
STRAIN AND LATTICE DISTORTION IN SEMICONDUCTOR STRUCTURES: A SYNCHROTRON RADIATION STUDY

DISSERTATION

zur Erlangung des akademischen Grades
Doktor der Naturwissenschaften (Dr. rer.nat.)
in der Wissenschaftsdisziplin Festkörperphysik

eingereicht an der
Mathematisch-Naturwissenschaftlichen Fakultät
der Universität Potsdam

von

DANIEL LÜBBERT

Potsdam, im Dezember 1999

Contents

Introduction	1
I X-ray diffraction: Theory & methods	5
1 X-ray diffraction in practice	5
1.1 Fundamentals	5
1.2 A source of X-rays: Third generation synchrotrons. The ESRF, Grenoble	6
1.3 Diffraction geometries. Terminology	8
1.4 Diffractometers	9
1.5 Angular versus reciprocal space. Transformation formulae	11
1.6 Resolution considerations	14
2 X-ray diffraction theory: a short primer	16
2.1 Basics	16
2.2 From the dynamical to the kinematical theory of X-ray diffraction	19
2.3 Peculiarities of grazing incidence diffraction	22
II Lattice distortions on a scale of some micrometers: Direct observation by X-ray rocking curve imaging	25
3 X-ray rocking curve imaging: Principle	25
3.1 Introduction and motivation	25
3.2 Methods to achieve spatial resolution with X-rays	26
3.3 A new method: μm -resolved X-ray diffraction by a combination of diffractometry and topography	27
3.4 Conclusion	33
4 Application to industrial quality inspection of semiconductor wafers	34
4.1 Experimental example: GaAs wafers	34
4.2 Another example: SiC wafers	35
4.3 Perspective: Determination of complete strain fields via μm -resolved <i>triple</i> crystal diffractometry	37
4.4 Conclusion	38
III Lattice distortions on a scale below the micrometer: Strain investigations in semiconductor surface nanostructures	39
Short historic introduction	39

5 Theory of diffraction from (strained) gratings	41
5.1 Grating geometry and reciprocal space structure	41
5.2 Strained gratings and elasticity theory	44
5.3 Numerical calculation of strain fields. The Finite Element Method	48
5.4 X-ray diffraction from strained crystals and from strained gratings	51
5.5 Conclusion – A general procedure for strain investigation	56
6 Monitoring the strain evolution in the fabrication process of gratings	59
6.1 Introduction. The samples	59
6.2 Simple surface grating: a reference case	60
6.3 Growth of a strained layer. Grating-induced strain relaxation	62
6.4 Overgrowth of an embedding layer. Counteraction on strain	64
6.5 Calculation of strain fields and reciprocal space maps	66
6.6 Conclusion	69
7 Strained layer gratings with variable shape	70
7.1 Introduction. The samples.	70
7.2 Trapezoidal grating	71
7.3 Rectangular grating	76
7.4 Conclusion	78
8 Superlattice gratings	80
8.1 Introduction. The sample	80
8.2 Symmetrical and asymmetrical diffraction	82
8.3 Theoretical calculation and fit of the results	83
8.4 Conclusion	87
9 Dynamic patterning by surface acoustic waves	88
9.1 Introduction	88
9.2 Experimental rocking curves	89
9.3 Adaptation of the simulation procedure. Fit of experimental results	90
9.4 Conclusion	93
Summary and perspectives	95
Appendix	i
A Transformation of elastic constants into different coordinate systems	i
Bibliography	v
Miscellaneous	xvii
List of publications	xvii
List of abbreviations	xix
List of important symbols	xx
Acknowledgements	xxi
Main conclusions (in German)	xxiii
Curriculum Vitae	xxv
Versicherung	xxvii

Introduction

This thesis presents X-ray methods for the analysis of lattice distortions on micrometer and sub-micrometer length scales in a variety of semiconductor structures. Before introducing these methods, let us briefly review the historic development of semiconductor fabrication techniques and their relevance for the field of modern microelectronic and optoelectronic devices.

The success story of semiconductor physics and device technology began in the 1950s with germanium and silicon, both from group IV of elements in the periodic table [Jac98]. Later, similar crystal growth techniques as for these two were developed also for other semiconductor materials, especially for combinations of elements from groups III and V (the so-called III-V compound semiconductors) like GaAs and InP [Nel63, WHW99]. These are particularly interesting for applications in optoelectronic devices such as semiconductor lasers, due to their direct band gap.

Another important step was the possibility to grow semiconductor crystals consisting of a mixture of two or more binary III-V materials. Ternary compounds like $\text{Ga}_x\text{In}_{1-x}\text{As}$ allow to vary the value of the band gap continuously between the extremes of the two binary materials involved, and thus to do “band-gap engineering” via the material composition x . The introduction of quaternary materials like $\text{Ga}_x\text{In}_{1-x}\text{As}_y\text{P}_{1-y}$ [Pea82] opened an additional degree of freedom, which is useful for instance in order to select independently both the band gap and the lattice parameter of the material.

In the 1960s and 1970s techniques for the growth of thin crystalline layers were invented and optimized. The variants include *liquid phase epitaxy* (LPE), *vapour phase epitaxy* (VPE) *chemical vapour deposition* (CVD) and *molecular beam epitaxy* (MBE). Nowadays, they allow to fabricate layers with thicknesses down to some 10 nm and even monolayers [Kel95]. This control of materials along one dimension has led to microelectronic and optoelectronic devices that exhibit novel properties. Examples are quantum well lasers [LHH90] and high electron mobility structures [PWS89].

In parallel, techniques for the *lateral* structurization of semiconductor structures in the sub-micrometer range were developed. They are mostly based on holographic or electron-beam lithography and etching, and allow to structurize semiconductors not only in the growth direction, but also in one or two directions along the surface. Different methods for obtaining laterally patterned thin layers are used in practice. The most widespread one is to first grow a thin planar layer which is subsequently etched [Kel95]. An alternative is to first etch a substrate material, and then to grow a thin layer on the pre-patterned surface [LTV90, Gal91]. A third way is to make use of the self-organized patterning which occurs in the growth of strain multilayers on misoriented substrate surfaces. Remarkably periodic lateral patterns have been observed in structures produced in this way [BGL99]. To simplify the terminology, all these types of lateral structures will be referred to as “gratings”.

Such lateral surface nanostructures are technologically very promising for use in optoelectronic devices, due to two special effects: *optical confinement* and *electrical confinement*. Optical confinement [Cor98] is used in distributed feedback lasers (DFB-lasers), where gratings are employed as resonators which selectively amplify special wavelengths, thus replacing the optical reflectors (Fabry-Perot cavity) used in more conventional lasers.

Electrical confinement [HC89] appears when charge carriers are enclosed in a region with an extension of less than approximately 50 nm along one, two or three dimensions - in so-called quantum wells, quantum wires and quantum dots, respectively. In this case, quantization effects occur which alter the electronic energy levels and the density of states [AS82]. This is technologically relevant in semiconductor lasers where the patterned region is simultaneously the active region of the device, i.e. the one in which

the recombination of charge carriers and the light emission take place. It allows to obtain improved laser characteristics by achieving a lower threshold current density [Yar88] as well as a higher differential gain [AMS86] and better temperature stability [AS82], and thus an increased overall device performance. Similar improvements can also be obtained by intentionally incorporating *strain* into the active region of the laser [Ada86, ALK86, HKS91, BBF98].

Simultaneously with the technological progress in fabrication methods grew the demand for techniques to characterize such nanoscopically structured samples. Especially in the initial stages of the development of a new growth or patterning technology, it is indispensable to inspect the resulting structures by an independent method. The final device performances are influenced by the crystalline properties of the material as well as by the geometry in the case of lateral patterning. Therefore the parameters of interest for a structural investigation include:

The sample geometry: the layer thicknesses in planar layered structures, a possible miscut of the sample surface with respect to the intended orientation, the grating periodicity, grating shape and grating orientation in the case of laterally patterned structures.

Properties of surfaces and interfaces: the roughness of the sample surface and interfaces, its statistical correlation properties, and the question whether the interfaces between layers with different compositions are atomically sharp or graduated.

The crystalline properties: the perfection of the crystalline lattice, the occurrence of defects, the lattice parameters of the different materials and their misfit, the resulting strain distribution, and the strain relaxation in gratings.

The crystalline properties are especially interesting since they are particularly difficult to control in the technological fabrication process, and since they play an important role for the device properties and device performance.

Several categories of methods are available to meet the demand for characterization techniques. Spectroscopic methods, like photoluminescence, allow to investigate the electronic band structure in nanostructures [ALK86, TMY92, Dar99]. Microscopic methods such as transmission electron microscopy (TEM), scanning electron microscopy (SEM), and atomic force microscopy (AFM) are attractive due to their impressive spatial resolution, and because they yield *visual* results which can often be readily interpreted and give a direct impression of the sample structure. They can be used in particular to investigate the roughness of a sample surface or the geometry of surface gratings, i.e. the first two of the three groups of parameters quoted above. Recently, high-resolution TEM has also been employed to study the strain distributions in epitaxial structures, with the examples of GaInAs quantum wires [CRS94] and of CdSe islands in a ZnSe matrix [SKP98].

Nevertheless, the issue of structural characterization is not closed with these techniques. Drawbacks of microscopic methods include that they are either purely surface-sensitive (SEM, AFM) or connected with the destruction of the sample (TEM), and require a special sample preparation. Another limitation is that they are *local* methods and cannot easily provide *representative* information about the variation of certain parameters (such as a grating period) along the whole sample surface. This is true in particular for the investigation of lattice parameters, which in the above-mentioned studies were determined with moderate precision and only in a restricted field of view.

What is required is therefore a method (1) which penetrates further into the sample and allows to overcome the restriction to the sample surface, (2) which — in view of strain investigations — is more sensitive to the crystalline properties and the lattice parameter, and (3) which provides more representative, statistically significant information.

X-rays are nearly ideal in all three respects: Their high penetrating power became apparent immediately after their discovery by Röntgen in 1895; Laue recognized in 1912 that their wavelength is of the order of the lattice spacing in crystals, and that they could thus be diffracted by crystals [FKL12]; and diffraction methods operate in reciprocal space, so that they “automatically” yield statistically averaged information. Since the advent of dedicated synchrotron sources in the 1970s and 1980s, very powerful sources of X-rays are available and allow to investigate even very thin layers with sufficient intensity.

Therefore in this thesis X-ray diffraction methods are used to investigate the crystalline properties, and in particular the lattice distortions and strain fields, of semiconductor structures. Two kinds of structures will serve as examples to demonstrate the potential of X-ray diffraction techniques for strain studies: wafers on the one hand, and surface gratings on the other hand. In a certain sense, these two systems represent the two extremes of a broad range of semiconductor structures.

Wafers are the “raw material”, the starting substance for many technological processes. They serve as substrates on which layered structures and complete integrated circuits are fabricated. Lattice distortions in wafers are particularly important since they can influence the properties of the entire structures which are grown on top of them, and thus lead to the degradation of device properties. These distortions arise due to the incomplete control of the bulk growth methods for certain crystalline materials: Silicon can nowadays be produced as an almost perfect single crystal, but the technologies for certain compound semiconductors are much less optimized [Jac98]. Efficient methods to monitor lattice distortions in semiconductor wafers can contribute to the further improvement of these growth technologies.

At the other end of the spectrum, surface gratings represent the whole category of low-dimensional systems like quantum wires and quantum dots. Since these are usually produced using sophisticated epitaxial methods, lattice defects do not play an as important role as in wafers. Instead, the focus will be on the *coherent* strain fields which arise due to the lattice mismatch between adjacent materials with different lattice parameters, and in the mechanism of strain relaxation as a result of the lateral patterning. Such strain fields in planar structures limit the maximum thickness (*critical thickness*[MB74]) up to which thin mismatched layers can be grown *pseudomorphically* (without formation of misfit dislocations). Strain and strain relaxation in gratings influences their electronic band structure, as discussed above. It is therefore important to understand the mechanisms of strain relaxation, especially in view of applications to strain engineering.

In both cases of wafers and gratings one needs to achieve a high *real-space* resolution in X-ray methods, while not losing the very high *reciprocal space* (or equivalently angular) resolution for which X-ray techniques are traditionally optimized. In the case of wafers it will become clear that detecting and analyzing the relevant variations of crystalline quality across the sample requires a resolution of the order of 1–10 μm . Part II of this work will show that such a resolution can be achieved “directly” with the help of the special X-ray beam properties and equipment of a synchrotron beamline. In the case of gratings, the relevant changes in the strain field occur on a length scale significantly below the micrometer. A spatial resolution of this order can presently not be achieved with “direct” experimental methods. Part III will show how it can nevertheless be realized due to interference effects and an appropriate data analysis procedure.

Structure of this thesis

The first Chapter of this manuscript gives a brief general introduction into the experimental methods and the instruments used in X-ray diffraction. Since all the experimental results contained in this manuscript were obtained with synchrotron X-rays, the most important characteristics of third generation synchrotrons sources will be presented briefly. A synopsis of the different diffractometer types used for this work is given, the relations between angular and reciprocal space for the different diffractometer geometries are discussed, and the question of instrumental resolution is briefly touched upon. Chapter 2 contains a digest of general X-ray diffraction theory. The main scope is to document those formulae which are essential ingredients of the analysis procedures for our experimental results. In Chapter 3 begins the description of the experimental studies. This Chapter presents a method which was developed and an equipment which was installed at the ID19 beamline of the ESRF that allow to perform *micrometer-resolved* quality investigations of crystalline structures. This method combines the advantages of X-ray diffractometry and X-ray diffraction topography, and is referred to as *X-ray diffraction rocking curve imaging*. Chapter 4 shows how this method can be applied to monitor lattice distortions in wafers of different semiconductor materials (with the examples of GaAs and SiC).

The next Part does the step towards the measurement of lattice distortions on a *sub-micrometer* length scale, namely strain relaxation in surface nanostructures. Chapter 5 lays the theoretical foundations for the analysis of strain fields in surface gratings. Since a knowledge of the grating *shape* is a necessary precondition for any strain analysis, the influence of the shape on the diffraction pattern will be reviewed first. Section 5.2 then describes how continuum elasticity theory can be adapted to describe strain fields in

nanoscopic gratings, and gives explicit results for special cases. Section 5.3 introduces the *Finite Element Method* and discusses how it can be employed to solve numerically the differential equations of elasticity in gratings samples in the general case. In Section 5.4 these results are coupled with X-ray diffraction theory. A general formula is obtained which allows to calculate numerically the diffraction patterns from a very general class of distorted crystalline structures. Section 5.5 establishes the link between numerical techniques and experimental strategies, and presents a general recipe for the quantitative investigation of strain fields in gratings.

This recipe is then explicitly applied to four different sample types. Chapter 6 starts with the study of the generation and evolution of inhomogeneous strain fields in the different technological steps involved in the fabrication of gratings. In particular, it will be demonstrated how X-ray diffraction uniquely allows to analyze *buried* gratings in a non-destructive way. Chapter 7 illuminates another aspect, namely the dependence of strain relaxation and the corresponding X-ray diffraction patterns on the grating *shape*. Furthermore, in this Chapter the analysis method is turned into an even more quantitative one by introducing a *fit loop*, involving simultaneous elastic calculations and simulations of diffraction patterns in order to achieve best agreement with the experimental data. Chapter 8 extends this method to the case of *superlattice* gratings. It demonstrates the new effects which occur when the sample structure is periodic not only along the lateral, but also along the vertical direction.

The samples studied in Chapters 6–8 are to be considered as test cases. Although their parameters do not correspond exactly to those of the quantum wire structures used for real devices, they reproduce those features of quantum wires which are most characteristic in the context of strain investigations. In fact, “real” quantum wires have already been successfully characterized by the same method [LJB99].

At the end of the thesis, Chapter 9 broadens the perspective, away from artificially etched samples towards other kinds of laterally periodic structures. It shows how the same data evaluation technique can be applied to analyze the periodic distortion fields occurring in crystal surfaces under the influence of surface acoustic waves. This Chapter serves as an example to demonstrate the flexibility and general applicability of the approach presented in the previous chapters.

To conclude the introduction, let us also give an overview from a crystallographic point of view: The semiconductor samples studied in this work are almost exclusively III-V-compounds, with the exception of one IV-IV material (SiC). All the samples have a [001]-oriented surface. For the non-crystallographer, let us mention that these materials have a Zinc-Blende structure, i.e. an fcc-lattice with a two-atom base. In the context of X-ray diffraction, this means that all the Bragg peaks with mixed even and odd indices HKL are forbidden, and that those with $(H + K + L) = 4n + 2$ (with n integer), such as 002 and 222, are in general particularly weak. We will therefore use mostly reflections like 004, 224 and 220.

Concerning notation, we will use the *Einstein summation convention* throughout this work: Whenever the same index appears twice on the same side of an equation, a summation over the applicable range of this index is tacitly implied. As an example, Hooke’s law (5.24) is written $\sigma_{ij} = C_{ijkl} \epsilon_{kl}$, which is to be read as $\sigma_{ij} = \sum_{k=1}^3 \sum_{l=1}^3 C_{ijkl} \epsilon_{kl}$.

Part I

X-ray diffraction: Theory & methods

Chapter 1

X-ray diffraction in practice

In this chapter we give a very brief general introduction to the basics of X-ray scattering, as well as to the techniques and instruments used in X-ray scattering experiments. The aim is to put the reader, who may not be an expert of X-ray diffraction, in a position to understand the experimental procedures and results which are to be presented in subsequent parts of this work.

1.1 Fundamentals

X-rays are electromagnetic waves, similarly to visible light, but with far higher frequencies ω and photon energies $\hbar\omega$, or correspondingly with far shorter wavelengths λ . The electric field of a monochromatic plane wave can be written as

$$\mathbf{E}(\mathbf{r}, t) = \mathbf{E}_0 e^{i(\mathbf{K} \cdot \mathbf{r} - \omega t)}. \quad (1.1)$$

The length of the wave vector \mathbf{K} in vacuum is given by $|\mathbf{K}| = \omega/c = 2\pi/\lambda$, where c is the velocity of light. Inside a material this length changes to $|\mathbf{k}| = n|\mathbf{K}|$, where the refraction index n is generally slightly less than 1 at X-ray frequencies.

X-rays interact with matter in a variety of ways. The most important in our context is elastic scattering, in which the single photons are deviated from their incident direction, but do not lose energy. It can be quantitatively explained by the fact that the incident electric field leads to a forced oscillation of the electron, which then acts as an accelerated charge and re-emits radiation of the same wavelength [War90]. The atomic nuclei cannot follow the fast oscillation of the electric field due to their much higher mass, and therefore do not contribute essentially to the elastic scattering cross section.

Two decades after the discovery of X-rays by Röntgen in 1895 it was recognized by Max von Laue that the wavelength λ of X-rays is of the same order of magnitude as the interatomic distances in crystals [FKL12]. Therefore, the X-rays scattered by the electrons around different atoms in a crystal can interfere, giving rise to sharp peaks of *diffracted* intensity in precise directions. The angular positions of these *Bragg peaks* are described by the Bragg law:

$$2d_{HKL} \sin \vartheta_B = \lambda, \quad (1.2)$$

where d_{HKL} ($= \frac{a}{\sqrt{H^2+K^2+L^2}}$ for a cubic crystal) is the spacing of two neighbouring lattice planes with Laue indices H , K and L , and ϑ_B is the Bragg angle. This diffraction condition can be stated alternatively in the *reciprocal space* formulation. One defines a *reciprocal lattice* whose basis vectors \mathbf{Q}^1 , \mathbf{Q}^2 , \mathbf{Q}^3 depend on the basis vectors of the crystal lattice \mathbf{a}^1 , \mathbf{a}^2 , \mathbf{a}^3 via

$$\mathbf{Q}^1 = \frac{2\pi}{V} \mathbf{a}^2 \times \mathbf{a}^3 \quad \mathbf{Q}^2 = \frac{2\pi}{V} \mathbf{a}^3 \times \mathbf{a}^1 \quad \mathbf{Q}^3 = \frac{2\pi}{V} \mathbf{a}^1 \times \mathbf{a}^2. \quad (1.3)$$

$V = \mathbf{a}^1 \cdot [\mathbf{a}^2 \times \mathbf{a}^3]$ represents the volume of the unit cell of the crystal lattice. In this way, the *Laue conditions* $\mathbf{Q}^m \cdot \mathbf{a}^n = 2\pi\delta_{mn}$ (with δ_{mn} being the Kronecker-Delta) are satisfied. Then, the Bragg law

(1.2) is equivalent to the condition that the *scattering vector* \mathbf{Q} , i.e. the difference between the incident and exit wave vectors \mathbf{K}_i and \mathbf{K}_f , must be equal to a vector $\mathbf{h} = H \cdot \mathbf{Q}^1 + K \cdot \mathbf{Q}^2 + L \cdot \mathbf{Q}^3$ of the crystal's reciprocal lattice:

$$\mathbf{Q} = \mathbf{K}_f - \mathbf{K}_i = \mathbf{h} \quad (1.4)$$

This thesis deals with the structural characterization of crystals by elastic scattering of X-rays in the vicinity of Bragg peaks. Our main method for this investigation is X-ray *diffractometry*, i.e. the measurement of scattered intensity I as a function of the relative positions of the incident beam, the sample and the detector.

Traditionally, the results of such measurements are often represented as a function of diffractometer angles: $I(\omega, 2\theta, \dots)$. A great deal of commercial control and simulation software is based on this angular scale. However, for our purposes it is more convenient to use a reciprocal space representation, since this makes it easier to concentrate on the structural features of the sample, independently of the effects of different measurement geometries. Therefore, throughout this work we will represent our results as diffracted intensity $I(\mathbf{Q})$ versus scattering vector \mathbf{Q} .

1.2 A source of X-rays: Third generation synchrotrons. The ESRF, Grenoble

In the first half of this century the only X-ray source at hand were laboratory X-ray tubes, which, apart from *Bremsstrahlung*, emit mainly at the characteristic emission lines of the respective anode material (such as Cu at $\lambda = 1.540597\text{\AA}$). An alternative with many very interesting characteristics has become available since the invention of synchrotrons in the 1940s [McM45, Vek45], and in particular since the construction of *second generation synchrotrons* in the 1970s. While the former were mainly used for particle physics, the latter were optimized for the emission of synchrotron radiation.



Figure 1.1: Top view of the ESRF, including a sketch of its accelerator structures. On the left, one can see one of the two beamlines at the ESRF which are not located in the experimental hall, but outside: The one shown here is in fact the beamline ID19, on which parts of the results presented in this thesis were obtained. (ESRF information office)

X-ray beams generated in this way have extraordinary properties which make them very attractive for a multitude of experiments: They are very intense, highly collimated in forward direction, strongly polarized, cover a broad spectrum of wavelengths, and have a pulsed time structure. The most interesting features in our present context are the very high intensity as compared to classical X-ray tubes, and the tunable continuous spectrum. For these two reasons most of the work presented in this manuscript was performed at the European Synchrotron Radiation Facility (ESRF, Grenoble - see Fig. 1.1) and other synchrotrons.

Figure 1.2: Sketch of the storage ring, showing the principal geometry of bending magnets, insertion devices and beamlines. (ESRF information office)

The ESRF, opened to users in 1994, consists mainly of a storage ring with 800 m circumference, in which an electron beam with a nominal energy of 6 GeV and a maximum current of $I = 200$ mA circulates for 6-12 hours. It is a *third generation synchrotron*, which means that X-rays are generated not only in the bending magnets which keep the electron beam on its circular path, but also in so-called *insertion devices* (see Fig. 1.2).

Bending magnets, wigglers and undulators

Insertion devices consist of a periodic sequence of dipole magnets with alternating orientation, and force the electron beam on a slalom trajectory (see Fig. 1.3). X-rays are emitted in each of the periods, and the total resulting X-ray intensity (and *brightness* [Wil96]) is considerably higher than in a bending magnet. Insertion devices are classified into two categories: *wigglers* and *undulators*. The relevant parameter for this distinction is the dimensionless quantity K [Wil96]:

$$K = \frac{\lambda_u e \tilde{B}}{2\pi m_e c}, \quad (1.5)$$

where λ_u is the magnetic period and \tilde{B} is the maximum magnetic field on the beam axis. This parameter K determines the maximum angular deviation Θ_w of the electron trajectory from a straight line via

$$\Theta_w = \frac{1}{\gamma} K, \quad (1.6)$$

where the relativistic parameter $\gamma = 1/\sqrt{1 - v^2/c^2}$ depends on the electron beam energy only.

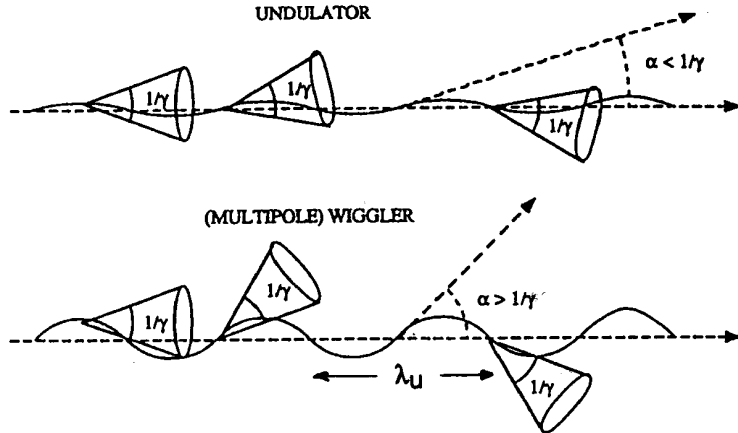


Figure 1.3: Distinction between wigglers and undulators. [Rao93]

When $K \leq 1$ the insertion device is called an *undulator*. In this case, the electrons are only weakly deviated from a straight line, so that the X-rays emitted in the single periods of the electrons' trajectory can interfere coherently. This leads to a spectrum with strong peaks at one special X-ray energy and its higher harmonics. The fundamental wavelength λ_1 depends on the electron beam energy and the magnet parameters via [Wil96, Rao93]

$$\lambda_1 = \frac{\lambda_u}{2\gamma} \left(1 + \frac{K^2}{2} + \gamma^2 \Theta_{\text{obs}}^2 \right), \quad (1.7)$$

and is smallest on the beam axis (angle of observation $\Theta_{\text{obs}} = 0$).

In the opposite case of $K > 1$ the insertion device is called a *wiggler*. Here, the deviation of the electrons is much stronger, and no more interference can occur. The X-ray spectrum is a more continuous distribution which, apart from being stronger in intensity, is comparable to the spectrum of a bending magnet.

Experimental stations. The example of the beamline ID19 at the ESRF

The X-rays generated in this way then travel along a *beamline* where they are monochromatized or conditioned in other ways in an *optics hutch* before they arrive in the *experimental hutch* and at the experiment. The beamline ID19 at the ESRF, where parts of the results presented in this thesis have been obtained, was described and characterized in great detail in a previous study [Zon95]. Therefore, we will omit the technical details and focus on some characteristic features.

ID19 is one of the two beamlines at the ESRF which are located not inside the experimental hall, but in a separate building. The distance from the wiggler source to the experimental hutch amounts to 145 m. This provides ideal conditions for applications such as X-ray diffraction topography, tomography, radiography, and X-ray imaging in general. The large distance allows to obtain a spatially extended and yet homogeneous beam with a low angular divergence and good coherence properties. The spot size on the sample can be as large as 4×1.5 cm.

Since the construction of a second, vertical diffractometer at the beginning of this thesis [MMH97, Mil99], high-resolution X-ray diffractometry can also be performed at ID19 [LJB99]. A system of accurate slits permits to restrict the size of the incident beam [ZBG99]. This beamline is equipped with a *FReLoN* camera, a fast CCD-camera which allows to record two-dimensional images of diffracted X-ray intensity [LSPvB96]. This camera will be of particular interest in the context of this thesis. We will make use of the special characteristics of ID19 and its equipment in the Chapters 3 and 4 of this thesis.

1.3 Diffraction geometries. Terminology

X-ray diffraction can be performed with different instrumental setups, and in a variety of experimental geometries. In this section, we introduce some distinctions in order to clearly define the terminology used in the experimental part of this work.

Coplanar versus non-coplanar diffraction

An X-ray diffraction geometry is referred to as *coplanar* when the incident wave vector \mathbf{K}_i , the exit wave vector \mathbf{K}_f and the sample surface normal \mathbf{n} lie in the same plane. In this case, the scattering vector \mathbf{Q} can vary only in one plane in reciprocal space. In the context of this thesis, we define the Q_z axis to be directed along the outward surface normal of the sample. The plane of coplanar scattering is then called the Q_x - Q_z -plane. Two diffractometer angles are sufficient to perform a coplanar diffraction experiment. Most commercially available instruments are based on (and restricted to) this coplanar geometry.

The opposite case of a *non-coplanar* diffraction geometry provides access to the whole, three-dimensional reciprocal space of the sample. To realize it with a diffractometer, further angular degrees of freedom (usually at least four) are required. Many diffractometers on synchrotron beamlines allow to do measurements in non-coplanar geometry. The greater flexibility which this offers is a prerequisite in particular for grazing incidence diffraction experiments.

Symmetrical, asymmetrical and grazing incidence diffraction

A coplanar diffraction geometry (in the Bragg case) is said to be *symmetrical* when the X-rays are reflected from lattice planes which are parallel to the sample surface, and *asymmetrical* otherwise. For a cubic crystal with a 001-cut surface, measurements at the $00L$ -reflections correspond to a symmetrical diffraction geometry, while measurements e.g. at the 224- or the 113-reflections represent asymmetrical diffraction.

Grazing incidence diffraction (GID) measures the intensity distribution around Bragg peaks HKL with $L = 0$. In this case, the X-rays are reflected from lattice planes which are perpendicular to the sample surface. The momentum transfer \mathbf{Q} is essentially parallel to the sample surface. By tuning the value of the small angle of incidence α_i one can additionally control the penetration depth of the probing X-ray beam below the sample surface (see Section 2.3).

All three diffraction geometries are shown schematically in Fig. 1.4. This distinction between symmetrical, asymmetrical and grazing incidence geometry is particularly relevant in the context of strain

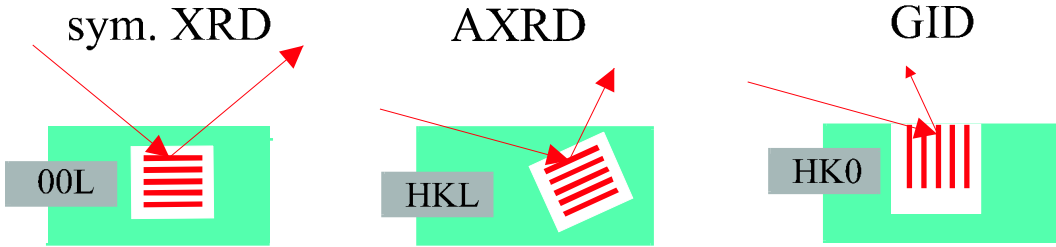


Figure 1.4: Different commonly used geometries for X-ray diffraction, shown for the case of a 001-cut crystal surface. In symmetrical diffraction (left) the X-ray beam is diffracted from lattice planes parallel to the surface (here, the 00L-planes). The momentum transfer \mathbf{Q} is perpendicular to the surface. In asymmetrical diffraction (center) it is inclined by a certain angle towards the surface normal. In grazing incidence diffraction (right) the X-ray beam is diffracted by lattice planes which are perpendicular to the surface. The momentum transfer \mathbf{Q} has a predominant lateral component (in the plane of the surface), and only a small vertical Q_z -component.

investigations, since they are selectively sensitive to different components of the strain field in the sample. This topic will be further discussed in Section 5.5.

Double axis and triple axis diffractometry

A diffraction experiment requires at least one crystal, the sample. In cases which necessitate a good instrumental resolution, further crystals are introduced into the beam path. On the incident beam side, a monochromator can be used to select one single wavelength and/or improve the angular resolution. On the exit side, an analyzer crystal can similarly be used to reduce the angular acceptance of the detector. The configuration with a monochromator and a sample is conventionally referred to as a *double-crystal diffractometer*; when an additional analyzer is used, we speak of a *triple-crystal diffractometry*. Note that this definition is independent of the actual number of crystals: An instrument may contain more than two crystals and still be a double-crystal diffractometer, in case the monochromator consists of a combination of two or four separate crystals, for instance.

1.4 Diffractometers

In this Section we give a short survey of some diffractometer types which are in common use for non-coplanar measurements, and which were in fact used in the course of this thesis on different synchrotron beamlines. The discussion in this Section is inspired by [Gün96].

Well-known instrumental setups for non-coplanar diffraction include the four-circle diffractometer [BL67, Moc88], the ‘z-axis’ diffractometer [Blo85], the six-circle [LV93] and the modified six-circle (‘2+2’)-diffractometer [Vli98], and a variant of the six-circle diffractometer, the so-called w21v diffractometer [ELT95, RVG95]. We will briefly compare these instruments in view of their principal geometrical features and of their respective advantages for our purposes.

The geometry of the four-circle diffractometer is shown in Fig. 1.5. It offers a total of four angular degrees of freedom, three of which (χ , ϕ and ω) correspond to the Euler angles of the sample and are used to put it into diffraction position. The fourth angle (called δ in the image) is used for the detector and determines uniquely the total scattering angle 2θ . Therefore, the scattering plane is fixed to either the horizontal or the vertical plane.

The six-circle diffractometer (left image of Fig. 1.6) offers two more angular degrees of freedom, and thereby allows a greater flexibility. Three angles (χ , ϕ and ω) are used to align and scan the sample. The detector can rotate around two perpendicular axes, called δ and γ . The sixth angle, named α , allows to rotate the whole apparatus with respect to the incident beam, and thereby to change the angle of incidence on the sample surface, α_i . Under a movement of α , the detector position remains constant with respect to the sample surface, but changes with respect to the incident beam. For this reason, and because the

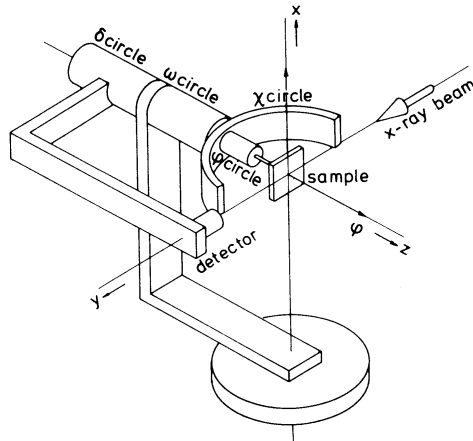


Figure 1.5: Geometry of the four-circle diffractometer. [VVdVM87]

scattering plane is not purely horizontal any more, the total scattering angle 2ϑ is a relatively complicated function of the diffractometer angles (for the calculation, see Section 1.5):

$$\cos 2\vartheta = \cos \delta \cos \gamma \cos \alpha - \sin \gamma \sin \alpha \quad (1.8)$$

This formula reduces to $2\vartheta = \delta$ when both γ and α are zero (purely vertical scattering plane). A diffractometer of this type was used for the experiments performed on the BW2-beamline of HASYLAB, Hamburg in the course of this thesis.

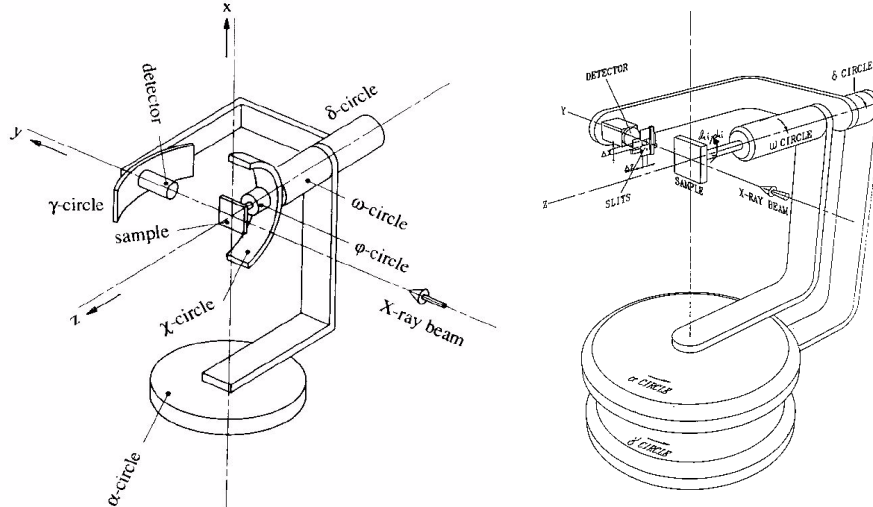


Figure 1.6: Geometries of the six-circle and the modified six-circle ('2+2') diffractometer. [Vli98]

A variant of the six-circle diffractometer is the '2+2'-diffractometer (or *modified six-circle diffractometer*) shown in the right image of Fig. 1.6. Here, sample and detector can be rotated individually around a vertical axis by two independent angles, called α and γ . In this way, the movements of sample and detector are decoupled, and controlled by one pair of angles each (γ and δ for the detector, and α and ω for the sample, plus the two angles ϕ and χ for the sample alignment). For this reason, the expression for the total

scattering angle reduces to:

$$\cos 2\theta = \cos \gamma \cdot \cos \delta \quad (1.9)$$

The angle of incidence is still uniquely determined by the motor α , but the angle α_f between exit beam and sample surface now depends on both detector motors [RVG95]:

$$\sin \alpha_f = \cos \delta \sin(\gamma - \alpha) \quad (1.10)$$

In fact, the roles of the detector angles γ and δ are interchanged with respect to the previous case. Now, γ is the independent angle which moves around an axis which is fixed in space, whereas the position of the δ -axis is variable and depends on the value of γ .

A third of diffractometer for non-coplanar scattering is shown in the left image of Fig. 1.7: the w21v-diffractometer. Here, the geometry of the four sample and detector rotations is identical to the ‘2+2’-diffractometer; only the two alignment angles for the sample are different. Instead of one horizontal rotation axis ϕ and one Eulerian cradle χ (see Fig. 1.6), the instrument has a set of two mutually perpendicular Eulerian cradles χ_1 and χ_2 . A diffractometer of this type was used for experiments in the context of this thesis on the ID32-beamline of the ESRF. There exists a horizontal version of this geometry: the w21h

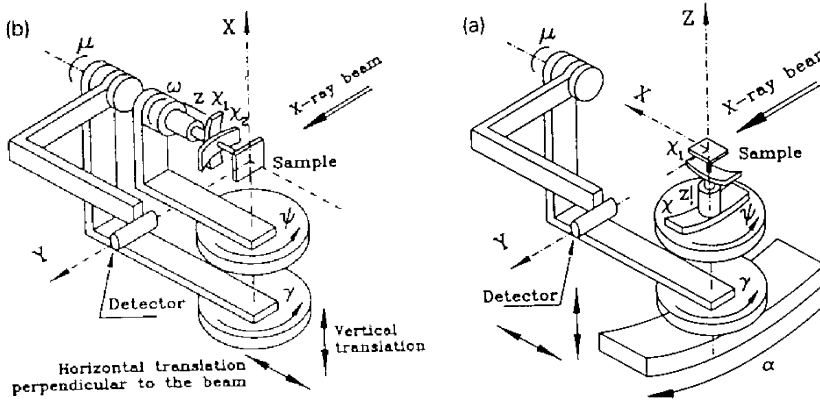


Figure 1.7: Geometries of the w21v and the w21h-diffractometer. [RVG95]

diffractometer (see right image of Fig. 1.7). Here, the sample is in horizontal position, which is favourable for scattering from liquid surfaces. A further advantage is the simpler resolution function: In the w21h-geometry, a set of horizontal and vertical detector slits always remain parallel and perpendicular to the sample surface, respectively, independently of the actual diffractometer angles γ and μ . This is not the case for the w21v-geometry, but can also be achieved in yet another type of instrument, the ‘2+3’-diffractometer [Vli98].

For measurements at synchrotrons, the beam polarization must be taken into account when choosing a diffractometer geometry: The beams from bending magnets and from the usual type of insertion devices are polarized in the horizontal plane, so that in order to obtain a maximum of diffracted intensity it is advantageous to choose a vertical scattering plane (s-polarization). This means that for coplanar diffraction the sample should be fixed on the diffractometer in horizontal position, whereas for grazing incidence diffraction it should be in vertical position.

1.5 Angular versus reciprocal space. Transformation formulae

As mentioned in Section 1.1, we usually do not control the experiment in terms of diffractometer angles, but of scattering vectors in reciprocal space. To facilitate the conversion between the two systems of reference, we first quote the transformation formulae for the case of coplanar scattering and then show a recipe to do the calculation in the general, non-coplanar case.

1.5.1 Coplanar diffraction

In the case of a coplanar diffraction geometry two angular degrees of freedom are sufficient to vary \mathbf{Q} within the accessible $Q_x - Q_z$ -plane. The relevant angles as well as the directions of the real- and reciprocal-space axes are defined in Fig. 1.8.

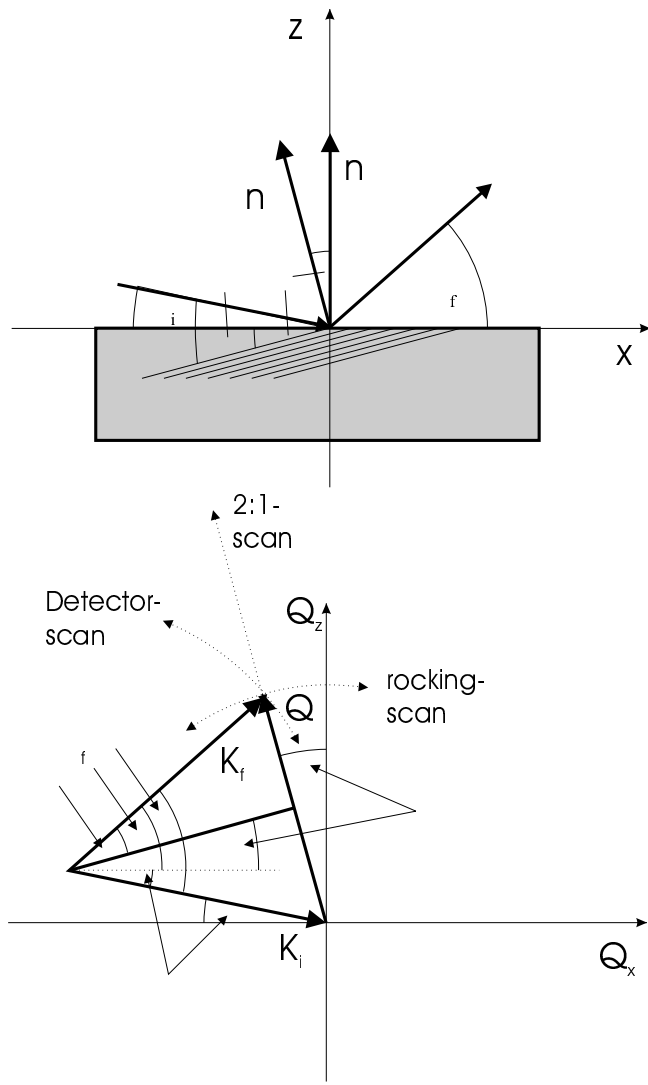


Figure 1.8: Sketch of the coplanar scattering geometry in real space (above) and reciprocal space (below) \mathbf{n} is the sample surface normal, \mathbf{n}_ϕ the normal to the diffracting lattice planes. ϕ is the angle between the two normals, and ω is the angle between the incident beam and the diffracting lattice planes, corresponding to $\omega = \alpha_i + \phi$. The right figure also shows the trajectories in reciprocal space of some simple angular scans (for a more detailed discussion, see e.g. [Tol93, Mik97]).

The relationships between the diffractometer angles and the components of \mathbf{Q} can be written in terms of the angle of incidence (α_i) and of exit (α_f) with respect to the sample surface,

$$Q_x = \frac{2\pi}{\lambda} (\cos \alpha_f - \cos \alpha_i) \quad (1.11)$$

$$Q_z = \frac{2\pi}{\lambda} (\sin \alpha_f + \sin \alpha_i), \quad (1.12)$$

or alternatively ¹ in terms of the total scattering angle 2ϑ and of ϕ , which is connected to the angle ω between the incident beam and the diffracting lattice planes by $\omega = \phi + \alpha_i$ (see Fig. 1.8),

$$-Q_x = |\mathbf{Q}| \sin \phi = \frac{2\pi}{\lambda} \cdot 2 \sin\left(\frac{2\vartheta}{2}\right) \cdot \sin \phi \quad (1.13)$$

$$Q_z = |\mathbf{Q}| \cos \phi = \frac{2\pi}{\lambda} \cdot 2 \sin\left(\frac{2\vartheta}{2}\right) \cdot \cos \phi \quad (1.14)$$

For both formulations, it is a relatively easy task to perform the inverse operation, i.e. to calculate the diffractometer angles required in order to reach a given scattering vector \mathbf{Q} .

1.5.2 Non-coplanar diffraction

The case of non-coplanar scattering is more involved. In order to avoid an excessive amount of trigonometric functions, we adopt a more compact matrix notation. Let $\mathcal{R}_i(\phi)$ be the rotation matrix for an active rotation by an angle ϕ around the e_i -axis, so that e.g.

$$\mathcal{R}_z(\phi) = \begin{pmatrix} \cos \phi & -\sin \phi & 0 \\ \sin \phi & \cos \phi & 0 \\ 0 & 0 & 1 \end{pmatrix} \quad (1.15)$$

The first step is now to transform the incident and exit wave vectors from the laboratory system (\mathbf{K}_i^L and \mathbf{K}_f^L) to the sample system (\mathbf{K}_i^S and \mathbf{K}_f^S), and thereby to express them in the reciprocal space of the sample. Let us take the example of the w21v-diffractometer at the ID32 beamline of the ESRF (see Fig. 1.7). The incident wave vector is directed along the y -axis, $\mathbf{K}_i^L = K \cdot e_y$. To transform it to \mathbf{K}_i^S , it must first be rotated by the angle ψ around the x -axis, and then by the angle ω around the z -axis²:

$$\mathbf{K}_i^S = \mathcal{R}_z(-\omega) \cdot \mathcal{R}_x(-\psi) \cdot \mathbf{K}_i^L = \mathcal{R}_z(-\omega) \cdot \mathcal{R}_x(-\psi) \cdot e_y.$$

The position of the exit beam in the laboratory system depends on the angles μ and γ , and can similarly be written as

$$\mathbf{K}_f^L = \mathcal{R}_z(\mu) \cdot \mathcal{R}_x(\gamma) \cdot e_y.$$

The subsequent transformation of this exit wave vector to the sample system is similar, $\mathbf{K}_f^S = \mathcal{R}_z(-\omega) \cdot \mathcal{R}_x(-\psi) \cdot \mathbf{K}_f^L$. The total scattering vector in the sample system, $\mathbf{Q}^S = \mathbf{K}_f^S - \mathbf{K}_i^S$, can then be calculated via (**1** being the unit matrix)

$$\mathbf{Q}^S = \mathcal{R}_z(-\omega) \mathcal{R}_x(-\psi) \cdot [\mathcal{R}_z(\mu) \mathcal{R}_x(\gamma) - \mathbf{1}] \cdot e_y$$

This calculation can be implemented in a computer program, and adapted with little effort to the other geometries discussed in Section 1.4. Such a program has been developed in the initial stages of this thesis, and similar programs are available at most synchrotron beamlines.

¹The angles ω and ϕ introduced here could be called ω_{cop}^S and ϕ_{cop}^S to stress the fact that they are measured in the *coplanar* reciprocal space of the *sample*. They are not to be mixed up with the motor angles ω and ϕ appearing in some of the diffractometers of the previous section, which are used in the *non-coplanar* case and measured in the *laboratory* system of reference.

²We assume here that the sample has already been aligned with the help of the motors χ_1 and χ_2 . In a more general calculation this can be taken into account via the *orientation matrix* \mathcal{U} .

The inverse problem (calculating the diffractometer angles required to reach a certain scattering vector \mathbf{Q}) can also be solved. The most convenient method takes a detour and first calculates the incidence and exit angles α_i and α_f as well as θ_i/θ_f , the angles between the projection of $\mathbf{K}_i/\mathbf{K}_f$ into the sample surface plane and the diffracting lattice plane. These are related to the scattering vector by

$$\mathbf{Q} = \begin{pmatrix} \cos \alpha_f \cos \theta_f + \cos \alpha_i \cos \theta_i \\ \cos \alpha_f \sin \theta_f - \cos \alpha_i \sin \theta_i \\ \sin \alpha_f + \sin \alpha_i \end{pmatrix} \quad (1.16)$$

Although many modern diffractometer control programs [BES99, Cer99] allow to “drive” directly in reciprocal space, it is very useful to know the explicit transformation formulae of this Section. They do not only show which trajectories in reciprocal space can be realized by single motor scans, but also play a role in the understanding of the resolution function of an instrument.

1.6 Resolution considerations

The measurable intensity distribution in reciprocal space is commonly written as a convolution of the reciprocal space structure of the sample, $I^0(\mathbf{Q})$, with the resolution function $R(\mathbf{Q})$ of the instrument:

$$I^{\text{exp}}(\mathbf{Q}) = \int I^0(\mathbf{Q}') \cdot R(\mathbf{Q} - \mathbf{Q}') \quad d\mathbf{Q}' \quad (1.17)$$

More precisely, the resolution function (at least the one in reciprocal space, as opposed to the one in angular space) does not depend on the difference $\Delta\mathbf{Q} = \mathbf{Q} - \mathbf{Q}'$ only, but on both \mathbf{Q} and \mathbf{Q}' separately: The measured intensity distribution around the 004-peak of, say, a perfect InP-crystal differs from the distribution around the 224-peak, due to the different experimental geometry. However, in a limited region around single Bragg peaks it is safe to approximate R locally as a function of $\Delta\mathbf{Q}$ only. To be exact, the local $R(\Delta\mathbf{Q})$ should then not be called *the* resolution function, but rather the resolution function *at a certain reflection*. With this in mind, we will now conform to common usage and refer to (the local) $R(\Delta\mathbf{Q})$ as “the resolution function”.

The resolution functions of triple-crystal diffractometers have been studied in detail in a series of articles [DuM37, Cow87, LGC89, GC90, BBP92] (see also [Tol93], and [HM96] for a comprehensive theoretical review). We will summarize here the most important qualitative features.

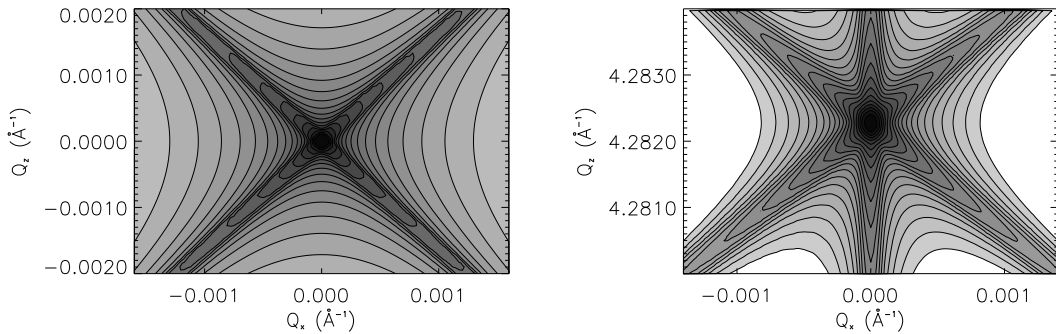


Figure 1.9: Illustration of the resolution function of a triple crystal diffractometer with a Si-111-monochromator and -analyzer for the InP-004-reflection and a wavelength $\lambda = 1.54 \text{ \AA}$, calculated with the program xtrace [Mik98]. Left: Pure contribution from the monochromator and analyzer crystals (the so-called monochromator and analyzer streaks), given in relative coordinates. Right: Convolution of the resolution function on the left with the crystal truncation rod at the 004-reflection of a (perfect) InP sample crystal. The contour lines are equidistributed on a logarithmic scale, with an intensity ratio of $10^{0.25}$ between adjacent lines.

Figure 1.9 shows the theoretical resolution function of a triple-crystal diffractometer equipped with a Si-111-monochromator and a similar analyzer crystal, for the InP-004-reflection and a wavelength of $\lambda = 1.54 \text{ \AA}$. The maximum at the center is surrounded by two lines along which the intensity decays only slowly. These are the so-called *monochromator streak* and *analyzer streak*. They are caused by the fact that neither the monochromator nor the analyzer crystal diffract only into one precise direction. Rather, their reflection profile can be described by a Darwin-curve (see also p. 32). Therefore, the analyzer streak follows a line (or, over larger distances, a circle) perpendicular to the direction of the exit wave vector \mathbf{K}_f , and similarly for the monochromator streak.

In the case of a double-crystal diffractometer the situation is slightly different: There is no analyzer crystal, and therefore no analyzer streak appears. Instead, the angular acceptance of the detector is usually limited by slits. This results in broadening of the intensity along the same direction, with the difference that the intensity does not decay continuously, but remains constant within a certain range and then suddenly drops. The width of this broadening is determined by the angular slit aperture. For 1 mm slits at a distance of 1 m from the sample, we obtain an aperture of 1 mrad, which would correspond to nearly the whole extension of the diagonal lines in the right image of Fig. 1.9.

The situation can be improved by double-crystal (or channel-cut) monochromators and analyzers, or even a four-crystal DuMond-Hart-Bartels monochromator setup, which reduce the extension of the streaks [BT98, Section 2.5]. However, it remains true that the instrumental resolution function needs to be taken into account when comparing experimental and calculated data. This can principally be done in two ways: The first is to correct the experimental values by performing a *deconvolution* with the resolution function — an approach which is well-known from image treatment [Jan97]. In principle, this allows to reconstruct the “real” structure and to eliminate the contribution from the instrumental setup. However, the method presupposes a good *a priori* knowledge of the instrumental resolution function, and is furthermore relatively sensitive to numerical artefacts caused by the deconvolution algorithm. Therefore, in the rest of this work we will adopt the opposite strategy, which consists in convoluting the results of a simulation with an approximate instrumental resolution function according to (1.17). Agreement with the experimental data is then achieved by adjusting the parameters of the resolution function of a reference sample.

Chapter 2

X-ray diffraction theory: a short primer

This chapter reviews some aspects of the theory of X-ray diffraction, in order to provide a general background for the calculation of scattered intensities. The whole theory has been documented in great detail in a series of excellent textbooks [vL60, Aza68, AKK74, Pin78, War90, Gui94, Zac94, BT98, HPB98]. Therefore, only those formulae will be mentioned here which are essential for the practical simulations performed to evaluate our experimental data in later chapters of this thesis.

2.1 Basics

X-rays interact mainly with the electrons in a material, since the atomic nuclei are too heavy to follow their high-frequency oscillation. Therefore, the interaction of X-rays with a material can be described in terms of the material's electron density $\rho(\mathbf{r})$. For a periodic arrangement of atoms in a crystal, the electron density can be expressed via a Fourier sum:

$$\rho(\mathbf{r}) = \frac{1}{V} \sum_{\mathbf{h}} F_{\mathbf{h}} e^{i\mathbf{h}\cdot\mathbf{r}}, \quad (2.1)$$

where V is the volume of the unit cell of the crystal, and the sum must be taken over all reciprocal lattice vectors \mathbf{h} . $F_{\mathbf{h}}$ is the *structure factor* of reflection \mathbf{h} .

Equivalent ways to describe the X-ray response of a material are the electric susceptibility $\chi(\mathbf{r})$, the dielectric function $\varepsilon(\mathbf{r})$, and the refractive index $n(\mathbf{r})$. The refractive index can be approximated by

$$n(\mathbf{r}) = \sqrt{\varepsilon(\mathbf{r})} = \sqrt{1 + \chi(\mathbf{r})} \approx 1 + \frac{\chi(\mathbf{r})}{2}, \quad (2.2)$$

since at X-ray frequencies the dielectric function differs from 1 by a very small amount only:

$$\varepsilon(\mathbf{r}) = 1 - \frac{e^2 \lambda^2}{4\pi^2 \epsilon_0 m_e c^2} \cdot \rho(\mathbf{r}) = 1 - \frac{r_e}{\pi} \lambda^2 \cdot \rho(\mathbf{r}). \quad (2.3)$$

The classical electron radius r_e has a value of 2.818×10^{-15} m.

With the definition $\Gamma = \frac{r_e \lambda^2}{\pi V}$ we can express $\varepsilon(\mathbf{r})$ as a function of the structure factors via

$$\varepsilon(\mathbf{r}) = 1 - \Gamma \cdot \sum_{\mathbf{h}} F_{\mathbf{h}} e^{i\mathbf{h}\cdot\mathbf{r}} \quad (2.4)$$

The structure factor $F_{\mathbf{h}}$, which is given by the inverse Fourier integral over one unit cell of the crystal, can be written as a coherent sum of the *atomic form factors* f_n over all atoms $n = 1 \dots N$ in the unit cell:

$$F_{\mathbf{h}} = \int_V \rho(\mathbf{r}) e^{-i\mathbf{h}\cdot\mathbf{r}} d^3\mathbf{r} = \sum_{j=1}^N f_j(\mathbf{h}) e^{-i\mathbf{h}\cdot\mathbf{r}_j}, \quad (2.5)$$

where \mathbf{r}_j is the relative position of the n -th atom within the unit cell. The atomic form factors represent the Fourier transform of the electron configuration around one single atom:

$$f_j(\mathbf{h}) = \int_{V_j} \rho_j(\mathbf{r}) e^{-i\mathbf{h}\cdot\mathbf{r}} d^3\mathbf{r} \quad (2.6)$$

In this form (which we will call f^0) the atomic form factor is real and depends on the *length* of the scattering vector $|\mathbf{Q}| = |\mathbf{h}| = 2\pi \cdot 2 \sin \vartheta / \lambda$ only, at least for atoms with a spherically symmetric electron configuration [Gui94]. This formulation is therefore valid for very high X-ray frequencies only, beyond the highest absorption edge of the respective atom. Resonance effects can be accounted for by adding a real correction f' which depends on the X-ray wavelength; furthermore, absorption can be included via an imaginary correction $if''(E)$. The final formula for the total atomic scattering factor is

$$f_j(\mathbf{Q}, \lambda) = f_j^0(Q) + f'_j(\lambda) + if''_j(\lambda) \quad (2.7)$$

Due to thermal vibrations, a crystal lattice cannot be perfectly periodic. Their influence can be accounted for by multiplying f_j with a *Debye-Waller factor* (m_j being the atomic mass) [Zac94]:

$$\hat{f}_j = f_j \cdot e^{-M_j} \quad \text{with} \quad M_j \sim \frac{kT}{m_j} \left(\frac{\sin \vartheta}{\lambda} \right)^2 \quad (2.8)$$

For practical use, the values for $f'_j(E)$ and $f''_j(E)$ over a wide range of X-ray energies are available in tabulated form in [Wil95]. The functional form of the remaining factor $f^0(Q) = f^0(\sin \vartheta / \lambda)$ is in general relatively complicated. For our purposes, it is sufficient to approximate them by a well-known empirical model with nine coefficients (named $a_1 - a_4$, $b_1 - b_4$, and c), which are specific for each sort of atom and can also be found in the *International Tables for Crystallography* [Wil95, p. 487]:

$$f^0 = \sum_{i=1}^4 a_i e^{-b_i \left(\frac{\sin \vartheta}{\lambda} \right)^2} + c \quad (2.9)$$

Table 2.1 shows the values of the nine coefficients for those atomic species which are most important in the context of this thesis. The resulting curves for $f^0(\sin \vartheta / \lambda)$ are visualized in Fig. 2.1. From these values, the structure factor of a pure crystalline material can now be calculated. For quaternary materials such as $\text{Ga}_x\text{In}_{1-x}\text{As}_y\text{P}_{1-y}$, which will play an important role in Part III, it can be calculated via linear interpolation (*Vegard's law* [Vin21]) from the corresponding binary materials:

$$\chi_{\mathbf{h}} = xy \chi_{\mathbf{h}}^{\text{GaAs}} + x(1-y) \chi_{\mathbf{h}}^{\text{GaP}} + (1-x)y \chi_{\mathbf{h}}^{\text{InAs}} + (1-x)(1-y) \chi_{\mathbf{h}}^{\text{InP}} \quad (2.10)$$

With absorption included, the refractive index can now be written as

$$n = 1 + \frac{\chi_0}{2} = 1 - \delta + i\beta. \quad (2.11)$$

At X-ray frequencies, δ is of the order of $10^{-6} - 10^{-5}$ for most materials, and β is typically one to two orders of magnitude smaller. For easy reference, the values for some important semiconductors and for $\lambda = 1.54 \text{ \AA}$ are given in table 2.2.

atom	a_1	a_2	a_3	a_4	b_1	b_2	b_3	b_4	c
^{15}P	6.4345	4.1791	1.78	1.4908	1.9067	27.157	0.526	68.1645	1.1149
^{31}Ga	15.2354	6.7006	4.3591	2.9623	3.0669	0.2412	10.7805	61.4135	1.7189
^{33}As	16.6723	6.0701	3.4313	4.2779	2.6345	0.2647	12.9479	47.7972	2.531
^{49}In	19.1624	18.5596	4.2948	2.0396	0.5476	6.3776	25.8499	92.8029	4.9391

Table 2.1: Coefficients of approximation (2.9) for the atomic form factors, as used for most of the practical calculations to be shown in later chapters. [Wil95]

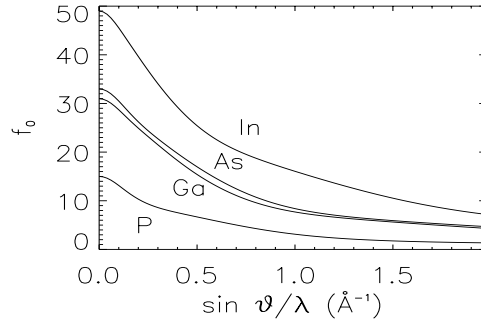


Figure 2.1: Analytical approximation for the atomic form factor $f_0(\sin \vartheta / \lambda)$, calculated for four different atoms with the help of the coefficients given in Table 2.1.

To conclude this section, let us mention that with these values of the refractive index the effect of refraction upon transmission of an X-ray beam through the interface between two materials can be calculated via *Snell's law*:

$$n_1 \cos \alpha_1 = n_2 \cos \alpha_2. \quad (2.12)$$

Just like in the case of visible light optics, total reflection occurs when the beam hits the interface between a denser and a less dense material at a small angle α_1 , more exactly when $\cos \alpha_1 < \frac{n_2}{n_1}$ (< 1). The difference is that, since n is generally below 1 at X-ray frequencies, the vacuum has a *higher* optical density for X-rays than any material, and total *external* reflection occurs when X-rays hit the surface of any material at a small angle.

Another topic which is common to the different scattering theories to be presented shortly is the polarization factor:

$$C = \begin{cases} 1 & \text{for s-polarization} \\ |\cos(2\vartheta)| & \text{for p-polarization} \end{cases} \quad (2.13)$$

When the X-ray beam has its electric amplitude vector \mathbf{E} in the scattering plane (is p-polarized) the measurable intensity is reduced by a factor $|\cos(2\vartheta)|^2$ with respect to the case of s-polarization (\mathbf{E} -vector perpendicular to the scattering plane). This is the reason why all the experiments to be presented in this work were done in s-polarization geometry. Therefore, the factor C didn't have to be taken into account in the corresponding calculations.

Material	δ	β
Si	7.575×10^{-6}	1.779×10^{-7}
SiC	1.049×10^{-5}	1.785×10^{-7}
GaP	1.184×10^{-5}	3.349×10^{-7}
InP	1.356×10^{-5}	1.166×10^{-6}
GaAs	1.456×10^{-5}	4.477×10^{-7}
InAs	1.554×10^{-5}	1.180×10^{-6}

Table 2.2: Values of δ and β , calculated at $\lambda=1.54\text{\AA}$ for some important semiconductors materials.

2.2 From the dynamical to the kinematical theory of X-ray diffraction

The Maxwell equations in the SI-system of units read

$$\nabla \cdot \mathbf{D} = \varrho_f(\mathbf{r}) \quad \nabla \times \mathbf{E} = -\frac{\partial \mathbf{B}}{\partial t} \quad (2.14)$$

$$\nabla \cdot \mathbf{B} = 0 \quad \nabla \times \mathbf{H} = \frac{\partial \mathbf{D}}{\partial t} \quad (2.15)$$

where ϱ_f is the density of free charges (net balance of positive minus negative charges), which must not be mixed up with the density of electrons ρ . These equations are completed by the material equations $\mathbf{B} = \mu\mu_0\mathbf{H}$ and $\mathbf{D} = \epsilon\epsilon_0\mathbf{E}$, with electric permittivity ϵ and magnetic permeability μ . We will assume that the material is non-magnetic ($\mu(\mathbf{r}) \equiv 1$), and does not contain any free charges ($\varrho_f = 0$). This leads to the following differential equation for the propagation of a plane electromagnetic wave (wave vector \mathbf{K}):

$$(\Delta + K^2) \mathbf{E}(\mathbf{r}) = \text{grad div } \mathbf{E}(\mathbf{r}) - K^2 \chi(\mathbf{r}) \mathbf{E}(\mathbf{r}) \quad (2.16)$$

Defining the potential V as $\hat{V}\mathbf{E}(\mathbf{r}) = \text{grad div } \mathbf{E}(\mathbf{r}) - K^2 \chi(\mathbf{r}) \mathbf{E}(\mathbf{r})$ allows to write the wave equation (2.16) in the form of a *Helmholtz equation*

$$(\Delta + K^2) \mathbf{E}(\mathbf{r}) = V(\mathbf{r}) \mathbf{E}(\mathbf{r}), \quad (2.17)$$

In many cases the term $\text{div } \mathbf{E}(\mathbf{r}) = 0$ in (2.16) is zero or negligibly small [HPB98]. The equation then decouples into independent scalar equations for the three components of $\mathbf{E}(\mathbf{r})$, and the potential becomes

$$V(\mathbf{r}) = -K^2 \chi(\mathbf{r}) \quad (2.18)$$

Equation (2.17) can be solved formally with the Green function method by writing

$$\mathbf{E}(\mathbf{r}) = \mathbf{E}_0(\mathbf{r}) + \int G(\mathbf{r} - \mathbf{r}') V(\mathbf{r}') \mathbf{E}(\mathbf{r}') d^3 r', \quad (2.19)$$

or more shortly in Dirac notation

$$|E\rangle = |E_0\rangle + GV|E\rangle, \quad (2.20)$$

where E_0 is a solution of the *homogeneous* equation $(\Delta + K^2)E_0(\mathbf{r}) = 0$, and $G(\mathbf{r} - \mathbf{r}')$ represents the *Green function* for the operator $(\Delta + K^2)$, i.e. a function which satisfies

$$(\Delta + K^2) G(\mathbf{r} - \mathbf{r}') = \delta(\mathbf{r} - \mathbf{r}'). \quad (2.21)$$

It is well known that the outgoing Green function for the operator $(\Delta + K^2)$ is given by $G(\mathbf{r} - \mathbf{r}') = -e^{iK|\mathbf{r} - \mathbf{r}'|}/4\pi|\mathbf{r} - \mathbf{r}'|$, and can be simplified even further in the Fraunhofer approximation [HPB98]. Nevertheless, solving (2.19) remains a difficult problem. The difficulty lies in the fact that the unknown function $\mathbf{E}(\mathbf{r})$ appears on both sides of the equation. The total wave field \mathbf{E} consists of the sum of the incident wave \mathbf{E}_0 and the scattered wave. The scattered wave, in turn, depends not just on E_0 , but on the complete wave field E , since a wave can be scattered more than once.

It is in principle possible to remedy this problem by writing the solution of (2.19) in the form of a Born series (given here in Dirac notation):

$$|E\rangle = |E_0\rangle + \sum_{n=1}^{\infty} (GV)^n |E_0\rangle. \quad (2.22)$$

However, this road is rarely explored in practice, since the series in (2.22) generally converges very slowly [HPB98]. Therefore, several other strategies have been developed to solve (2.17).

Dynamical theory: The dynamical theory of X-ray diffraction has been derived at the beginning of the 20th century in two different ways by Darwin [Dar14b] and Ewald [Ewa13, Ewa16a, Ewa16b, Ewa17], and has later been reformulated by Laue [Lau31]. More recent presentations of the theory can be found in [BC64, Pin78]. It is a theory for the propagation of electromagnetic waves inside a medium, and is based on the fact that the susceptibility of a crystalline material with translational symmetry can be expressed as a discrete Fourier sum:

$$\chi(\mathbf{r}) = \sum_{\mathbf{g}} \chi_{\mathbf{g}} e^{i\mathbf{g}\cdot\mathbf{r}}. \quad (2.23)$$

To solve the combination of (2.17), (2.18) and (2.23) one makes use of a *Bloch wave ansatz*, which states that the amplitude of a wave propagating in a periodic medium must have the same periodicity as the medium itself:

$$\mathbf{E}(\mathbf{r}) = \mathbf{E}^0(\mathbf{r}) e^{i\mathbf{k}_0 \cdot \mathbf{r}} = e^{i\mathbf{k}_0 \cdot \mathbf{r}} \sum_{\mathbf{g}} \mathbf{E}_{\mathbf{g}} e^{i\mathbf{g} \cdot \mathbf{r}}. \quad (2.24)$$

With the help of (2.24) the differential equation (2.16) can be transformed into a system of algebraic equations for the amplitudes of the waves:

$$\sum_{\mathbf{g}} e^{i\mathbf{k}_{\mathbf{g}} \cdot \mathbf{r}} \left[(K^2 - \mathbf{k}_{\mathbf{g}}^2) \mathbf{E}_{\mathbf{g}} + K^2 \sum_{\mathbf{p}} \chi_{\mathbf{g}-\mathbf{p}} \mathbf{E}_{\mathbf{p}} \right] = 0, \quad (2.25)$$

where the individual wave vectors $\mathbf{k}_{\mathbf{g}}$ are defined by $\mathbf{k}_{\mathbf{g}} = \mathbf{k}_0 + \mathbf{g}$. In order this Fourier series to be zero, the terms in brackets must vanish individually. This leads to an infinite system of equations in which the amplitudes $\mathbf{E}_{\mathbf{g}}$ of all components of the wave field are coupled. The system is particularly easy to solve in cases where only very few of the amplitude coefficients are different from zero. The most important is the *two-beam case*, in which only the incident wave \mathbf{E}_0 and one diffracted wave \mathbf{E}_h have significant amplitudes. In this case, (2.25) can be reduced to a system of two algebraic equations which relate the amplitudes $\mathbf{E}_0, \mathbf{E}_h$ to the susceptibility components χ_0, χ_h and $\chi_{\bar{h}}$:

$$\begin{aligned} \{K^2(1 + \chi_0) - \mathbf{k}_0 \mathbf{k}_0\} \mathbf{E}_0 + K^2 C \chi_{\bar{h}} \mathbf{E}_h &= 0 \\ K^2 C \chi_h \mathbf{E}_0 + \{K^2(1 + \chi_0) - \mathbf{k}_h \mathbf{k}_h\} \mathbf{E}_h &= 0 \end{aligned} \quad (2.26)$$

In order the system (2.26) to have non-trivial solutions for $\mathbf{E}_0, \mathbf{E}_h$ the determinant of the coefficient matrix must be zero. We define the *deviation parameters* ξ_0, ξ_h as $\xi_0 = \frac{1}{2K} [\mathbf{k}_0 \mathbf{k}_0 - K^2(1 + \chi_0)]$ and $\xi_h = \frac{1}{2K} [\mathbf{k}_h \mathbf{k}_h - K^2(1 + \chi_0)]$, which represent the (normalized) difference in squared length between the actual wave vectors in the medium, \mathbf{k}_0 and \mathbf{k}_h , and the vacuum wave vector length corrected by the average index of refraction, nK . One then arrives at the condition that the wave vectors $\mathbf{k}_0, \mathbf{k}_h$ must lie on the *dispersion surface* in reciprocal space [BC64]:

$$\xi_0 \xi_h = \frac{1}{4} K^2 C^2 \chi_h \chi_{\bar{h}}. \quad (2.27)$$

For waves fulfilling this condition, the relative diffracted intensity follows from (2.26) via

$$\frac{\mathbf{E}_h}{\mathbf{E}_0} = \frac{2\xi_0}{C \chi_{\bar{h}} K} = \frac{C \chi_h K}{2\xi_h} = \sqrt{\frac{\xi_0 \chi_h}{\xi_h \chi_{\bar{h}}}}. \quad (2.28)$$

The Distorted Wave Born Approximation: A solution of (2.19) in terms of a series approach similar to (2.22) becomes feasible in cases where the potential $V(\mathbf{r})$ can be split into a main part V_A and a small disturbance V_B :

$$V = V_A + V_B \quad (2.29)$$

Instead of (2.17), we then use the wave equation in the form $(\Delta + K^2 - V_A)\mathbf{E}(\mathbf{r}) = V_B \mathbf{E}(\mathbf{r})$ and replace (2.20) by

$$|E\rangle = |E_0\rangle + G_A V_B |E\rangle, \quad (2.30)$$

where G_A is now the Green function for the new operator $(\Delta + K^2 - V_A)$, and $|E_0\rangle$ is an exact solution of the corresponding homogeneous equation $(\Delta + K^2 - V_A)|E_0\rangle = 0$. Equation (2.30) can now be solved iteratively with a *Distorted wave Born series* [Vin82]:

$$|E\rangle = |E_0\rangle + |E_1\rangle + |E_2\rangle + \dots \quad (2.31)$$

with the recurrence relation

$$|E_{n+1}\rangle = G_A V_B |E_n\rangle$$

An approximate solution for the wave field $E(\mathbf{r})$ can be obtained by truncating the series (2.31) after a small number of terms. A *Distorted Wave Born approximation* (DWBA) of first order is defined via $|E\rangle = |E_0\rangle + |E_1\rangle$, and similarly for higher orders.

A DWBA of first order has been successfully applied in particular to the interpretation of diffuse scattering from roughnesses of single layers, both in X-ray reflectivity (XRR) [SSG88] and in grazing incidence diffraction (GID) [Vin82]. The method has subsequently been transferred to the study of multilayers by XRR [HB94] and GID [BTP95]. A second-order DWBA has also been introduced in the literature for XRR [dB94] and diffraction [BG95].

The usefulness of the DWBA approach depends on the clever splitting $V = V_A + V_B$. In a multi-layer structure, for instance, V_A can be chosen to represent the variation of the (laterally averaged) refractive index with depth, and V_B to additionally introduce roughness at the interfaces and/or the crystalline structure inside the single layers [BG95]. Then, one can find the *distorted wave* \mathbf{E}_0 , the wave field under the pure influence of reflection from and transmission through the multilayer interfaces, by *Abelès' matrix formalism* [Abe50]. The diffraction by the crystal lattice is additionally taken into account by including the second term of the Born series (2.31), namely $G_A V_B |E_0\rangle$.

Kinematical theory: The *kinematical theory* of X-ray scattering [Dar14a, AKK74, Kri96] consists in truncating the series in (2.22) after the first term:

$$|E\rangle = |E_0\rangle + GV|E_0\rangle \quad (2.32)$$

With this simplification (and in *Fraunhofer approximation*), the diffracted intensity can be calculated via a simple Fourier transform of the scattering potential V (2.18):

$$I(\mathbf{Q}) \sim K^2 |S(\mathbf{Q})|^2 = K^2 \left| \int_V \chi(\mathbf{r}) e^{-i\mathbf{Q} \cdot \mathbf{r}} d^3 r \right|^2. \quad (2.33)$$

The kinematical theory contains three main simplifications. First, the refraction of X-rays upon transmission through the sample surface (and inner interfaces) is neglected. Second, the weakening of the incident wave by the scattering process (extinction) is ignored, and every part of the sample is taken to be illuminated with the same incident intensity. Third, every incident wave is assumed to be scattered at most once, and multiple scattering is not considered.

The fact of disregarding extinction obviously violates the law of energy conservation. Nevertheless, the theory can be applied very successfully in many cases - in fact, the whole field of crystal structure analysis is essentially based on the kinematical approximation. It is often applicable when the scattering by the object is weak, and in particular for high-angle diffraction from small crystals, thin crystalline layers and samples with a high mosaicity or an otherwise low crystalline perfection.

We will see in Part III that our experimental data can in general be explained very satisfactorily by an approach which is essentially based on a semi-kinematical theory. Especially in the case of grazing

incidence diffraction the effects of refraction and of reflection from the sample surface additionally need to be taken into account. Therefore, our method of choice will be a first order DWBA with the potential V_A being defined simply as $V_A = n$, the average refractive index inside the structure. In this case, the *distorted waves* in the sample differ from the incident waves via a refraction correction for the component of their wave vector \mathbf{k} which is perpendicular to the sample surface:

$$k_z = -\sqrt{(nK)^2 - |\mathbf{K}_{||}|^2} \quad (2.34)$$

The expression for the diffracted intensity becomes [Dos87]

$$I(\mathbf{Q}) \sim K^2 |t(\alpha_i) S(\mathbf{k}_f - \mathbf{k}_i) t(\alpha_f)|^2, \quad (2.35)$$

where α_i, α_f are the incidence and exit angle with respect to the surface, and $t(\alpha)$ is the *Fresnel transmission function* [BW80] (see Fig. 2.2):

$$t(\alpha) = \frac{2 \sin \alpha}{\sin \alpha + \sqrt{n^2 - \cos^2 \alpha}} = \frac{2\mathbf{K}_z}{\mathbf{K}_z + \mathbf{k}_z}. \quad (2.36)$$

In Chapter 5 we will derive expressions for the structure amplitude $S(\mathbf{Q})$ of strained surface gratings. The simulation of diffracted intensities in later chapters will then always be based on (2.35). Thus, the formula for the structure amplitude must not be evaluated for the argument $\mathbf{Q} = \mathbf{K}_f - \mathbf{K}_i$, the momentum transfer in vacuum, but for the difference $\mathbf{k}_f - \mathbf{k}_i$ of wave vectors *inside* the medium (we do not use the symbol \mathbf{q} here since it is reserved for other purposes in Chapter 5). The difference is particularly noticeable in the case of grazing incidence diffraction, which we discuss now.

2.3 Peculiarities of grazing incidence diffraction

Grazing incidence diffraction is the extreme case of non-coplanar scattering [MEC79]. The scattering vector \mathbf{Q} lies mainly in the plane of the sample surface, with only a very little vertical component \mathbf{Q}_z . The wave vectors \mathbf{K}_i and \mathbf{K}_f form very small angles α_i, α_f with the surface. The diffracting lattice planes are thus perpendicular to the sample surface. For a [001]-oriented sample surface, this corresponds to scattering in the vicinity of reflections (H, K, L) with $L = 0$. The small angles α_i, α_f lead to some special experimental effects and allow particular theoretical approximations which we now discuss.¹

The fact that at X-ray frequencies the refractive index of any material is slightly less than 1 ($\delta = \text{Re}(1 - n) \approx 10^{-5}$) leads to the phenomenon of total external reflection of an X-ray beam which impinges on a surface at an angle below the critical angle α_c . This angle is of the order of some tenths of degrees for typical materials and wavelengths. It is related to δ , the average electron density ρ_0 and/or the average susceptibility χ_0 of the material by the equations

$$\alpha_c = \sqrt{2\delta} = \lambda \sqrt{r_e / \pi \cdot \rho_0} = \sqrt{-\chi_0}. \quad (2.37)$$

The vertical component of the transmitted wave vector, given by (2.34) in the general case, can be approximated for small α_i as

$$k_z = \sqrt{(nK)^2 - |\mathbf{K}_{||}|^2} \approx K \sqrt{\alpha_i^2 + \chi_0} = K \sqrt{\alpha_i^2 - 2\delta + 2i\beta} \quad (2.38)$$

For α_i close to or below α_c the component k_z becomes complex: The wave is exponentially damped below the sample surface, it forms an *evanescent wave* [Dos87]. The depth at which the intensity of the incident wave is reduced by a factor $1/e$ is called the *penetration depth* Λ_i . It is determined by the imaginary component of k_z and can be expressed as a function of the material parameters δ, β :

$$\Lambda_i(\alpha_i) = \frac{1}{2 \text{Im}(k_z)} = \frac{\lambda}{2\sqrt{2\pi}} \sqrt{\frac{1}{\sqrt{(\sin^2 \alpha_i - 2\delta)^2 + 4\beta^2} - (\sin^2 \alpha_i - 2\delta)}}. \quad (2.39)$$

¹The formulae discussed in this Section are valid whenever the angles α_i and/or α_f are small. Therefore, the discussion applies not only to the case of grazing incidence diffraction, but also to coplanar diffraction in extremely asymmetrical cases and to X-ray reflectivity.

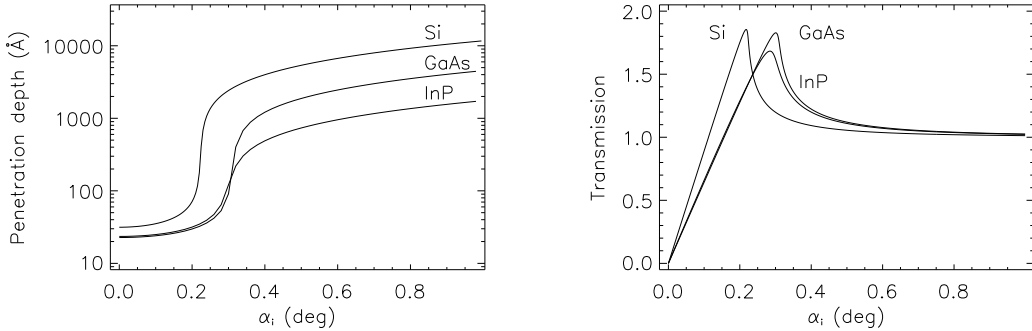


Figure 2.2: Left: Penetration depth $\Lambda_i(\alpha_i)$ of X-rays ($\lambda = 1.54 \text{ \AA}$) for three important semiconductor materials. Right: Fresnel amplitude transmission function $|t_s(\alpha_i)|$ (see (2.36)) for the same materials, calculated for $\lambda = 1.54 \text{ \AA}$ and s-polarization. The function has its maximum at $\alpha_i = \alpha_c$, the critical angle of the respective material.

Typical shapes of this curve at $\lambda = 1.54 \text{ \AA}$ are demonstrated in Fig. 2.2 with the example of three important semiconductor materials. For $\alpha_i = 0$ the value of Λ_i becomes independent of the wavelength, and is determined by the material's average electron density alone: $\Lambda_i(0) = \lambda/(4\pi\alpha_c) = 1/(4\sqrt{\pi r_e \rho_0})$, which is of the order of 50 Å for many materials.

Above the critical angle, a limiting expression for Λ_i can be obtained for $(\alpha_i - 2\delta) \gg 2\beta$:

$$\Lambda_i(\alpha_i) \approx \frac{\lambda}{2\sqrt{2}\pi} \sqrt{\frac{(\sin^2 \alpha_i - 2\delta)}{2\beta^2}} \approx \frac{\lambda}{4\pi} \frac{(\sin \alpha_i)}{\beta}. \quad (2.40)$$

We thus recover the familiar expression for the absorption coefficient, $\mu (= 1/\Lambda_i) = 4\pi\beta/\lambda$, corrected for the projection of the beam propagation direction onto the inward surface normal ($\sin \alpha_i$).

In a scattering experiment, not only the attenuation of the incident wave, expressed in terms of the penetration depth, is of interest. A similar effect takes place when the scattered wave \mathbf{k}_f leaves the sample through the surface. The relevant quantity is therefore not Λ_i alone, but the *information depth* Λ [PMR93] (also called *scattering depth* [Dos87]):

$$\frac{1}{\Lambda(\alpha_i, \alpha_f)} = \frac{1}{\Lambda_i(\alpha_i)} + \frac{1}{\Lambda_f(\alpha_f)} \quad (2.41)$$

The fact that α_i and α_f enter symmetrically into this expression can be viewed as a consequence of the reciprocity theorem in optics [Dos92]. The effect is visible in Fig. 2.3, which shows Λ_i , Λ_f and the resulting Λ as a function of α_i , for two different fixed \mathbf{Q}_z . The exit angle α_f is uniquely determined by the combination of α_i and \mathbf{Q}_z , and is plotted on a second horizontal axis. It becomes clear from this figure that the information depth does not grow monotonously with α_i , but can increase only up to a certain maximum value, and then decreases again under the opposite influence of α_f . For very small \mathbf{Q}_z , this decay even occurs before the increase due to α_i can take place, so that the middle of the curve is a minimum instead of a maximum. For surface-sensitive X-ray investigations it is very important to know the exact form of these functions in order to systematically probe a structure at different depths below the surface. To conclude the discussion of the information depth, let us mention that it can equivalently be expressed via the imaginary part of the scattering vector \mathbf{Q} : $1/\Lambda(\alpha_i, \alpha_f) = 2 \operatorname{Im}(\mathbf{Q}_z) = 4\pi/\lambda \operatorname{Im} \left(\sqrt{\sin^2 \alpha_i + \chi_0} + \sqrt{\sin^2 \alpha_f + \chi_0} \right)$. For the practical investigation of thin films and surface nanostructures, grazing incidence diffraction presents three significant advantages. First, by choosing small angles of incidence one can restrict the sensitivity of the probing X-ray to a very thin layer below the surface, of the order of some 10 nm. It is even possible to study the evolution of sample properties as a function of depth below the surface by systematically performing a measurement for a series of different α_i [LBP99]. Second, the Fresnel transmission functions $t(\alpha)$ have a maximum at the critical angle α_c (see Fig. 2.2, right graph). Therefore, the measurable

intensity is enhanced by up to a factor of 4 in the case of a single layer (see (2.35)), which is a significant advantage since the diffracted signal from thin layers is generally weak. Third, grazing incidence is sensitive to the lattice spacing along a lateral direction. This fact is particularly helpful to isolate the influence of the lateral strain component in the course of a complete strain investigation [BL99], as we will see in Section 5.5. For these three reasons, a grazing incidence diffraction study will be an essential ingredient of all our experimental strain investigations of surface gratings in Part III of this work.

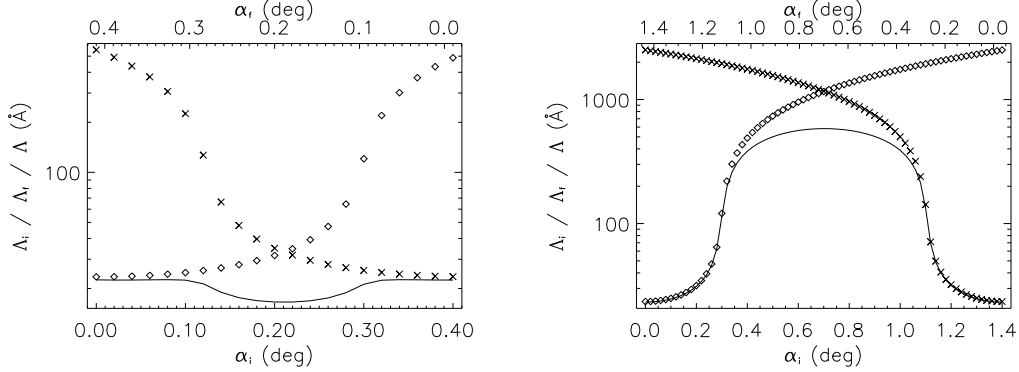


Figure 2.3: Penetration depths $\Lambda_i(\alpha_i)$ (diamond symbols) and $\Lambda_f(\alpha_f)$ (crosses), and the resulting information depth $\Lambda(\alpha_i, \alpha_f)$ (full line) calculated for InP according to (2.39) and (2.41) for fixed vertical momentum transfer Q_z and an X-ray wavelength of $\lambda=1.54 \text{ \AA}$ (for which the critical angle is $\alpha_c = 0.298^\circ$). Left: $Q_z = 0.03 \text{ \AA}$, right: $Q_z = 0.10 \text{ \AA}$.

Part II

**Lattice distortions on a scale of some
micrometers:
Direct observation by X-ray rocking
curve imaging**

Chapter 3

X-ray rocking curve imaging: Principle

In this Chapter we describe a new method to investigate the crystalline quality, its spatial variation, the defect distribution, lattice tilts, and the sample curvature in semiconductor wafers and other kinds of crystalline samples. The method combines classical X-ray diffractometry with additional spatial resolution in the range of micrometers. Furthermore, we present an equipment and a data analysis software package which have been installed at the ID19 beamline of the ESRF to implement this method.

Chapter 4 will show first results of the application of our method, demonstrated with the example of GaAs and SiC wafers. The method is, however, perfectly general and can be applied to all types of crystalline structures, like microelectronic devices or high-power semiconductor lasers under operation.

3.1 Introduction and motivation

The crystalline quality of semiconductor wafers is crucial for the fabrication of all kinds of microelectronic and optoelectronic devices. Lattice distortions which are present in a substrate induce defects in the epitaxial layers that are grown on top of them. Therefore, bad wafer quality can lead to poor performance of the entire device. Distortions can be generated in a whole series of different steps in the wafer fabrication process: crystal pulling, crystal slicing and etching, wafer polishing, thermal processing, packaging and transport. They lead to different effects in the wafer: macroscopic curvature (also called *warp*), microscopic curvature (lattice tilts) and defects like dislocations, which all lower the local crystalline quality. For improvements of wafer fabrication technology it is essential to have non-destructive methods for wafer quality inspection and defect analysis. In order to resolve the microscopic causes of a degradation in crystalline quality, the method should have a spatial resolution of the order of the order of some μm .

Various experimental methods are available to investigate wafer quality in general. Firstly, X-ray topography can be used to visualize local defects in the crystal lattice [JK88]. Secondly, high resolution X-ray diffractometry is an integral, non-local technique and is conventionally used to assess the *mean* crystalline quality via the rocking curve half width. It achieves high *angular* - or equivalently reciprocal space - resolution, but integrates *spatially* over the illuminated area on the sample surface. Finally, with *total reflection X-ray fluorescence (TXRF)* it is possible to measure impurity concentrations on the surface of semiconductor wafers with a very high accuracy [CNM99].

The most appropriate method for our purpose, namely to measure the overall crystalline perfection of a semiconductor wafer in a *quantitative* way, is certainly X-ray diffraction. However, in order to judge the *local* rocking curve FWHM (taken as a local crystalline quality parameter), one needs a way to additionally realize *spatial* resolution in the diffraction measurement, while not losing the advantage of high angular resolution. Various X-ray methods have been explored in the past. They can be roughly grouped into two categories: methods which achieve spatial resolution in the incident beam, and methods which achieve resolution on the detector side. We will briefly describe the methods which have been known so far. Then we present our own alternative approach which in a certain sense recombines different elements of several precursor techniques.

3.2 Methods to achieve spatial resolution with X-rays

3.2.1 Spatial resolution on the incident side: slits or focusing

A simple possibility to obtain a spatially resolved incident X-ray beam is to restrict it in size by mechanical slits. This approach is certainly inefficient in terms of X-ray intensity, but is instrumentally very uncomplicated. The sample surface can then be scanned by translation of the sample holder with respect to the fixed incident beam — a procedure which has been used by different groups to map whole wafers [FKK97, GMM97].

Commercial equipment is available which implements this procedure. It is based on conventional X-ray tubes and allows to obtain a spatial resolution of about 1 mm^2 . In this way a macroscopic lattice curvature can be detected by measuring the angular position of a Bragg peak as a function of the lateral position. The full width at half maximum of the rocking curve is taken as a quality parameter for the local crystalline perfection of the wafer crystal. The moderate spatial resolution which can be achieved does not allow, however, to correlate the measured macroscopic crystalline quality with the underlying microscopic effects.

Furthermore, these instruments can be operated in Bragg geometry (reflection mode) only, due to the limited X-ray flux which is not sufficient for transmission through thick samples. Therefore the diffracted signal originates predominantly from the region near the sample surface, whose extension is characterized by the extinction length of the X-ray beam, which is of the order of a few μm . This limited penetration depth sets an instrumental lower limit to the measurable rocking curve half width, and thus an upper limit to the crystalline quality which can be found by such a measurement. In summary, the situation at this kind of instruments is such that the measured signal does not necessarily give a precise image of the sample's crystalline properties, but is often strongly distorted by instrumental effects.

A second possibility is beam focusing. This allows to avoid the high loss of intensity caused by the slits. X-rays are much more difficult to focus than visible light, due to the smaller variations in refractive indices at X-ray frequencies. However, focusing is feasible: Bragg-Fresnel zone plates (see Fig. 3.1) are in widespread use nowadays, and even refractive lenses have been demonstrated in practice recently [SKS96]. The main drawback of these methods is that they are technologically very demanding. Furthermore, the focused beam has a higher angular divergence than the primary beam.

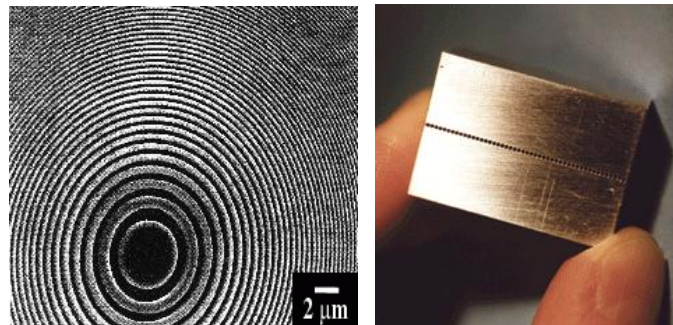


Figure 3.1: Methods of focusing an X-ray beam: Bragg-Fresnel zone plates (left) or refractive lenses (right). (ESRF information office)

A third alternative, beam *compression*, has been explored only recently. It consists in capturing an incident large beam inside an X-ray waveguide structure. After the beam has travelled through the conducting layer it emerges again from the lateral end of the structure. Its intensity is then concentrated in a cross section corresponding to the layer thickness of the waveguide structure, which is of the order of some 100 nm. A one-dimensional focusing of an X-ray beam has been achieved in this way [Ced99, Clo99, Pfe99]; a two-dimensional version of the same method is under study [LCC98].

Instead of coupling the incident beam into the waveguide by *reflection*, as done in these studies, it is also possible to achieve coupling by *diffraction* in a crystalline waveguide structure. The advantage is that the projection of the incident beam cross section onto the waveguide is much smaller, for geometrical reasons. Preliminary investigations performed in the course of the present work have shown, however, that this method is not appropriate for our purposes. From the tests it became clear that the waveguide accepts a large *spatial* width but selects a very narrow *angular* divergence of the incident beam. The gain in intensity via spatial compression of the beam is offset by a loss due to an enhanced angular selectivity; the major part of incident photons is simply not coupled efficiently into the waveguide structure. Therefore, this option was momentarily abandoned in favour of an alternative technique.

3.2.2 Spatial resolution on the exit side: area detectors

The three methods described above allow to measure an X-ray diffraction signal from a restricted area on the sample surface, some μm in size. In the context of our objective, namely to monitor the crystalline quality across the whole sample area, they suffer from one common drawback: They are inherently slow, since they are scanning methods and need to measure the rocking curves for one spot on the sample surface after the other. For large sample sizes, this leads to long measuring times.

There is an alternative, which yields information for a whole spatial region in one single “shot”: X-ray *diffraction topography* or simply *topography*. It consists in placing a sample into a spatially extended X-ray beam with as low a divergence as possible (such as the beam of ID19 at the ESRF, $1.5 \times 4 \text{ cm}^2$ in size), and to record the spatial variation of diffracted intensity with the help of a film or, more recently, a digital camera. In this way topography makes use of the full size of the incident beam, illuminating large parts of the sample simultaneously.

Different experimental techniques for topography in a “white” and/or monochromatic X-ray beam have been developed in the past (see [Bar45, Lan58, Lan59, Aut77, Lan78, BT98]). They reveal directly different kinds of defects in a (relatively perfect) crystalline structure: dislocations, domain walls, grain boundaries and holes in crystals and, more recently, quasi-crystals [Man98].

Topography with synchrotron radiation is fascinating in that it is a very fast technique (the illumination times are generally of the order of seconds or below) which allows not only to detect but also to *visualize* defects and the surrounding strain fields in crystal lattices. However, it is not entirely adapted to our purposes, since it does not allow to easily draw *quantitative* conclusions concerning crystal quality in terms of the rocking curve half width and of the sample curvature.

3.2.3 Application to wafers

To summarize the two preceding section, one can say that two classical techniques are in common use for X-ray characterization of crystal qualities. The first is X-ray diffractometry, which measures quality via the rocking curve FWHM, and can be made spatially selective, but thereby usually becomes inefficient in terms of X-ray intensity, delicate to handle and/or very slow. The second is X-ray topography, which allows to visualize individual defects in crystals very rapidly, but can monitor lattice curvature and perfection in a *quantitative* way only with some special care [YMW79]. Furthermore, its use becomes problematic in the case of curved crystals, for which it is not easy to fulfil the Bragg condition simultaneously for large areas on the sample surface.

In order to reach our aim of monitoring the local crystalline quality of semiconductor wafers, we therefore need to combine the advantages of both methods. What is required is a technique that is (a) quantitative and (b) fast, which (c) has a microscopic spatial resolution and (d) can be applied also to curved samples.

3.3 A new method: μm -resolved X-ray diffraction by a combination of diffractometry and topography

To this end, we have developed a new method which we will call *μm -resolved rocking curve imaging*. It is based on a combination of the characteristics of diffractometry (angular resolution; measurement of

crystalline quality via FWHM) and those of X-ray topography (visualization), and becomes fast thanks to the use of synchrotron X-rays.

3.3.1 Experimental procedure and data reconstruction

The principle is shown in Fig. 3.2, and can be described as follows: The sample is placed into a wide monochromatic X-ray beam on top of a diffractometer. This allows to rotate it around an axis perpendicular to the beam (the ω axis), as well as to translate it horizontally and vertically. A crystallographic reflection is selected, for instance the 220 reflection, and the ω angle scanned over a small angular range, typically some hundredths of a degree. At each step in the scan, an image is recorded with the help of a digital camera, showing the spatial variation intensity in the diffracted beam. Each single image corresponds to a digital version of a classical X-ray topograph for one special sample rotation angle.

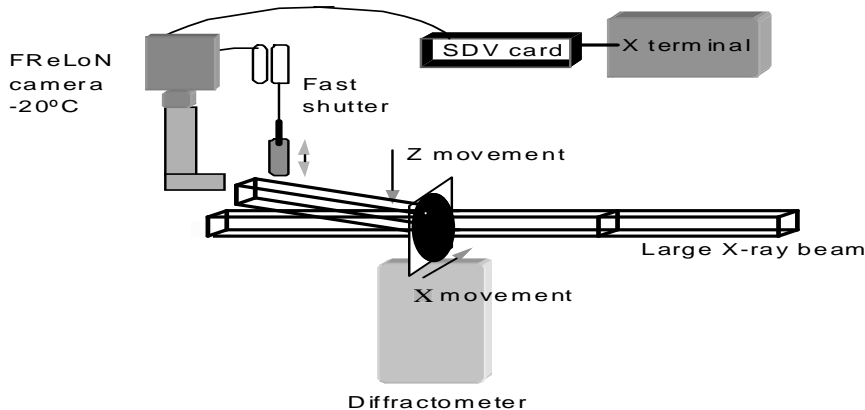


Figure 3.2: Principle of the measurement. [LBH00]

An equipment that implements this procedure has been installed at the ID19 beamline of the ESRF. Due to its length of 145 m from the wiggler source to the experimental hutch this beamline delivers a large and yet highly parallel beam. The maximum spot size on the sample can be as large as $1.5 \times 4 \text{ cm}^2$. The images are recorded by a *FReLoN camera*, a CCD-camera with special noise characteristics and short read-out times that has been developed at the ESRF [LSPvB96]. It is based on a CCD-camera with a field of view of (presently) 1024×1024 pixels. The incident X-rays are converted to visible photons by a converter screen. After this, they are imaged onto the CCD chip by optics systems with variable magnification, which allows to select the pixel size between 1 and $10 \mu\text{m}$.

This combination of a large homogeneous beam with a two-dimensional detector allows to record the signal from a larger number of spots on the sample surface simultaneously. This makes it possible to accelerate the measurement considerably (by a factor 10^6 in the ideal case) compared to the methods described in the previous section. Furthermore, the resolution which can be achieved with the camera is far better than what can be obtained with mechanical slits in the incident beam. The degree of parallelism in the data acquisition is limited only by the maximum field of view of the camera, which is presently 1 cm^2 in the case of $10 \mu\text{m}$ pixel size. When wafers are to be investigated which exceed this size, the sample can be automatically translated in lateral and horizontal direction, and the measurement is repeated until the whole sample surface has been covered.

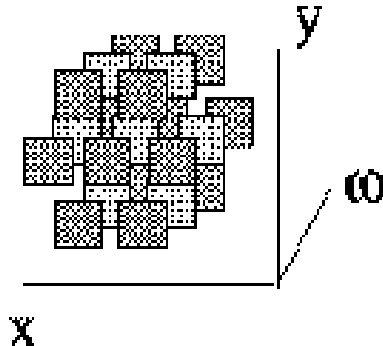


Figure 3.3: *Principle of the data evaluation procedure.* Data are originally recorded as images, i.e. as $I(x, z)$, for a series of sample rotation angles ω . In the analysis they are re-ordered to extract the rocking curves $I(\omega)$ for each spot (x, z) on the sample surface.

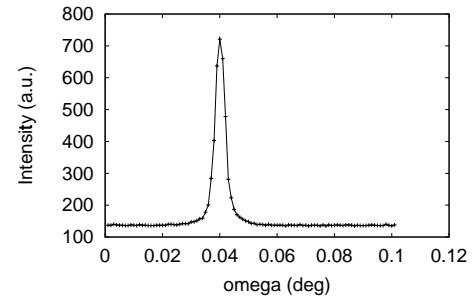


Figure 3.4: *Rocking-curve of a spot on a GaAs-wafer, reconstructed by the mechanism described above from a series of digital topographs.*

The raw result of this measuring procedure is a three-dimensional data field, which contains the diffracted intensity as a function of the horizontal and vertical positions x, y and of the sample rotation angle ω (see Fig. 3.3). The fact that the intensities have been recorded in digital form now displays its full usefulness, since it makes them accessible to quantitative evaluation. The three-dimensional data field is re-ordered according to a certain scheme, in order to reconstruct the rocking curve profile $I(\omega)$ for each (fixed) position (x, z) . A typical example of such a rocking curve, reconstructed from the measurement on a GaAs-LEC-wafer, is shown in Fig. 3.4. The third step of data evaluation consists in extracting the relevant data from each such rocking curve. Parameters of particular interest are (a) the absolute peak intensity, (b) the angular peak position, and (c) its full-width-at-half-maximum (FWHM).

A special program package was written to implement this evaluation scheme and to extract the three relevant parameters consecutively for each pixel in a series of images. Some effort has been invested to make the program insensitive to problems arising in special cases: (1) the peak may be too weak to distinguish it from the noisy background; (2) the angular step of the ω -scan may have been chosen too large to clearly identify a FWHM; or (3) the (apparent) peak may appear at the far left or right end of the angular scan range. All these special cases are recognized and handled as necessary.

The result of the program's operation are three different two-dimensional data fields, namely the peak intensities, peak positions and peak widths, each as a function of pixel positions x and y . They are subsequently stored in binary data format and represented as maps, just like the original images. The peak widths are taken as a crystalline quality parameter, while the peak positions are interpreted in terms of sample curvature.

Let us mention that this method for data evaluation is based on a fact which has been established experimentally by Ferrari et al. [FKK97] in a triple-crystal X-ray diffractometry study on GaAs wafers: The crystal lattice in the wafers is mainly distorted by local lattice *tilts*, and not additionally by variations in the lattice parameter. This is important since it guarantees a clear one-to-one correlation of spots in the detector with spots on the sample. In a material with more or less homogeneous lattice parameter, all regions of the sample diffract at the same total scattering angle $2\vartheta_B$. In other words, although different parts of the sample may be tilted with respect to each other, the diffracted intensity from their main Bragg peaks always reaches the detector in the same angular direction. This is what makes it possible that differences in the rotation angle necessary to put the individual regions into diffraction position can be identified as local lattice tilts.

On the other hand, our data analysis would not be perturbed by strains of an order of magnitude practically relevant to semiconductor wafers ($\epsilon \sim \text{some } 10^{-4}$). Since the camera is mounted close to the sample (~ 10 cm), the deviation of the diffracted beam due to strain amounts to few camera pixels, at maximum. The one-to-one correlation between positions on the wafer surface and camera pixels is thus preserved in

our case. If higher strains occur in a sample, it may become necessary to additionally analyze the direction of the diffracted beam with the help of an analyzer crystal (see section 4.3).

The main remaining practical difficulty in this evaluation scheme consists in the large masses of data which are produced at a rapid pace. A single image contains 2 MB of binary data. If a sample is to be investigated with an angular step width of 0.0002° and a total angular scan range of 0.01° , for instance, then each square centimeter of the sample surface corresponds to 100 MB of data. The total storage space required grows proportionally with the total sample curvature (total scan range), the local crystalline perfection (angular step width) and the sample surface. Theoretically an image can be recorded every 1–2 seconds. This leads to a data flow of 43 GB per day, which can be handled only with state-of-the-art computer equipment. If the analysis is to last not considerably longer than the measurement itself, one furthermore needs to pay particular attention to the numerical efficiency of the evaluation algorithm.

3.3.2 Further analysis and theoretical background

For a more thorough analysis, the experimental data must first be corrected for the camera noise and inhomogeneity. Then, the instrumental dispersion must be accounted for. Finally, the measured rocking curve half widths must be compared with the theoretical ones for non-distorted crystals, in order to obtain information on the actual distortions in the sample. In what follows we go into the details of all three aspects.

In order to correct the raw experimental data $I^{\text{raw}}(x, z)$ for possible inhomogeneities in the camera noise, the camera sensitivity (efficiency), and the incident beam profile, two kinds of corrective data must be recorded in regular intervals during the experiment. On the one hand, the so-called *dark field* $I^{\text{dark}}(x, z)$ represents the intensity “seen” by the camera when the beam shutter is closed and the camera should theoretically record zero intensity. This dark field is due to electronic noise and must be subtracted from the raw data. On the other hand, the so-called *flat field* $I^{\text{flat}}(x, z)$ represents the intensity seen by the detector when the sample is not in the beam path.¹

In the ideal case, the flat field would show a spatially homogeneous, non-zero intensity. Deviations from homogeneity are caused by two factors: variations in the sensitivity of different pixels in the camera, and/or the incident beam profile (see section 1.2). The final formula for the corrected intensities I^{corr} as a function of the raw experimental data I^{raw} is:

$$I^{\text{corr}}(x, z) = \frac{I^{\text{raw}}(x, z) - I^{\text{dark}}(x, z)}{I^{\text{flat}}(x, z) - I^{\text{dark}}(x, z)} \quad (3.1)$$

If the peak position maps are to represent the real sample curvature, then the instrumental dispersion must be calculated and accounted for in the next analysis step. The reason for this becomes clear from Fig. 3.5. It shows the raw results, single images recorded at three different sample ω , of a study performed on a GaAs-LEC-wafer. The pictures do not seem to be homogeneously illuminated; in each single image, only a small zone of the sample diffracts with noticeable intensity. Two different reasons can be responsible for this effect. The most obvious reason is a macroscopic sample curvature (progressive lattice tilt); after rotation of the sample, new areas on the wafer surface come into diffraction condition. The other possible reason is the instrumental *dispersion*, i.e. the fact that different areas in the image are illuminated with slightly different X-ray wavelengths. In addition, geometry plays a role: The beam from the wiggler source reaches the different ends of the sample surface at slightly different angles. Both effects lead to variations in the experimentally observed Bragg angles even for homogeneous, non-curved samples.

In order to account for the dispersion, we need to calculate the effect quantitatively and subtract it from the experimental curvature values. In the case of a vertically diffracting double-crystal analyzer and horizontally diffracting sample (see Fig. 3.6), an elementary derivation leads to the following formula for the

¹This terminology originally stems from the field of X-ray micro-tomography, where the *transmitted* intensity is recorded for a series of sample rotation angles. It is then a simple operation to remove the sample from the beam path and to record the flat field. In our present context, an additional difficulty occurs since we record *diffracted* intensity: When the sample is removed, the detector has to be moved back by $2\theta_B$ into the incident beam direction in order to record the flat field. This operation cannot be performed with sufficient angular precision to correlate a single pixel’s position in the two images. Therefore, in our case the procedure cannot be used to identify sharply localized deviations from homogeneity in the image, e.g. single defective pixels, but only to correct for more slowly varying effects, and especially for the non-homogeneous beam profile.

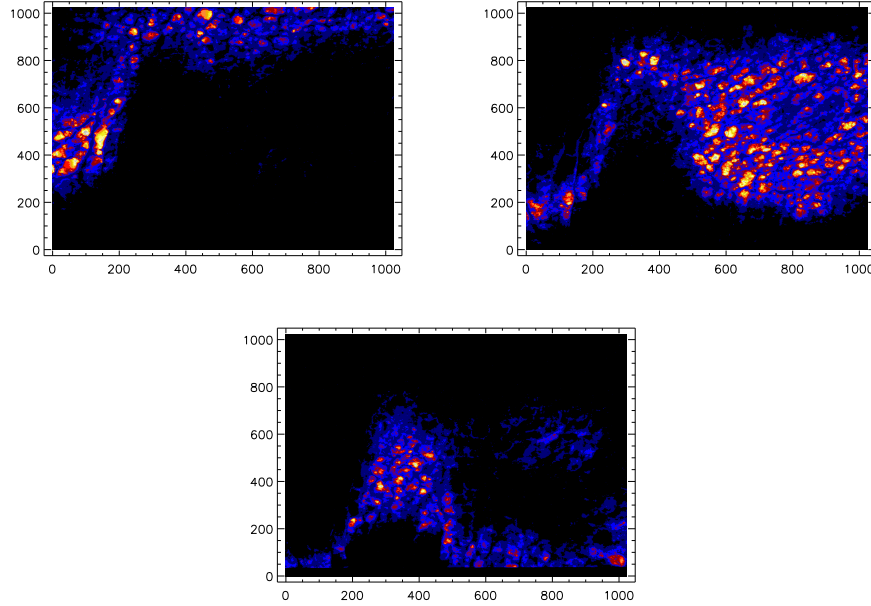


Figure 3.5: Three “snap-shots”, single images taken during an ω -scan on a GaAs-LEC-wafer, recorded with a digital camera (axes are in units of camera pixels, i.e. multiples of $10 \mu\text{m}$ - thus, the total width and height of each image is 1 cm). Symmetrical 220-reflection in Laue geometry; diffraction vector in the horizontal plane; angular step between images: 0.0015° . Due to the sample curvature, only small zones on the sample surface are simultaneously in Bragg position.

variation $\Delta\vartheta$ of the apparent Bragg angle as a function of x and z , the lateral and vertical distance from the center of the image:

$$\Delta\vartheta(x, z) = \frac{z}{L} \tan \vartheta_B + \left[\arccos \left(\frac{x \sin \vartheta_B + L \cos \vartheta_B}{\sqrt{x^2 + z^2 + L^2}} \right) - \vartheta_B \right]. \quad (3.2)$$

L is the distance from the X-ray source to the sample, ϑ_B is the average Bragg angle of the sample, and $\vartheta_B^{\text{mono}}$ the Bragg angle of the monochromator. The first term in (3.2) has its origin in the (slight) variation of wavelengths with height, while the second term describes the geometrical effect. The result of a numerical evaluation of (3.2) for our setup at ID19 and an X-ray energy of 30 keV is shown in the right image of Fig. 3.6. We see that the apparent Bragg angle varies by $\pm 0.005^\circ$ across an image size of 1 cm^2 , due to purely instrumental effects. The combined influence of the two contributions leads to diagonal lines of equal angular shift. If only variations in wavelength were taken into account, these lines would be purely horizontal, while the mere geometrical effects would lead to a strictly vertical line orientation.

The total correction has to be subtracted from all the experimentally measured peak position maps. Concerning the series of single images in Fig. 3.5, a qualitative conclusion can be drawn already now: The instrumental effects alone cannot account for the observed shifts in Bragg angle, since the observation does not follow the clear evolution from the lower left to the upper right end of the image in Fig. 3.6. A remaining macroscopic sample curvature can thus be identified.

The calculation of dispersion effects is important for the interpretation of the peak position maps in terms of sample curvature. In order to also interpret the peak widths correctly in terms of local crystalline quality, the measured data must now be compared with the theoretical values for the rocking curves widths of non-distorted samples.

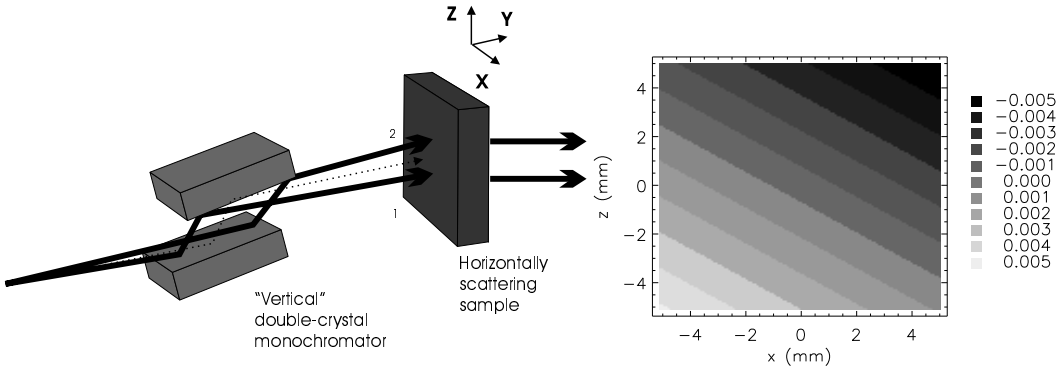


Figure 3.6: *Left:* Scattering geometry for the case of a vertically scattering monochromator and a horizontally scattering sample. The image shows the effect of a slight vertical divergence of the incident beam which, due to the monochromator geometry, leads to slightly different wavelengths $\lambda_1 > \lambda_2$ *Right:* Necessary correction for the peak position map for this geometry and the parameters of the ID19 beamline.

Dynamical scattering theory predicts a Darwin-Prins-curve for the rocking curve profile in the limit of Bragg-diffraction from thick, non-absorbing crystals [BC64, Pin78, Aut93]:

$$I/I_0 = \left| \eta \pm \sqrt{\eta^2 - 1} \right|^2. \quad (3.3)$$

The variable η in (3.3) is the deviation parameter [BC64]:

$$\eta = \frac{-b\Delta\vartheta \sin(2\vartheta) + \chi_0/2 (1-b)}{|C||b|^{\frac{1}{2}} |\chi_h \chi_{\bar{h}}|^{\frac{1}{2}}}, \quad (3.4)$$

where b is the asymmetry factor of reflection \hbar :

$$b = \frac{\gamma_0}{\gamma_h} = \frac{\sin \alpha_i}{\sin \alpha_f}. \quad (3.5)$$

γ_0 and γ_h are the direction cosines of the wave vectors \mathbf{K}_0 , \mathbf{K}_h with respect to the sample's surface normal. They can be equivalently expressed via $\gamma_0 = \sin(\theta_B - \phi)$, $\gamma_h = \sin(\theta_B + \phi)$ (see Fig. 1.8).

The most characteristic feature of (3.3) is that there is a region of total reflection (reflected intensity ratio = 1) in the region $\eta \in [-1, 1]$ around each Bragg peak. The width of this region in an angular scale is called the *Darwin width* w :

$$w = \frac{2C\sqrt{\chi_h \chi_{\bar{h}}}}{\sin 2\vartheta_B} \sqrt{\frac{|\gamma_h|}{\gamma_0}}, \quad (3.6)$$

A similar formula can also be derived for the rocking curve half width in Laue (transmission) geometry [Pin78].

The rocking curve profile (3.3) can alternatively be expressed in reciprocal space via

$$I/I_0 = \left| \frac{q_z \tau}{2} \pm \sqrt{\left(\frac{q_z \tau}{2} \right)^2 - 1} \right|^2 \quad (3.7)$$

where the parameter τ is proportional to the *extinction depth* Λ_0 [Aut93]:

$$\pi\tau = \Lambda_0 = \frac{\lambda \sqrt{\gamma_0 |\gamma_h|}}{|C| \sqrt{\chi_h \chi_{\bar{h}}}}. \quad (3.8)$$

Formula (3.7) can be used to derive the rocking curve width along the q_z -direction in reciprocal space that corresponds to the angular Darwin width (3.6). When presenting the experimental results for the peak widths in the next Chapter, we will also give the numerical values of the Darwin width calculated for our special experimental conditions for comparison.

3.4 Conclusion

In summary, we have presented a new method to quantitatively investigate the crystalline quality of semiconductors with a spatial resolution of the order of $1 \mu\text{m}$. The method is based on a combination of X-ray diffractometry and topography, and yields fast and precise information on the local intensity of Bragg peaks, local lattice tilts and the local rocking curve half width. In this way the macroscopic crystal quality parameters can be correlated with the microscopic lattice defects. The method has been implemented with a dedicated equipment at the ID19 beamline of the ESRF. We developed a data analysis software package which reconstructs the raw data and corrects them for different experimental effects. It can be used to plot the results in terms of lattice curvature and rocking curve FWHM as two-dimensional images.

The advantages of the method in its present configuration include:

- The method is very fast (with an image rate of up to 1 image/sec), and gives precise and abundant information about sample curvature as well as the crystalline quality.
- It combines the advantages of diffractometry (high angular — i.e. reciprocal space — resolution) and X-ray topography (high spatial resolution for the detection of lattice defects). It allows to correlate the macroscopic effects of sample inhomogeneities (wafer curvature) with their microscopic causes (lattice defects).
- The experimental procedure is very flexible, and allows to adapt the experimental conditions to a variety of different sample materials and thicknesses. One can choose the X-ray wavelength from a broad available spectrum, including very hard X-rays. Since these have a lower absorption, we are able to work in transmission geometry even for thick samples. Furthermore, the use of hard X-rays leads to low intrinsic peak widths (Darwin widths). In this way, the measured rocking curves give a precise image of the real sample properties, and are not broadened significantly due to the nature of the scattering process.
- The choice between reflection and transmission geometry makes it possible to be selectively sensitive only to a small layer near the sample surface, or alternatively to the whole crystal. In this way, lattice distortions can for the first time be monitored for the entire volume of a crystalline structure, which was not possible with the pre-existing commercial instruments. Furthermore, the choice between two configurations for the monochromator and for the diffractometer geometry (vertical or horizontal scattering planes) can be used to optimize the dispersion conditions.

First results of the application of this method will be given in the next Chapter.

Chapter 4

Application to industrial quality inspection of semiconductor wafers

We now apply the method described in the previous Chapter to the study of lattice distortions in two different sample types: gallium arsenide and silicon carbide wafers. They serve as examples for two different groups of semiconductor materials which we might call the “classical” and the “new” ones. The first group is constituted by semiconductors like Si, GaAs and InP. The technology for their growth has been studied and optimized with considerable effort during the past 50 years. Important progress has been achieved, so that they are nowadays routinely used in device applications. The second group, in which we find materials like SiC and GaN, is technologically far less well controlled. Their special properties, like a higher electronic bandgap, mechanical hardness and chemical resistivity, make them attractive for innovative applications and will certainly cause further effort to be invested into this field of material research.

In this Chapter we show experimental results from both groups of materials, obtained with the procedure discussed in Chapter 3. At the end of the Chapter, we will furthermore discuss possible future extensions of our method.

4.1 Experimental example: GaAs wafers

Fig. 4.1 shows the results of three angular scans recorded on three different spots on the surface of a GaAs wafer grown by the *liquid encapsulated Czochralsky* (LEC) method [Jac98]. The rocking curve half widths (images in the left column) must be compared with the theoretical value of the Darwin width for the symmetric 220-reflection of GaAs at an X-ray energy of 30 keV (see eq. (3.6)):

$$w_{\text{GaAs}} = 0.00091^\circ = 3.2''$$

The experimental maps of the spatial distribution of the rocking curve FWHM exhibit a system of small “islands”, regions with a very low FWHM (close to the theoretical value) and accordingly a high local crystalline quality. They are separated by a network of lines with considerably larger local half width. These islands represent crystallites with a highly perfect internal crystalline structure, while the system of lines between them constitutes a network of dislocations. The possibility to map the rocking curve half width with a spatial resolution in the range of micrometers thus allows to visualize the mosaicity of the sample, to identify the individual crystallites as well as the transition regions between them, and to measure their individual crystalline quality separately.

The structure of the networks of dislocations changes from one spot on the sample to the next: While in the first row of Fig. 4.1 (center of the wafer) they seem to be more or less isotropic, they show a clear preferential orientation along the vertical direction in the second row, and along the horizontal direction in the third row of Fig. 4.1.

The maps of the angular position of the Bragg peak (right column of Fig. 4.1) indicate mainly how the sample curvature (lattice tilt) changes over macroscopic dimensions. However, at many places the local

details are sufficiently clear to allow a similar identification of crystallites as in the FWHM maps. From this observation, it becomes clear that not only the crystallites have a good internal crystalline quality, but also that their homogeneous orientation changes from one crystallite to the next, due to the defects in the zone between them.

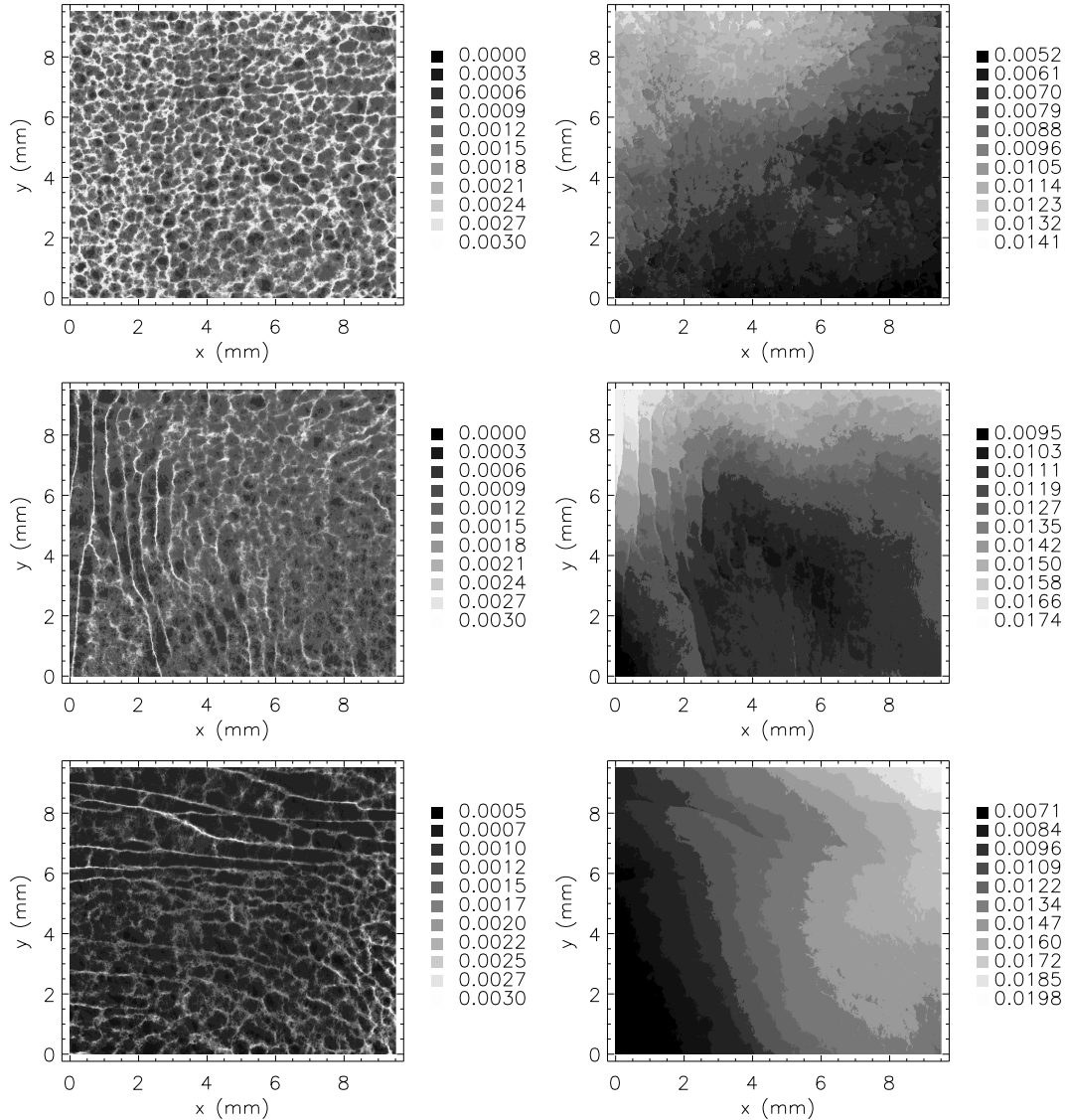


Figure 4.1: Rocking curve imaging of GaAs-LEC-wafers: results of the data evaluation procedure. Maps of rocking curve half width (left column) and of angular peak position (right column) for three different locations on the surface of the same sample. First row: center of the wafer, second and third row: two different regions along the wafer circumference. All gray scales are in units of degrees. In the curvature maps, the average peak shift of 0.01° across the image diagonal corresponds to a bending radius of about 80 m. [LBH00]

4.2 Another example: SiC wafers

Silicon carbide is an example of a “new” semiconductor material. Its fabrication technology is not yet optimized to the same degree as for silicon or gallium arsenide, but it is a very interesting material due to

its higher electronic bandgap, which makes it attractive for optoelectronic devices in the shorter wavelength range (“blue lasers”). Furthermore, its mechanical hardness, chemical resistivity and thermal stability are of high interest for a variety of applications.

Silicon carbide exists in different crystallographic phases or *polytypes*, the most well-known of which are called “3C” (cubic), “4H” and “6H” (both hexagonal) and “15R” (rhombohedral). Silicon carbide can be grown by two different methods: The *Lely method* [Lel55], on the one hand, yields very pure, relatively perfect single crystals, but the maximum size of samples which can be obtained is limited to some *cm* in diameter at best. The method is based on the evaporation of a polycrystalline SiC powder inside a furnace whose sidewalls are heated up to 2500 ° C. The material then condenses on the walls of a small porous cylinder introduced for this purpose into the furnace. The *modified Lely method* [TT78], on the other hand, leads to larger crystals. Here, the growth from vapour starts in a controlled way on an oriented SiC seed, rather than spontaneously on the walls of the porous cylinder. However, the crystalline quality of the resulting crystals is generally worse than in the seed, and new defects like micropipes can appear [HDV99, DHH99]. For a recent X-ray topographic study of SiC and its typical defects, including a more detailed review of growth methods and polytypes, see [Mil99].

In order to monitor the overall crystalline quality and simultaneously correlate it with the microscopic defects, we applied our experimental method to two different SiC samples, grown by the two growth methods. The results of the data evaluation procedure are shown in Fig. 4.2. The left column shows the rocking curve half width maps, while the right column contains the maps of the angular peak position. Once again, the FWHM values must be compared with the theoretical Darwin width for perfect crystals (eq. (3.6)), which for the symmetric 220-reflection of SiC at an X-ray energy of 30 keV yields

$$w_{\text{SiC}} = 0.00033^\circ = 1.2''$$

From the images of the sample grown by the Lely method (upper row in Fig. 4.2) it becomes clear that this crystal is indeed relatively perfect. The half widths are generally very low (although they remain higher than the theoretical value, of the order of 5×10^{-4} to 1×10^{-3} degrees) and have a relatively homogeneous distribution. Only a narrow area on the right exhibits a larger half width, and also shows some defects. This is in fact the region where the crystal growth began and the growth process had not stabilized entirely yet. However, the rocking curve width does not exceed 1.5×10^{-3} degrees anywhere, which indicates an overall highly regular crystal lattice. This picture is also confirmed by the curvature map (right column): The crystal orientation varies by no more than 0.02 degrees across the whole illuminated surface, and in a large area (excluding the region on the right) it is stable within 1×10^{-3} degrees. In summary, the crystal is almost ideal.

Two stripes in the images (about the last *mm* on the left and right borders) seem to be more perturbed. They do not indicate deviations from crystalline perfection, though. As discussed above, samples grown by the Lely method do not reach a big size. Our sample was therefore smaller than the illuminating X-ray beam and the field of view of the camera. This is why only scattering by the surrounding air can be observed in these lateral regions.

The second sample (lower row in Fig. 4.2) shows very different characteristics: The FWHM is strongly non-homogeneous, with some highly perturbed regions where the width is as large as about 0.006° - under similar experimental conditions as before. The curvature map on the right shows the same tendency: The lattice orientations vary strongly across the illuminated area, with tilts of up to 0.15° within a distance of some millimeters.

An interesting feature in both of these images is the diagonal “bay” in the upper left corner, which seems similar to the two empty stripes in the images of the first SiC sample. However, this does not mean that we have detected a hole in the sample; this region simply did not diffract in our experiment. The reason is that the sample condensed in several different crystallographic phases. The regions with a cubic structure are in Bragg position under our experimental conditions, while the hexagonal parts of the sample have a different lattice parameter and accordingly diffract at different Bragg angles. Therefore they appear black in our image. Our experiment thus shows that the sample consists of a mixture of crystallographic phases, which is a well-known problem in SiC growth in general.

Another detail deserves attention: the small tube-shaped region which is visible in both images at medium height, in the left third of the field of view. The FWHM map shows an inner region of relatively good

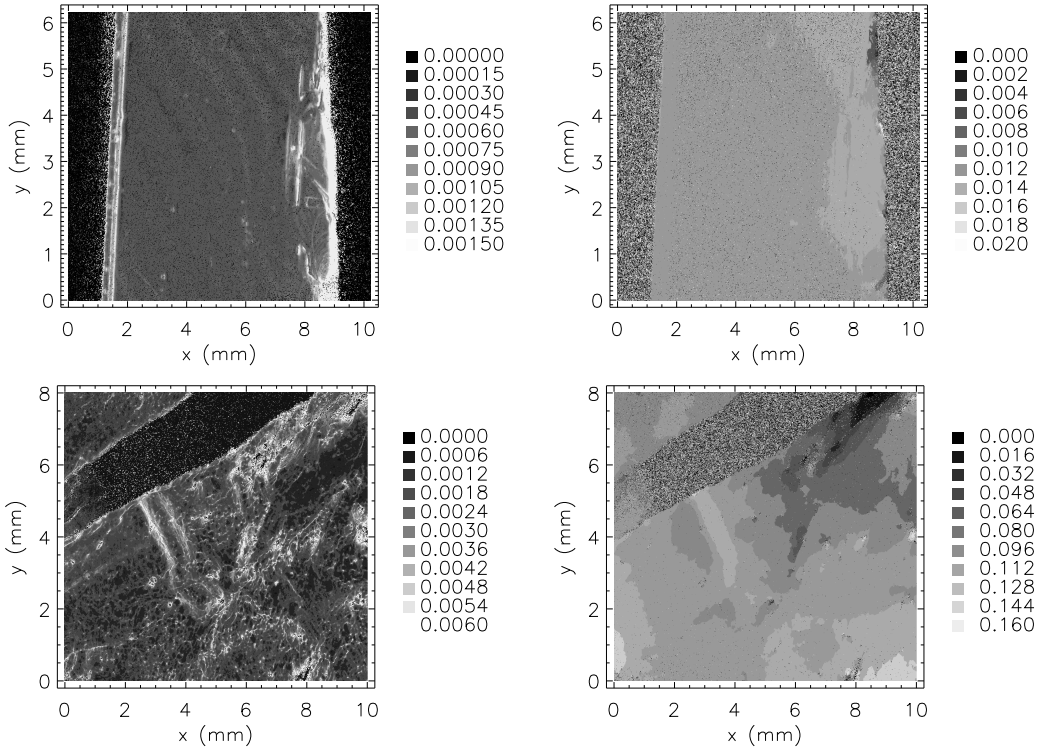


Figure 4.2: X-ray rocking curve imaging on silicon carbide wafers: results of the data evaluation procedure. Maps of the rocking curve half widths (left column) and of the angular peak position (right column) for a sample grown by the Lely method (upper row) and one grown by the modified Lely method (lower row). All gray scales are in units of degrees. In both kinds of maps, it is clearly visible that the crystalline quality of the first sample is superior to the one of the second sample. [LBH00]

crystalline quality, which is separated from its surroundings by two narrow, highly perturbed zones. The corresponding area in the curvature map shows that the interior of this “tube” is homogeneously oriented. At its borders, there occurs a sharp transition to regions with a different orientation, at the right and at the left. The combination of the two images thus allows to identify this tube-like region as a highly perfect crystallite, which is tilted with respect to its local crystallographic environment.

4.3 Perspective: Determination of complete strain fields via μm -resolved *triple* crystal diffractometry

Our procedure, as described so far, is applicable when the crystal lattice is essentially perturbed by lattice tilts, and not simultaneously by strong variations $\delta d/d$ of the lattice parameter. In this case the Bragg angle is nearly constant across the image, so that a one-to-one-correlation between spots on the sample surface and pixels of the camera is preserved.

When stronger variations $\delta d/d$ occur it becomes necessary to analyze the direction of the diffracted beam. Then, one can extract information on the local lattice parameter from the knowledge of the local total scattering angle $2\vartheta_B(x, z)$. This can be achieved not only in diffractometry [FKK97] and topography [BH81, YMW79], but also with a *triple* crystal version of our procedure, by inserting an analyzer crystal between the sample and the camera.

One then has to vary systematically not only the sample angle ω , but also the analyzer angle 2ϑ . This procedure obviously tends to increase the amount of data to be stored and treated by a large factor. This

disadvantage is more than balanced by the wealth of information which can be obtained in this way: By combining the measurements at several complementary reflections, one is principally able to extract all nine components of the *complete* lattice distortion tensor $\partial u_i / \partial x_j$ with a spatial resolution of some μm .

Crystal growers working on SiC have shown a strong interest in this application. Local strain variations influence the mechanisms of vapour deposition of atoms on a seed. Once the strain field can be measured, it can be used in numerical simulations with the aim to optimize the growth process. Due to this technological relevance, the triple-crystal version of the method will be experimentally realized in the near future.

4.4 Conclusion

In summary, we have given experimental examples of the μm -resolved investigation of crystalline quality in semiconductor wafers. Results for one classical and one “new” semiconductor material, namely GaAs and SiC, were reported. In the GaAs-LEC-wafers, networks of dislocations could be identified and distinguished from the neighbouring, highly perfect crystallites. In the case of SiC wafers, we could prove experimentally that the samples grown with the Lely method were far more homogeneous and defect-free than those grown by the modified Lely method. The latter were demonstrated to consist of a mixture of different crystallographic phases.

These were just two examples of what can be achieved with the method in its present state. Their choice was motivated by the fact that semiconductor wafers are the basis for the fabrication of microelectronic and optoelectronic devices. The extension and application of our method to microelectronic circuits or semiconductor lasers is straightforward. Furthermore, an extension of the method to a *triple crystal* measuring mode is planned for the near future.

However, in the context of the present work we will *not* pursue this technique any further, but continue a slightly different route. We will be interested in strain variations on even smaller length scales, namely in the 1-100 nm range. Strain variations on this scale occur in artificially patterned structures like surface gratings, quantum wires and quantum dots. A spatial resolution of the order of nanometers cannot (yet?) be reached in X-ray diffraction with the techniques described above in Chapter 3. Therefore, we will need to employ a different experimental strategy, making use of the fact that the strain field in such structures is *periodic* along the lateral direction. This allows us to study it with the help of *interference* effects. Investigation of this kind are the subject of the rest of this manuscript.

Part III

Lattice distortions on a scale below the micrometer: Strain investigations in semiconductor surface nanostructures

A short history of grating investigations

To define more clearly the relevance of the present work in the context of strain investigations in surface gratings, let us have a short look on previous studies and review the history of X-ray methods developed to characterize this type of structures.

The authors of early studies of laterally patterned GaAs substrates [TG90] and of bare and overgrown InP substrates [MS90] recognized the methodical potential of X-ray diffraction in this field. It was found that the lateral grating periodicity induced a series of satellite peaks in reciprocal space around the central Bragg peaks. Theoretical models based on kinematical diffraction theory were proposed [MS90, DCST94] which could describe the influence of the geometrical parameters and the grating shape onto the diffraction pattern. These studies were done with double-crystal diffractometry (DCD), a method whose limited resolution in reciprocal space does not allow to examine the details of the grating shape. Lattice strain was immediately recognized to influence the diffraction patterns [MS90], but could not be explicitly analyzed at this stage.

Later, triple-crystal diffractometry (TCD) was used to resolve more information in order to investigate the shape of simple surface gratings [GBM93, SUW93] and of superlattice gratings [TLRL92, HTK93, TSDC95]. Thorough experimental and theoretical studies by Tolan [Tol93] et al. showed that the observed intensity distribution in reciprocal space was accessible to a quantitative theoretical description by either kinematical diffraction theory (in the case of X-ray *diffraction*) [TKB92, TPB94] or dynamical theory (in the case of X-ray *reflectivity*) [TPB95].

After the influence of the grating geometry onto the diffraction pattern was understood, it became clear that this was not sufficient to interpret some of the experimentally observed diffraction patterns [Gai95]. In certain cases, drastic deviations of measured reciprocal space maps from theoretical expectations appeared, which could not even be explained by model calculations which additionally took dynamical scattering effects (multiple scattering, *Umweganregung*) into account [BG95, BHP94]. Several research groups found that the discrepancies could be due to strain relaxation in quantum wires [SKT96], quantum dots [DKB95] and surface gratings [LBT97]. Reciprocal space maps of $\text{Ga}_x\text{In}_{1-x}\text{As}$ gratings clearly indicated that a non-homogeneous strain distribution was present in the samples and significantly distorted the diffraction pattern with respect to the one of non-strained samples [Gai95]. Conversely, this strong distortion made it clear that X-ray diffraction is a very sensitive tool to study such strain fields.

However, an exact explanation and interpretation of the measured data was not easy. Initial models were based on simplifying assumptions: They neglected the influence of the interface with the substrate [DKB95], or they included a description of strain relaxation only in terms of a phenomenological power law *ansatz* [SUW96, SKT96, SK97]. More well-founded theoretical studies were made by De Caro et al., who first employed continuum elasticity theory to predict strain fields in quantum well and quantum wire structures. They showed how the combination of Hooke's law for a cubic material with the appropriate boundary conditions could be used to calculate the strain in planar strained layers [DCT93, DCT95a] and in quantum wires [DCT94, DCT95b] via the minimization of strain energy. The model was subsequently extended to superlattice gratings with a vertically periodic layer setup [DCTG96], for which an analytical solution of the strain problem in terms of a Fourier series was found. The limitation of these studies consists in neglecting the elastic interaction between the grating and the substrate and assuming a complete freedom of the grating region to relax laterally. The result for the strain is therefore not a strain *field* in the strict sense, since it cannot account for spatial inhomogeneities of the relaxation in strained-layer surface gratings.

Yet, the above-mentioned experiments indicated that the strain distribution was non-homogeneous in reality. Therefore, when this work was begun it was time to develop a complete quantitative model for the strain *field* in partially relaxed grating structures. The first strategy to begin with was to base the approach on continuum elasticity, although it had not been tested yet whether this macroscopic theory remained valid in the limit of structures with dimensions in the range of nanometers. It had been found to be “very well verified” for monoatomic films of ZnTe in CdTe in a study which compared the predictions of elasticity theory with *ab-initio* pseudopotential calculations [BEM97], but had been shown experimentally to be inapplicable in the limit of monoatomic films of InAs in InP in a high resolution TEM study [BPB92]. Therefore, the use of elasticity theory in this field could only be considered as tentative.

Attempts to solve the equations for the strain fields in gratings analytically remained inconclusive, mainly due to the complicated boundary conditions. Therefore, numerical techniques needed to be employed to obtain an approximated solution. Among other techniques, the *Finite Element Method* (FEM) is available in the form of commercial computer codes. Some problems remained to be solved in order to adapt these programs to the calculation of *lattice* strains in crystals, for which they were not originally conceived [PB99] (see Chapter 5). In the end, numerical solutions could be obtained, but the theoretical validity of the approximations underlying the use of linear elasticity theory as well as the numerical accuracy of the solutions remained to be tested.

Comparisons of FEM calculations for lattice strain fields with experimental data had previously been done by other research groups. The experimental techniques which were applied included electron diffraction [CAS94], photoluminescence [TMY92, NHW95] and micro-Raman measurements [JHA95]. In all these cases, not more than a qualitative similarity between experiment and calculation could be achieved. A detailed and *quantitative* experimental verification of the applicability of elasticity theory to nanostructures was still due.

Therefore, the following Chapters describe a technique to determine experimentally the complete spatial variation of strain fields in nanoscopic structures. By comparison of high-resolution X-ray diffraction data with calculated strain fields, the validity of elasticity theory as a theoretical description could be tested quantitatively, and the limits of its applicability were determined.

Chapter 5

Theory of diffraction from (strained) gratings

5.1 Grating geometry and reciprocal space structure

Kinematical theory predicts that an infinitely extended, perfect crystal diffracts only at discrete points in reciprocal space, the Bragg peaks. An actual crystal is not infinitely extended; the interruption (truncation) of the periodicity of the crystal lattice at the sample surface leads to the appearance of a continuous distribution of diffracted intensity around each Bragg peak. Mathematically, this can be described with the concept of a *shape function*: The susceptibility $\chi(\mathbf{r})$ of a finite crystal is written as the product of an “ideal” susceptibility $\chi_\infty(\mathbf{r})$ of an infinite crystal and the shape function $\Omega(\mathbf{r})$ which can have only two different values, namely 1 inside the crystal and 0 outside:

$$\chi(\mathbf{r}) = \chi_\infty(\mathbf{r}) \Omega(\mathbf{r}) \quad (5.1)$$

The structure amplitude of the sample can then be derived via the *convolution theorem* [Gui94]. It states that the Fourier transform $S(\mathbf{Q})$ of this product of two functions in real space is equal to the convolution of the two individual Fourier transforms in reciprocal space:

$$S(\mathbf{Q}) = \int \chi(\mathbf{r}) e^{-i\mathbf{Q}\cdot\mathbf{r}} d^3\mathbf{r} = \int \chi_\infty^{\text{FT}}(\mathbf{Q}') \Omega^{\text{FT}}(\mathbf{Q} - \mathbf{Q}') d\mathbf{Q}' \quad (5.2)$$

Let us assume for a moment that the crystalline material inside the boundaries described by $\Omega(\mathbf{r})$ is perfectly periodic, defect-free and non-strained. Then, the Fourier transform $\chi_\infty^{\text{FT}}(\mathbf{Q}')$ can be written as a discrete Fourier sum:

$$\chi_\infty^{\text{FT}}(\mathbf{Q}') = \int \chi_\infty(\mathbf{r}) e^{-i\mathbf{Q}'\cdot\mathbf{r}} d^3\mathbf{r} = \sum_{\mathbf{h}} \chi_{\mathbf{h}} \delta(\mathbf{Q}' - \mathbf{h}). \quad (5.3)$$

In writing (5.3) we have momentarily assumed that the grating consists of one single material only. This assumption is not too restrictive since Section 5.4 will introduce a formula for the general case of layered gratings.

The expression for the structure amplitude is reduced to a simple sum:

$$S(\mathbf{Q}) = \sum_{\mathbf{h}} \chi_{\mathbf{h}} \Omega^{\text{FT}}(\mathbf{Q} - \mathbf{h}) \quad (5.4)$$

If the shape described by Ω is extended over more than a few lattice parameters (contains a large number of atoms), then $\Omega^{\text{FT}}(\mathbf{Q})$ is relatively sharply defined in reciprocal space, and the intensity at $\mathbf{Q} = \mathbf{h}$ is not influenced by contributions from other reciprocal lattice points \mathbf{g} with $\mathbf{g} \neq \mathbf{h}$. In this case, expression (5.4) in the vicinity \mathbf{h} reduces to one single term:

$$S_{\mathbf{h}}(\mathbf{q}) = \chi_{\mathbf{h}} \Omega^{\text{FT}}(\mathbf{q}), \quad (5.5)$$

where the *reduced scattering vector* \mathbf{q} is defined as $\mathbf{q} = \mathbf{Q} - \mathbf{h}$. In other words, the intensity distribution in reciprocal space is given by the Fourier transform Ω^{FT} of the shape function, replicated around each Bragg peak of the crystalline material. For instance, in the case of a crystal plate with upper and lower (smooth) surfaces at $z = 0$ and $z = h$ each Bragg peak is surrounded by an intensity distribution along a vertical line with a profile $I(q_z) \sim (\sin(q_z h/2)/q_z)^2$, the so-called *crystal truncation rod* (CTR) [Rob86]. A similar CTR with a profile $I(q_z) \sim 1/(q_z^2 + \mu^2)$ can be derived for scattering from the surface of a semi-infinite crystal if absorption is taken into account by an absorption coefficient μ .

In this thesis, we deal with grating samples whose general geometry is shown in Fig. 5.1. Their shape function $\Omega(\mathbf{r})$ is characterized by a lateral periodicity (grating period D): The basic element, the single grating wire, is replicated along the x -direction at positions $x = nD$ for every integer number n . Mathematically, such a periodic shape can be described as a convolution of a “microscopic” shape function $\Omega_{\text{ind}}(\mathbf{r})$, describing the shape of one single individual grating wire, with an infinite series of delta-peaks along the x -direction:

$$\Omega(\mathbf{r}) = (\Omega_{\text{ind}}(\mathbf{r})) \otimes \left(\sum_{n \in \mathbb{N}} \delta(x - nD) \right). \quad (5.6)$$

In order to calculate the diffracted intensity from such a structure via (5.5) we need to obtain an expression for the Fourier transform of the shape function (5.6). This can be achieved by applying the convolution theorem once again, now in opposite direction, which yields (apart from a normalization factor):

$$\Omega^{\text{FT}}(\mathbf{q}) = \Omega_{\text{ind}}^{\text{FT}}(\mathbf{q}) \cdot \left(\frac{1}{D} \sum_{n \in \mathbb{N}} \delta(q_x - H_n) \right) \quad \text{with} \quad H_n = n \frac{2\pi}{D}, \quad (5.7)$$

where we made use of the fact that the Fourier transform of an infinite series of δ -functions in real space is given by a corresponding sequence of δ -peaks in reciprocal space (see e.g. Appendix A of [Gui94]). Equation (5.7) shows that the diffracted intensity does not represent a continuous distribution in reciprocal space, but is concentrated at specific lateral positions along the so-called *grating truncation rods* (GTRs) [GBM93] which are parallel to the CTR. In the case of gratings and quantum wires (as opposed to quantum dots) the in-plane positions of the GTRs can be written in vectorial notation as

$$\mathbf{Q}_{||} = \mathbf{h}_{||} + H_n \mathbf{e}_x. \quad (5.8)$$

Let us mention here that the organization of the diffraction pattern in GTRs is determined by the lateral superperiodicity of the structure only, and is independent of whether the material inside the grating period is strained or not. The sharpness of the GTR cross section along q_x can be altered only by fluctuations of the grating period D along the sample surface — apart from the fact that in experimental reciprocal space maps they are, of course, broadened due to the instrumental resolution of the instrument.

In order to obtain information about the structure inside one single grating period, one therefore needs to study the intensity profile $I(q_z)$ along the single GTRs. In the case of a grating of homogeneous, non-strained material the profile $I_n(q_z)$ of the n -th lateral rod can be calculated via the Fourier transform $\Omega^{\text{FT}}(\mathbf{q})$ of the shape function of one single period¹, evaluated selectively at the position $q_x = n \cdot 2\pi/D$.

In order to obtain the full reciprocal space structure of a grating, the remaining task is thus to calculate the Fourier transform of the shape function of a single grating wire. Due to the translational symmetry along the y -direction, the dependency of Ω^{FT} on q_y is given by a simple factor $\delta(q_y)$, so that the calculation effectively becomes a two-dimensional problem, $\Omega^{\text{FT}} = \Omega^{\text{FT}}(q_x, q_z)$. In what follows we perform this calculation explicitly with the example of a trapezoidal grating shape, as shown in Fig. 5.1. We use the following symbols to describe the geometry: t is the grating height, b the width of the planar top surface, g the width of the valley between neighbouring grating wires, and $p_{l/r} = \partial x/\partial z$ are the sidewall slopes. For the grating geometry shown in Fig. 5.1 the value of p_l is positive, whereas p_r is negative.

¹Our approach deviates slightly from the method which was used in [Tol93] to deduce the same result for the first time. There, a “grating function” $z = f(x, y)$ was used to describe the shape of the grating surface. The diffracted intensity is then given by the two-dimensional Fourier transform of the exponential $e^{i f(x, y)}$. In our notation, where the shape function Ω is a function of all three coordinates, no exponential is required, and the intensity is directly given by the three-dimensional Fourier transform of $\Omega(\mathbf{r})$ itself.

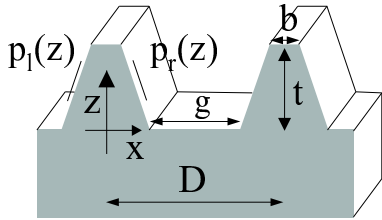


Figure 5.1: Geometry of a surface grating [BL99], including the definitions of some variables which will be used throughout this work: grating period D , groove path (grating valley width) g , top path (grating top width) b , and grating sidewall slopes $p_l, p_r = \partial x / \partial z$.

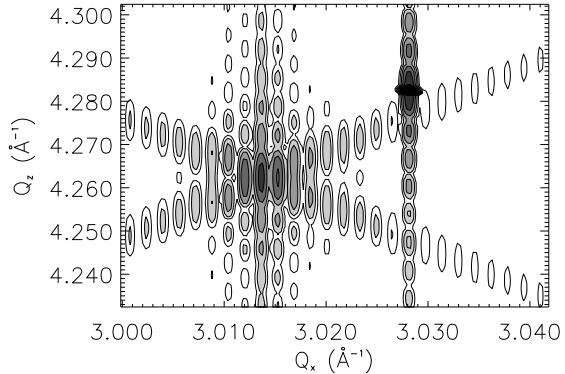


Figure 5.2: Reciprocal space structure (simulated diffraction pattern around the 224-reflection) of the grating shown on the left. The main feature is a characteristic cross pattern around the Bragg peak of the layer material ($\text{Ga}_x\text{In}_{1-x}\text{As}$) at $Q_x = 3.013 \text{ \AA}^{-1}$ (left). This figure highlights the pure influence of the grating shape function on the diffraction pattern. For better comparison with the corresponding experimental maps from strained samples the effect of an InP substrate is included. It gives rise to the strong Bragg peak at $Q_x = 3.028$ (on the right), surrounded by its CTR. Grating and substrate are assumed not to be in contact, so that no strain occurs in either material.

In terms of these variables, the Fourier transform of $\Omega_{\text{ind}}(x, z)$ is

$$\Omega_{\text{ind}}^{\text{FT}}(q_x, q_z) = \int_0^t \int_{a_l(z)}^{a_r(z)} e^{-iq_z z} e^{-iq_x x} dx dz \quad (5.9)$$

The integration limits $a_l(z)$ and $a_r(z)$ represent the left and right border of the trapeze at height z . They are related to the sidewall slopes $p_{l/r}(z)$ at height z by

$$a_l(z) = -\frac{b}{2} + \int_t^z p_l(z') dz' \quad a_r(z) = \frac{b}{2} + \int_t^z p_r(z') dz' \quad (5.10)$$

These formulae can be used to describe arbitrarily curved sidewall slopes, e.g. in the case of selectively etched multilayer gratings [BLG00]. For our present case of a simple trapezoidal grating with straight sidewalls they simplify to

$$a_l(z) = -\frac{b}{2} + (z - t)p_l \quad a_r(z) = \frac{b}{2} + (z - t)p_r. \quad (5.11)$$

For $q_x \neq 0$ the first integration yields

$$\Omega_{\text{ind}}^{\text{FT}}(q_x, q_z) = \frac{i}{q_x} \int_0^t \left\{ e^{-iq_x(\frac{b}{2} - p_r t)} e^{-i(q_z + p_r q_x)z} + e^{iq_x(\frac{b}{2} + p_l t)} e^{-i(q_z + p_l q_x)z} \right\} dz \quad (5.12)$$

We simplify the notation by defining the new scattering vectors

$$q^+ = q_z + q_x p_r \quad (5.13)$$

$$q^- = q_z + q_x p_l \quad (5.14)$$

Using (5.13) and (5.14), the formula for scattering amplitude at $q_x \neq 0$ becomes:

$$\Omega_{\text{ind}}^{\text{FT}}(q_x, q_z) = \frac{i}{q_x} \left\{ e^{-iq_x(\frac{b-p_r t}{2})} \frac{\sin(q^+ t/2)}{q^+ t/2} - e^{iq_x(\frac{b+p_l t}{2})} \frac{\sin(q^- t/2)}{q^- t/2} \right\} e^{-iq_z \frac{t}{2}} \quad (5.15)$$

The two essential terms in this formula, the $\sin(q \dots)/q \dots$ -functions, reach their maximum value of 1 when the respective argument is zero. The effect on the intensity distribution in reciprocal space is illustrated in Fig. 5.2. Around the Bragg peak of the grating material we see two diagonal streaks of strong intensity along straight lines with $q_z = -p_{l/r} q_x$, i.e. one streak perpendicular to each of the grating sidewalls. Qualitatively, this can be understood by analogy with the appearance of a CTR in the case of a flat surface. The grating sidewalls give rise in a similar way to “sidewall truncation rods” which run diagonally in reciprocal space.

The top surface of the grating gives rise to a third streak along the q_z direction, as becomes apparent by deriving the limiting expression of (5.15) for $q_x = 0$:

$$\Omega_{\text{ind}}^{\text{FT}}(0, q_z) = \int_0^t e^{-iq_z z} \{b + (p_r - p_l)(z - t)\} dz \quad (5.16)$$

$$= \left\{ b - i \frac{(p_r - p_l)}{q_z} \right\} t \frac{\sin(q_z t/2)}{q_z t/2} e^{-iq_z t/2} + i \frac{(p_r - p_l)}{q_z} t \quad (5.17)$$

For direct use in a computer program, let us also state explicitly the limit of (5.17) for $q_z = 0$:

$$\Omega_{\text{ind}}^{\text{FT}}(0, 0) = \left(b + \frac{(p_l - p_r)}{2} t \right) t. \quad (5.18)$$

This expression corresponds in fact to the area of a trapeze with height t and top width b .

The combination of equations (5.15), (5.17) and (5.18) describes completely the kinematical diffraction amplitude from a trapezoidal grating of homogeneous material. The resulting intensity distribution in reciprocal space has a characteristic cross form, as visible around the layer Bragg peak in Fig. 5.2. We have chosen a trapezoidal shape for the explicit calculation due to its relative generality: The formulae for many other grating shapes can be deduced from this result as special cases, for instance a triangular ($b = 0$), rectangular ($p_l = p_r = 0$) or parallelogram shape ($p_l \neq p_r$).

In deriving (5.17) and (5.18) we have neglected the contribution of the planar substrate below the grating. When necessary, it can be taken into account additionally without major complications [Tol93]. The reason for neglecting it here is that we are not mainly interested in homogeneous gratings, but in gratings which are internally *strained* due to the contact between two or more mismatched materials. X-ray diffraction from such structures cannot be treated by simple Fourier transformation of the external shape function any more. However, in the approach which we will develop in Section 5.4 for the calculation of diffracted intensity from strained structures equations (5.15), (5.17) and (5.18) will reappear as one ingredient of fundamental importance. Before turning to this subject, we first have to introduce a theoretical description of the strain fields occurring in epitaxial structures.

5.2 Strained gratings and elasticity theory

In Section 5.1 we have reviewed the relations between structural properties and the X-ray diffraction signal for the case of “monolithic” gratings. This field has been under intensive investigation in the last decade [MS90, TG90, Tol93, BG95] and is well understood by now. However, for device applications in electronics and optoelectronics, layered heteroepitaxial structures consisting of several different materials are more relevant. They allow to achieve quantum effects by confinement of charge carriers to nanoscopic dimensions along one, two or three directions, due to the different electronic band gaps of the materials involved.

The different types of semiconductors involved in such layered structures generally do not only differ in band gap, but also in lattice parameters. Under epitaxial conditions thin mismatched layers tend to grow *pseudomorphically*, i.e. the layer material adapts its lateral lattice parameter to the lattice spacing

of the substrate. This is true as long as the layer thickness does not exceed a certain *critical thickness* [MB74]. Thus, the contact at the interface leads to a deformation of the crystal lattice of the layer material. To describe this deformation quantitatively we introduce the displacement field $\mathbf{u}(\mathbf{r})$. For a piece of material initially located at \mathbf{r} , the vector $\mathbf{u}(\mathbf{r})$ indicates the change in position between the bulk state of the respective material and the configuration in the actual structure:

$$\mathbf{r}' = \mathbf{r} + \mathbf{u}(\mathbf{r}) \quad (5.19)$$

The question of interest in this section is how the variation of the displacement field $\mathbf{u}(\mathbf{r})$ across the whole structure depends on the material compositions and the geometrical parameters of the structure.

A preliminary answer to this question can be found in the framework of *linear elasticity theory* [LL86, TG87, CP92], at least in the limit of small relative displacements $u_{i,j} = \frac{\partial u_i}{\partial x_j} \ll 1$. In this Section, we introduce the relevant quantities dealt with in this theory, derive a partial differential equation (PDE) from which $\mathbf{u}(\mathbf{r})$ can be determined, and present solutions for two special cases. In the next Section (5.3) we will discuss a method by which a general solution of the PDE can be found *numerically*.

Before proceeding to the technical details, it must be emphasized that elasticity theory is a *continuum* theory developed for macroscopic objects, and does not take the atomic nature of matter into account. Therefore, the description of *lattice* distortions in nanoscopic gratings by means of elasticity theory stays on a somewhat hypothetical ground for the moment. It is not clear *a priori* whether the interaction between atomic monolayers at the interfaces of an epitaxial structure can be described in terms of a continuous distribution of forces, on which the idea of a strain tensor σ_{ij} is based. This is why the entire approach presented in this and the following sections should be considered as a tentative description, the general validity of which remains to be verified.

We define the *strain tensor* $\epsilon_{ij}(\mathbf{r})$ and the *rotation tensor* $\omega_{ij}(\mathbf{r})$ as the symmetric and antisymmetric parts of the derivative tensor $\mathbf{u}_{i,j}$, respectively:

$$\epsilon_{ij} = \frac{1}{2} \left\{ \frac{\partial u_i}{\partial x_j} + \frac{\partial u_j}{\partial x_i} \right\} \quad (5.20)$$

$$\omega_{ij} = \frac{1}{2} \left\{ \frac{\partial u_i}{\partial x_j} - \frac{\partial u_j}{\partial x_i} \right\} \quad (5.21)$$

with $i, j \in [1, 2, 3]$. By definition $\epsilon_{ij} = \epsilon_{ji}$, so that the strain tensor has six independent components. The three diagonal components ($i = j$) represent compressions or dilatations along the axis e_i .

The rotation tensor ω_{ij} contains three independent components (ω_{32}, ω_{13} and ω_{21}), which can be rearranged to form a vector $\boldsymbol{\omega}$. This vector can equivalently be expressed with the *curl* operator:

$$\boldsymbol{\omega} = \begin{pmatrix} \omega_1 \\ \omega_2 \\ \omega_3 \end{pmatrix} = \begin{pmatrix} \omega_{32} \\ \omega_{13} \\ \omega_{21} \end{pmatrix} = \frac{1}{2} \nabla \times \mathbf{u}(\mathbf{r}) \quad (5.22)$$

The quantities $\mathbf{u}(\mathbf{r})$ and $\epsilon_{ij}(\mathbf{r})$ characterize the geometrical effects due to distortion inside a material. On the other side, the forces generated by the distortion are described by the *stress tensor* $\sigma_{ij}(\mathbf{r})$, which can be defined so as to be symmetrical ($\sigma_{ij} = \sigma_{ji}$) in analogy to the strain tensor [LL86]. The divergence of the stress tensor, $\partial \sigma_{ij} / \partial x_j (\mathbf{r})$, gives the net force component along e_i acting on a unit volume at the location \mathbf{r} . The elements of the tensor σ_{ij} represent the force component along the i -axis acting on a unit surface that is perpendicular to the j -axis.

A distorted body in static equilibrium is described by the equation

$$\frac{\partial \sigma_{ij}}{\partial x_j} + \mathbf{f}_i = 0, \quad (5.23)$$

where \mathbf{f} represents the body forces per unit volume acting on the material (due for instance to a gravitational field).

X-ray structure investigation allows to proof directly the geometrical displacements $\mathbf{u}(\mathbf{r})$. We are therefore interested in a differential equation equivalent to (5.23), but expressed in terms of $\mathbf{u}(\mathbf{r})$. In order to derive such an equation, we relate stress to strain by *Hooke's law*:

$$\sigma_{ij} = C_{ijkl} \epsilon_{kl} \quad (5.24)$$

where the *stiffness* C_{ijkl} is a fourth-order tensor with $3^4 = 81$ elements [Nye95, for transformation properties see also Appendix A]. After some calculus, the following PDE for the displacement results [LL86] (with the *Lamé constants* λ, μ):

$$-\mu \Delta \mathbf{u}(\mathbf{r}) - (\lambda + \mu) \operatorname{grad} \operatorname{div} \mathbf{u}(\mathbf{r}) = \mathbf{f}(\mathbf{r}). \quad (5.25)$$

The main difficulty in solving (5.25) for $\mathbf{u}(\mathbf{r})$ lies in the often very complicated boundary conditions, which reflect the shape of the sample surface. Two kinds of boundary conditions can be used: Either the displacement $\mathbf{u}(\mathbf{r})$, and thereby also the strain $\epsilon_{ij}(\mathbf{r})$, along the sample boundary is given, or the value of the force density \mathbf{T} acting on the sample surface is specified. The latter method is equivalent to prescribing the values of the stress tensor σ_{ij} , since \mathbf{T} results from σ_{ij} via $T_i = \sigma_{ij} n_j$, where \mathbf{n} is the local surface normal.

In the case of surface gratings a combination of both methods is most appropriate. At the interface with the vacuum the grating is free to relax so that along the upper surface, the grating sidewalls and the grooves the following boundary conditions holds:

$$\sigma_{ij} \mathbf{n}_j = 0 \quad (5.26)$$

Another boundary condition results from the lateral grating periodicity:

$$\mathbf{u}(\mathbf{r}) = \mathbf{u}(\mathbf{r} + D\mathbf{e}_x). \quad (5.27)$$

This condition can be combined with the equation $\mathbf{u}(\mathbf{r}) = -\mathbf{u}(-\mathbf{r})$, which is valid in the case of symmetrically shaped gratings² and yields a condition for the left and right sample boundary:

$$\mathbf{u}_x = 0 \quad \text{for} \quad x = \pm \frac{D}{2} \quad (5.28)$$

Finally, the substrate thickness t_{sub} is assumed to be large enough (of the order of some μm at least) so that its lower boundary is completely unaffected by the grating-induced strain field:

$$\mathbf{u} = 0 \quad \text{for} \quad z = -t_{sub} \quad (5.29)$$

The combination of (5.26), (5.28) and (5.29) specifies completely the outer, *geometrical* restrictions on the solution $\mathbf{u}(\mathbf{r})$. Up to this point, the lattice mismatch between the different materials has not yet been taken into account. The conditions for the contact between the different materials at the interfaces inside the structure are crucial, since without these no strain field would be generated at all. Therefore, the following equation for the contact between materials A and B (lattice constants a^A, a^B) at all horizontal interfaces can be considered as the most important among all the boundary/interface conditions [PB99]:

$$\mathbf{u}^B \left(\frac{a^B}{a^A} x_0 \right) - \mathbf{u}^A(x_0) = \frac{a^B - a^A}{a^A} x_0 \mathbf{e}_x. \quad (5.30)$$

Equation (5.30) states that the difference in displacement between two adjacent materials grows linearly as a function of lateral distance, with a proportionality constant corresponding to the lattice mismatch. This expresses the condition of pseudomorphic growth: The one-to-one relation between corresponding atoms in the two adjacent layers translates into a very specific discontinuity of lateral strain ϵ_{xx} across the interface, since the displacement fields are calculated with respect to each layer's bulk state. The vertical

²All the samples investigated in this thesis fulfil the symmetry requirement. For asymmetrical grating shapes (5.28) can no longer be used, and to calculate $\mathbf{u}(\mathbf{r})$ it becomes necessary to specify the boundary conditions in a different way [LBG99].

displacement component \mathbf{u}_z , on the other hand, as well as the vertical stress are continuous across all horizontal interfaces³.

Equation (5.30) is of fundamental importance for all our strain calculations in the sense that it allows to establish the link between macroscopic continuum elasticity theory and the microscopic boundary conditions, which result from the discrete, atomic nature of matter.

This equation can be restated by introducing the distinction between the initial displacement \mathbf{u}^0 occurring in the planar layer before etching (and corresponding to a spatially uniform initial strain ϵ^0), and the grating-induced strain relaxation $\Delta\mathbf{u}$ which is caused by the etching process:

$$\mathbf{u}(\mathbf{r}) = \mathbf{u}^0(\mathbf{r}) + \Delta\mathbf{u}(\mathbf{r}). \quad (5.31)$$

In pseudomorphically grown structures the discontinuity of $\mathbf{u}(\mathbf{r})$ is fully contained in $\Delta\mathbf{u}(\mathbf{r})$. Condition (5.30) is then equivalent to the fact that the relaxation $\Delta\mathbf{u}(\mathbf{r})$ is continuous across the interface.

An analytical solution to the combination of (5.25) and (5.26)-(5.30), expressed in terms of a Fourier series, has been found by De Caro et al. [DCTG96] for the special case of rectangular superlattice gratings. In their derivation the authors made the simplifying assumption that the influence of the substrate-grating interface on the strain field in the grating can be neglected. Whenever this approximation is not appropriate it remains a difficult task to find a solution $\mathbf{u}(\mathbf{r})$ which satisfies simultaneously (5.25) and the boundary conditions. We will therefore make use of numerical methods to calculate an *approximate* solution for the strain field. The details of these methods are the subject of the next section.

Before proceeding to the general solution, we present analytical solutions for the two limiting cases of *full distortion* and *full strain relaxation*. The first case, the fully strained state described by \mathbf{u}^0 in (5.31), is characterized by tetragonal deformation in the layer: The layer lattice (bulk lattice parameter a^l) is matched to the substrate (lattice parameter a^s) along both the x - and the y -direction. The strain in the layer is determined by the relative lattice mismatch:

$$\epsilon_{||}^0 = \epsilon_{xx}^0 = \epsilon_{yy}^0 = \frac{a_s - a_l}{a_l} \quad (5.32)$$

Along the third direction the material is free to relax ($\sigma_{zz} = 0$), and the resulting vertical strain ϵ_{zz} can be deduced from Hooke's law (5.24):

$$\epsilon_{zz}^0 = - \left(\frac{C_{31} + C_{32}}{C_{33}} \right) \cdot \epsilon_{||}^0. \quad (5.33)$$

C_{ij} are the elements of the *stiffness tensor* in 6×6 -matrix notation [CP92] (see Appendix A). Relation (5.33) can be simplified to

$$\epsilon_{zz}^0 = -2 \left(\frac{C_{12}}{C_{11}} \right) \cdot \epsilon_{||}^0 \quad (5.34)$$

on two conditions: The crystalline material must have cubic symmetry, and the axes of the coordinate system used must coincide with the cubic crystallographic axes. In this case C_{ij} has three independent components only (conventionally named C_{11} , C_{12} and C_{44}) whose values can be found in the literature for many semiconductor materials [Ada82, Ada85]. In any other case, for instance if one chooses the x - and y -axes perpendicular and parallel, respectively, to the wires of a [110]-oriented grating, C_{ij} must first be transformed from the crystallographic to the rotated reference system (see Appendix A), and then the more general relation (5.33) needs to be used.

The second limiting case (full strain relaxation) is characterized by orthorhombic deformation of the strained layer. It represents the fully relaxed state of a grating which is lattice matched to the substrate along one direction only, the direction of the wires (with ϵ_{yy} still being given by (5.32)), but free to relax

³For non-horizontal interfaces, such as the sidewalls of the buried grating studied in Chapter 6, with an inclined normal $\mathbf{n} \parallel \mathbf{e}_z$, (5.30) needs to be replaced by a similar equation for the component of \mathbf{u} along the interface, $\mathbf{u}_{||} = \mathbf{n} \times (\mathbf{n} \times \mathbf{u})$.

in the both x - and the z -direction. The resulting lateral and vertical strain ϵ_{xx} and ϵ_{zz} can be found from $\sigma_{xx} = \sigma_{zz} = 0$, together with Hooke's law (5.24):

$$\epsilon_{xx}^{\text{ortho}} = - \left(\frac{C_{33}C_{12} - C_{13}C_{32}}{C_{33}C_{11} - C_{13}C_{31}} \right) \cdot \epsilon_{\parallel}^0 \quad (5.35)$$

$$\epsilon_{zz}^{\text{ortho}} = - \left(\frac{C_{11}C_{32} - C_{31}C_{12}}{C_{33}C_{11} - C_{13}C_{31}} \right) \cdot \epsilon_{\parallel}^0 \quad (5.36)$$

For cubic symmetry all three directions are equivalent, so that (5.35) and (5.36) become identical:

$$\epsilon_{xx}^{\text{ortho}} = \epsilon_{zz}^{\text{ortho}} = - \left(\frac{C_{11}C_{12} - C_{12}^2}{C_{11}^2 - C_{12}^2} \right) \cdot \epsilon_{\parallel}^0 \quad (5.37)$$

However, for different wire orientations the anisotropy of the crystalline material causes a relevant difference between $\epsilon_{xx}^{\text{ortho}}$ and $\epsilon_{zz}^{\text{ortho}}$. For instance, in the case of an InP-grating with [110]-oriented wires the value of the coefficient in parenthesis in (5.35) is 0.015, while in (5.36) it is 0.554.

An orthorhombic strain state is realized in the limit of single-layer gratings with large height (see Fig. 5.3) where the influence of the substrate on ϵ_{xx} can be assumed to decay to zero inside a narrow transition region near the substrate-grating interface [DKB95, DCT94, DCT95b].

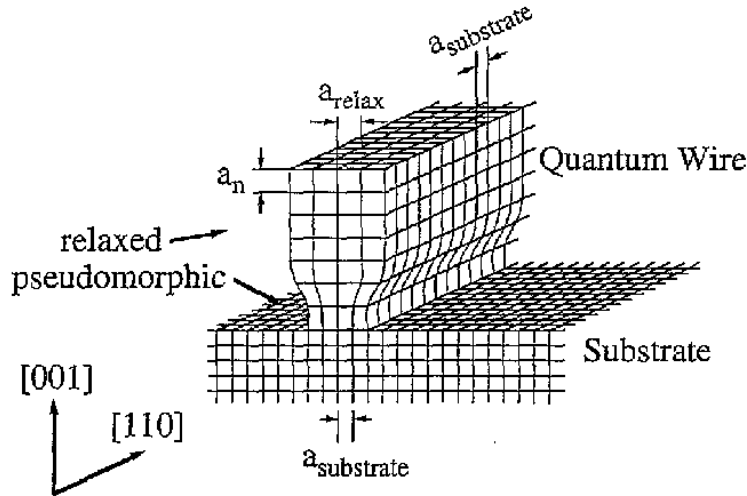


Figure 5.3: Model for strain relaxation in a grating with large height. The layer material is lattice matched to the substrate along the wire direction, and completely relaxed along the two perpendicular directions, except in a narrow transition region near the grating-substrate interface. [DKB95]

The actual strain state $\epsilon_{ij}(r)$ in a partially relaxed grating will be intermediate between the fully strained state ϵ^0 and the fully relaxed state ϵ^{ortho} , and still remains to be determined. Nevertheless, the knowledge of the values of both ϵ^0 and ϵ^{ortho} is highly useful. They represent upper and lower limits to the actual strain in partially relaxed gratings and can be used for an independent check of a calculated strain.

5.3 Numerical calculation of strain fields. The Finite Element Method

A variety of approximate methods to solve boundary value problems such as (5.25) have been developed in the past [PTV95]. One group of numerical techniques is inspired by variational calculus, and is based on the fact that (5.25) can be reformulated as a minimization problem. Among all possible strain configurations which satisfy the boundary conditions, the strain field actually occurring in the sample is the one which

minimizes a *strain energy functional*. The expression for the potential energy $\Pi(\mathbf{u}(\mathbf{r}))$ of a configuration $\mathbf{u}(\mathbf{r})$ is [CP92]

$$\Pi(\mathbf{u}) = \frac{1}{2} \int_V \sigma_{ij}(\mathbf{u}) \epsilon_{ij}(\mathbf{u}) dV - \left\{ \int_V \mathbf{f} \cdot \mathbf{u} dV + \int_S \mathbf{T} \cdot \mathbf{u} dS \right\}, \quad (5.38)$$

where we wrote $\epsilon_{ij}(\mathbf{u})$ and $\sigma_{ij}(\mathbf{u})$ to indicate that strain and stress depends uniquely on displacement via (5.20) and (5.24). The first integral in (5.38) is proportional to the *internal* strain energy of the body, while the terms in parentheses correspond to the work done by *external* body forces \mathbf{f} and surface forces \mathbf{T} . In our case, the only possible body force is the (weak) gravitational field; we will therefore neglect \mathbf{f} from now on. A condition for minimization of (5.38) is provided by the *principle of virtual work*. It states that for a displacement field $\mathbf{u}(\mathbf{r})$ which minimizes (5.38) the work done by any additional *virtual displacement* $\delta\mathbf{u}(\mathbf{r})$ must be zero [CP92]:

$$\delta\Pi = \int_V \sigma_{ij}(\mathbf{u}) \delta\epsilon_{ij}(\delta\mathbf{u}) dV - \int_S \mathbf{T} \cdot \delta\mathbf{u} dS = 0 \quad (5.39)$$

or, with the help of Hooke's law:

$$\int_V C_{ijkl} \epsilon_{kl}(\mathbf{u}) \delta\epsilon_{ij}(\delta\mathbf{u}) dV = \int_S \mathbf{T} \cdot \delta\mathbf{u} dS. \quad (5.40)$$

Thus, the problem of solving (5.25) has been transformed into the task of finding the actual displacement field $\mathbf{u}(\mathbf{r})$ which fulfils (5.40) for every possible $\delta\mathbf{u}(\mathbf{r})$. The only restriction to the virtual variation $\delta\mathbf{u}(\mathbf{r})$ is that $\mathbf{u}(\mathbf{r}) + \delta\mathbf{u}(\mathbf{r})$ must still fulfil the given boundary conditions.

Minimization problems of this kind can be solved by the *Finite Element Method* (FEM) [ZT87, GRT93, Bra97]. Very briefly stated, it finds a minimum of (5.38) by expanding $\mathbf{u}(\mathbf{r})$ into a series of basis functions, and minimizing $\Pi(\mathbf{u})$ as a function of the coefficients of this series.

Mathematically speaking, the FEM represents a general method to find a function $\mathbf{u}(\mathbf{r}) \in W$ which satisfies

$$a(\mathbf{u}(\mathbf{r}), v(\mathbf{r})) = b(v(\mathbf{r})) \quad \text{for all } v(\mathbf{r}) \in W, \quad (5.41)$$

where W is a given set of functions. The *bilinear form* $a(u, v)$ with $a : W^2 \rightarrow \mathbb{R}$ associates a real number (\mathbb{R} being the set of real numbers) to every pair of functions $u(\mathbf{r}), v(\mathbf{r})$ from W , and can represent any combination of differential or integral operators. Similarly, $b(v)$ is a *linear form* $b : W \rightarrow \mathbb{R}$. The elasticity problem (5.40) becomes a special case of the more general (5.41) by identifying $v(\mathbf{r})$ with the virtual displacement $\delta\mathbf{u}(\mathbf{r})$.

For the solution of (5.41) one chooses in practice a set of N linearly independent functions from W , called $w_1(\mathbf{r}), \dots, w_N(\mathbf{r})$. The set of linear combinations of the w_i constitutes a subspace W_s of W . Instead of solving the general problem (5.41) one now restricts oneself to finding a solution $u_s \in W_s$ which satisfies

$$a(u_s, v_s) = b(v_s) \quad \text{for all } v_s \in W_s. \quad (5.42)$$

In other words, the *ansatz* for an approximate solution is $u(\mathbf{r}) \approx u_s(\mathbf{r}) = \sum_{i=1}^N u_i w_i(\mathbf{r})$, with coefficients u_i to be determined. Similarly, the function $v(\mathbf{r})$ is replaced by $v_s(\mathbf{r}) = \sum_{i=1}^N v_i w_i(\mathbf{r})$.

The great advantage of this technique is that it allows to transform the variational problem ((5.41)) into a system of linear algebraic equations. Due to the linearity of $a(., .)$ and $b(.)$ we obtain a relation for the coefficients u_i, v_i :

$$\sum_{i,j=1}^N a(u_j w_j, v_i w_i) = \sum_{i=1}^N b(v_i w_i) \quad \Rightarrow \quad \sum_{i,j=1}^N a(w_j, w_i) u_j v_i = \sum_{i=1}^N b(w_i) v_i \quad (5.43)$$

from which the coefficients v_i can be eliminated. This yields, in matrix notation:

$$\sum_{j=1}^N A_{ij} u_j = b_i. \quad (5.44)$$

The elements of the matrix A_{ij} and the vector b_i can be calculated from the linear forms a and b and the basis functions $w_i(\mathbf{r})$ alone. Thus, the remaining task is to solve the system (5.44) for the coefficients u_i , from which the approximate solution $u_s(\mathbf{r})$ of the elasticity problem can be reconstructed. Equation (5.44) represents a *matrix inversion problems*, which can be solved numerically by very efficient methods. If N is not too large (say, $N \leq 10^3 - 10^4$) then A^{-1} can be calculated by *direct methods* — such as Gauss' algorithm — which yields a solution that is exact up to rounding errors. For larger N *iterative methods* such as the *Gauss-Seidel relaxation method*, the *conjugate gradient method* or *multigrid methods* can be used [Lüb96, PTV95]. These methods provide a series of increasingly accurate approximate solutions for the coefficient vector u_i , and can be interrupted when sufficient precision is achieved.

Many of the iterative methods are particularly efficient if the matrix A is *sparse*, i.e. if a large number of elements A_{ij} is zero. For our elasticity problem this can be achieved by choosing the basis functions $w_i(\mathbf{r})$ in such a way that each w_i has finite values only on a small subdomain $V_i \subset V$, and is zero everywhere else in the volume V of the body. In this case, A_{ij} vanishes for all combinations of indices i, j except for those whose domains V_i and V_j overlap.

Therefore, in a practical Finite-Element calculation of strain fields the sample volume is subdivided into small cells, as shown in Fig. 5.4 for the case of a rectangular surface grating. In general, the larger the number N of cells, the closer the calculated approximate solution v_s will be to the real solution $u(\mathbf{r})$. If the cell subdivision is sufficiently fine one can restrict the choice of $w_i(\mathbf{r})$ to linear functions of the coordinates (x, y, z) inside V_i [GRT93]. Such *linear finite elements* were used for all the calculations shown in this thesis.

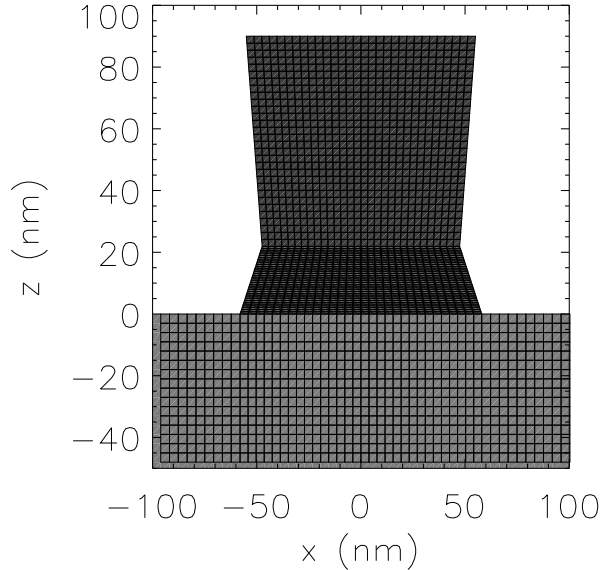


Figure 5.4: Example of a subdivision of a grating into small cells.

Application to strain fields in surface gratings

Finite Element calculations can be carried out in practice with the help of commercially available program packages. They allow to define the sample geometry interactively on the computer screen. The user must decide upon the subdivision of the sample volume into small cells, and specify the boundary conditions. The basis functions w_i are then automatically determined by the program as linear functions of the coordinates inside the single cells. Furthermore, the calculation of the elements of the matrix A_{ij} and the vector b_i as well as the solution of the resulting matrix equation are automatically handled by the software. On output, a value of \mathbf{u} is provided for the nodes of each of the cells, and the values of ϵ_{ij} are calculated by numerical differentiation.

Nevertheless, it is not obvious how such commercial packages can be used for our task. Two difficulties, a conceptual and a more practical one, remain which must be solved before we can successfully apply a FEM program to calculate strain fields in surface gratings:

- FEM program packages (just like elasticity theory in general) are conceived in order to solve *macroscopic* problems. They ignore the discontinuous atomic structure of matter and the existence of crystal lattices in solids. No easy way is provided to implement the boundary condition for lattice matching at the interfaces of a pseudomorphically grown structure. Therefore, one has to find an alternative method to incorporate (5.30) into the calculation.

The technique we used was to define the different materials in the structure as having different temperatures, and thereby to replace the difference in lattice parameters by a different (fictitious) thermal expansion.

- Some of the programs, such as the one available for our calculations, do not even allow to enter the elastic constants in the short form C_{11} , C_{12} and C_{44} for cubic crystals. Instead, they expect the elastic constants in their “engineering version”, i.e. the full set of three Young moduli E_i , three Poisson ratios ν_{ij} and three shear moduli G_{ij} , to be given on input.

The formulae for the conversion between these two sets of elastic constants are given in Appendix A. They were implemented in a program package which we developed to facilitate the practical application, and which can be used for any quaternary III-V semiconductor material like $\text{Ga}_x\text{In}_{1-x}\text{As}_y\text{P}_{1-y}$. This program first calculates the values of C'_{ijkl} by linear interpolation (*Vegard's law*) between the values for the corresponding binary III-V materials, which can be found in the literature [Ada82, Ada85]. Then, it transforms the stiffness tensor to C''_{ijkl} in the coordinate system chosen for the FEM calculation, and finally calculates the “engineering” constants from the components of C''_{ijkl} .

These difficulties being solved, the FEM can now be applied to calculate grating strain fields. Two simplifications can be made at the beginning: Since the grating structure is symmetrical along the grating wire direction, the solution $\mathbf{u}(\mathbf{r})$ must be independent of the y -coordinate. Furthermore, the structure cannot relax in the y -direction, so that the strain component ϵ_{yy} is constant and given by (5.32). The combination of these two aspects is known as the *plane strain condition* [TG87] and allows to reduce the problem to an actually two-dimensional problem. It is therefore sufficient to define the geometry of the grating *cross section*, and to subdivide it into two-dimensional cells. We chose a trapezoidal shape for these cells. Preliminary studies showed that cell lengths of about 5-10 nm represented a sufficiently fine subdivision to capture most of the spatial variation of $\mathbf{u}(\mathbf{r})$, except near the edges of the grating structure. In what follows, we will call these cells explicitly “Finite Element cells” in order to stress the fact that they are not identical with the crystal unit cells. In fact, every Finite Element cell contains several hundred atoms. The deformation inside each of these cells is assumed to be uniform, and is represented by one single value of the strain tensor.

5.4 X-ray diffraction from strained crystals and from strained gratings

In Section 5.3 we have presented a method to solve numerically the equations for the grating strain field which result from elasticity theory. However, it is still not clear whether the description provided by elasticity theory is valid in the case of nanoscopic semiconductor structures. Therefore, a method for independent experimental verification of strain field calculated in this way is required.

Preliminary studies exist that have observed a non-uniform strain relaxation in $\text{Ga}_x\text{In}_{1-x}\text{As}/\text{GaAs}$ quantum wires by photoluminescence (PL) [TMY92] and, in a more spatially resolved way, by transmission electron microscopy (TEM) [CRS94]. The results have been compared with FEM models of the strain field for both PL on InAsP/InP quantum wires [NHW95] and electron microscopic methods applied to GeSi/Si quantum dots [CAS94]. However, these studies cannot be considered as an experimental proof of the validity of continuum elasticity theory in nanostructures: PL, on the one hand, is an integral method which does not allow to probe the spatial variation of strain inside the structures. TEM, on the other hand,

does provide spatial resolution, but only for a small area on the sample surface and never in a representative, statistically significant way for the distortion in the whole sample volume.

Therefore, a more thorough experimental test of the applicability of elasticity theory to semiconductor nanostructures is still due. X-ray diffraction is particularly well suited for this scope for two reasons: X-rays penetrate more deeply into matter than electrons do, and the diffracted intensity, being generated by interference, is sensitive simultaneously to the strain field in the whole volume of the body. We now derive the basic formulae needed to simulate X-ray diffraction patterns from distorted structures. This will later allow to compare experimental and calculated X-ray diffraction reciprocal space maps, and thereby to test the predictions of elasticity theory in a quantitative way.

The diffraction of X-rays from a distorted crystal can be calculated in the framework of both the kinematical and the dynamical scattering theory. The exact, dynamical approach relies on the Takagi-Taupin equations [Tak62, Tau64, Tak69]. They provide a set of partial differential equations for the spatial variation of the amplitudes of the incident and diffracted beams inside the deformed crystal. In order to solve them for complex sample geometries, it is possible to numerically integrate the equations along the propagation direction of the beams, starting from the entrance face, as demonstrated for instance in [Moc99].

For our type of samples, a simpler approach based on kinematical theory is sufficient. Shortly stated, we calculate the diffracted intensity by coherent superposition of the contributions from the individual *finite elements* introduced in Section 5.3. The material inside each cell is considered to be uniformly strained, and diffracts around a *shifted* Bragg peak whose position is determined by the local strain.

The approximation contained in a kinematical approach is justified because the typical thickness of the strained layers on the surface of our grating samples is of the order of some 100 nm only. Multiple scattering events as well as extinction effects inside this region can most probably be neglected. The only correction beyond pure kinematical theory that we will apply is to include the effect of refraction, which is important especially in the case of GID (see Section 2.3). The validity of this method can be definitely established only by comparing the calculations with experimental data (see Part III).

In order to derive an expression for the kinematical intensity similarly to (5.2) we consider the susceptibility $\chi'(\mathbf{r}')$ of a deformed crystal. The electron density is assumed to follow the distortion of the crystal lattice, so that $\chi'(\mathbf{r}') = \chi'(\mathbf{r} + \mathbf{u}(\mathbf{r})) = \chi(\mathbf{r})$. If the deformation field is weak or varies slowly, more precisely if $(\partial \mathbf{u}_i / \partial x_j) \cdot \mathbf{u}_j \approx 0$, we can approximate $\mathbf{r} \approx \mathbf{r}' - \mathbf{u}(\mathbf{r}')$. By renaming the variables ($\mathbf{r}' \rightarrow \mathbf{r}$) we obtain for the susceptibility

$$\chi'(\mathbf{r}) = \chi'(\mathbf{r} - \mathbf{u}(\mathbf{r})) = \sum_{\mathbf{h}} \chi_{\mathbf{h}} e^{i\mathbf{h} \cdot (\mathbf{r} - \mathbf{u}(\mathbf{r}))}. \quad (5.45)$$

In writing (5.45) we made use of the *Takagi approximation* [Tak62]: The Fourier series for the distorted crystal is written with the same Fourier coefficients $\chi_{\mathbf{h}}$ as in the undistorted case. In fact, the $\chi_{\mathbf{h}}$ correspond to the Fourier transform of one unit cell of the crystal lattice. Thus, the Takagi approximation is equivalent to assuming that the single unit cells are not significantly distorted, but only displaced *en bloc*. Any non-uniform variation of $\mathbf{u}(\mathbf{r})$ takes place on larger length scales. Therefore, the relative strength of the Bragg peaks, as described by $\chi_{\mathbf{h}}$, remains unchanged. Only their positions in reciprocal space, which are determined by the exponential term in (5.45), are affected by the strain field.⁴

To obtain the kinematical scattering signal we need to calculate

$$S(\mathbf{Q}) = \int \chi'(\mathbf{r}) \Omega(\mathbf{r}) e^{-i\mathbf{Q}\cdot\mathbf{r}} d^3\mathbf{r} = \sum_{\mathbf{h}} \chi_{\mathbf{h}} \int e^{-i\mathbf{h}\cdot\mathbf{u}(\mathbf{r})} \Omega(\mathbf{r}) e^{-i(\mathbf{Q}-\mathbf{h})\cdot\mathbf{r}} d^3\mathbf{r}. \quad (5.46)$$

In analogy to (5.5) we can isolate the signal in the vicinity of Bragg peak \mathbf{h} by writing

$$S_{\mathbf{h}}(\mathbf{Q}) = \chi_{\mathbf{h}} \int \Omega(\mathbf{r}) e^{-i\mathbf{h}\cdot\mathbf{u}(\mathbf{r})} e^{-i(\mathbf{Q}-\mathbf{h})\cdot\mathbf{r}} d^3\mathbf{r} \quad (5.47)$$

⁴Actually, the diffracted signal from a distorted crystal can be derived in more general terms, without making use of the Takagi approximation. Kuriyama [Kur67] found a formulation, based on a quantum theory of X-ray diffraction, which needs to assume only that the electron wave functions of neighbouring atoms in the distorted crystal do not overlap.

The important difference with respect to (5.5) is that we now have to Fourier-transform a product of two functions, the shape function $\Omega(\mathbf{r})$ and the characteristic function of the strain field

$$U_{\mathbf{h}}(\mathbf{r}) = e^{-i\mathbf{h} \cdot \mathbf{u}(\mathbf{r})}. \quad (5.48)$$

Two different approaches can be employed to perform this calculation. The first one is based on yet another application of the convolution theorem. It consists in calculating $S_{\mathbf{h}}$ as convolution of the single Fourier transforms [BG95, HPB98]:

$$S_{\mathbf{h}}(\mathbf{Q}) = \chi_{\mathbf{h}} \int \Omega^{\text{FT}}(\mathbf{q}') U_{\mathbf{h}}^{\text{FT}}(\mathbf{q} - \mathbf{q}') d^3 q'. \quad (5.49)$$

The evaluation of (5.49) can be further simplified by making use of the lateral grating periodicity which causes the Ω^{FT} to be non-zero only at the (Q_x, Q_y) -positions of the grating truncation rods. In this way, the integral in (5.49) can be converted into a discrete sum, which can more easily be calculated on a computer. Such an approach is convenient when the strain field is considered in terms of an analytical approximation, so that U^{FT} can be calculated exactly prior to evaluation of (5.49).

In our case, where the strain field is available as numerical data from the FEM simulation, it is more desirable to use the FEM data for $\mathbf{u}(\mathbf{r})$ directly, without first having to numerically calculate the Fourier transform of $e^{-i\mathbf{h} \cdot \mathbf{u}(\mathbf{r})}$. Therefore, we developed a second, alternative method for the quantitative evaluation of formula (5.49). This approach aims at using the same formula (5.5) again, which is possible only if the material inside $\Omega(\mathbf{r})$ has a uniform crystalline lattice. Therefore, the structure amplitude of the grating is not calculated in one step any more, but split into a sum of contributions from the single Finite Element cells, each of which is uniformly strained internally. We define $\Omega_m(\mathbf{r})$ as the shape function of the m -th Finite Element cell, having value 1 only on the small domain V_i . The total diffracted intensity results from a superposition of the individual elements' contributions

$$S_{\mathbf{h}}(\mathbf{Q}) = \sum_{m=1}^N S_{\mathbf{h}}^m(\mathbf{Q}) = \sum_{m=1}^N \chi_{\mathbf{h}}^m \int_{V_m} \Omega_m(\mathbf{r}) e^{i\mathbf{h}(\mathbf{r} - \mathbf{u}(\mathbf{r}))} e^{-i\mathbf{Q}\mathbf{r}} d^3 r \quad (5.50)$$

Inside each finite element the displacement varies linearly with the distance from some reference point \mathbf{r}_0^m (with components \mathbf{r}_{0j}^m):

$$\mathbf{u}_i(\mathbf{r}) - \mathbf{u}_i(\mathbf{r}_0^m) = \frac{\partial \mathbf{u}_i}{\partial x_j} \cdot (\mathbf{r}_j - \mathbf{r}_{0j}^m) \quad (5.51)$$

For the practical calculations, we defined the reference point \mathbf{r}_0^m as the middle of the upper horizontal edge in the case of trapezoidal Finite Element cells. For such locally uniform strain one can introduce a local *distorted reciprocal lattice* [Tak69, HPB98] whose vectors \mathbf{h}' are given by

$$\mathbf{h}' = \mathbf{h} - \nabla \psi_{\mathbf{h}} \quad \text{with} \quad \psi_{\mathbf{h}}(\mathbf{r}) = \mathbf{h} \cdot \mathbf{u}(\mathbf{r}), \quad (5.52)$$

so that if (5.50) we can replace $\mathbf{h}(\mathbf{r} - \mathbf{u}(\mathbf{r}))$ by $\mathbf{h}'\mathbf{r} - \mathbf{h}\mathbf{u}(\mathbf{r}_0^m)$. With the definition of a new reduced scattering vector $\mathbf{q}' = \mathbf{Q} - \mathbf{h}' = \mathbf{q} - \delta\mathbf{h}'$ the final formula for the structure amplitude becomes

$$S_{\mathbf{h}}(\mathbf{Q}) = \sum_{m=1}^N \chi_{\mathbf{h}}^m \Omega_m^{\text{FT}}(\mathbf{q}') e^{-i\mathbf{q}'\mathbf{r}_0^m} e^{-i\mathbf{h}\mathbf{u}(\mathbf{r}_0^m)}, \quad (5.53)$$

where we splitted off a phase factor $e^{-i\mathbf{q}'\mathbf{r}_0^m}$ from the shape function Ω^{FT} to account explicitly for the absolute position of element m within the structure. With (5.53) we have recovered a formula which, apart from being a sum of N terms, is very similar to (5.5). The main difference is that the argument of Ω^{FT} is now the distance between the scattering vector \mathbf{Q} and the position \mathbf{h}' of the Bragg peak of the *distorted* material.

Let us mention that our approach leading to (5.53) is based on an idea which we call the *fixed-window-approximation*: The external shape Ω^m is assumed not to be essentially affected by the deformation of

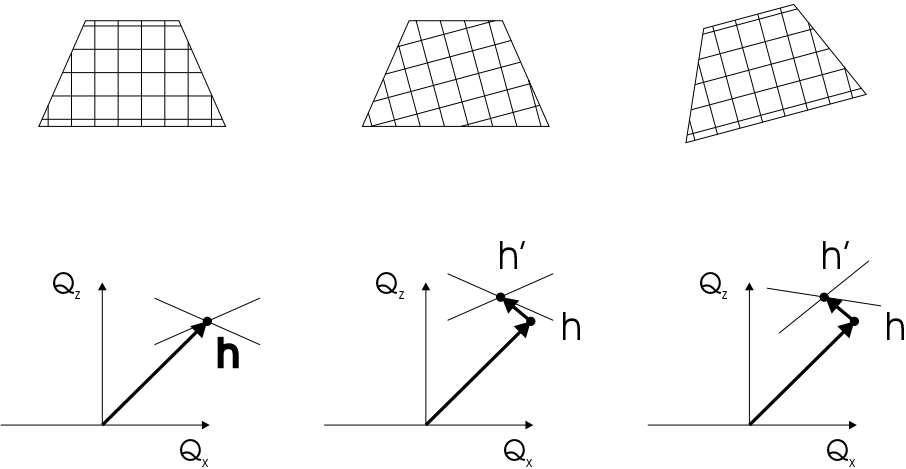


Figure 5.5: Contribution of one distorted cell to the diffracted intensity (one term in the sum (5.53)), demonstrated with the example of a symmetrical trapezoidal shape and a pure rotation. Left: the undistorted case. The element contributes according to the Fourier transform of its shape function Ω^{FT} (symbolized by the cross), centered around the Bragg peak \mathbf{h} of the bulk material. Center: the fixed-window-approximation. The external shape of the cell is assumed to remain unchanged – it constitutes a “window” through which one views the crystal lattice “behind” it. Therefore, the cross retains the same form in reciprocal space, but is centered around the RLP \mathbf{h}' of the distorted (here: rotated) material. Right: the complete case. The external shape is subject to the same distortion as the crystal lattice. As a result, the cross is not only displaced from \mathbf{h} to \mathbf{h}' , but also rotated in reciprocal space.

the material inside, it is neither compressed nor expanded nor rotated. In other words, the shape function constitutes an immobile “window frame” through which we observe the changes in the crystal lattice inside. This approach is valid as long as the extension of each domain V_m is much larger than the absolute displacements $|\mathbf{u}(\mathbf{r})|$, so that the effects at the edges of $\Omega(\mathbf{r})$ are comparatively insignificant. In cases where this doesn’t hold, $\Omega(\mathbf{r})$ must be replaced in (5.46) by a *distorted shape function* Ω' which is defined by $\Omega'(\mathbf{r} + \mathbf{u}(\mathbf{r})) = \Omega(\mathbf{r})$. This is illustrated in Fig. 5.5.

A very interesting property of (5.53) is that it can easily be generalized to structures consisting of several different materials, in contrast to (5.5) which was necessarily limited to homogeneous gratings. By writing \mathbf{h}'^m instead of \mathbf{h}' , and accordingly $\mathbf{q}'^m = \mathbf{Q} - \mathbf{h}'^m$, to allow for different Bragg peak positions of the materials within the different cells m , expression (5.53) can also be used without any formal change to obtain the diffracted intensity from a strained *superlattice* grating [BLG00]. The interference of signals originating from the different layers in a multilayered structure is automatically handled correctly by (5.53), provided the lattice matching conditions at the interfaces within the structure have been taken into account correctly in the preceding FEM calculation of the strain field.

To evaluate formula (5.53) quantitatively we still need an expression for the Bragg-peak shift $\delta\mathbf{h} = \mathbf{h}' - \mathbf{h}$ in (5.52) as a function of $\mathbf{u}(\mathbf{r})$, $\epsilon_{ij}(\mathbf{r})$ and/or $\omega_{ij}(\mathbf{r})$. From (5.20) and (5.21) we have $\partial\mathbf{u}_i/\partial x_j = \epsilon_{ij} + \omega_{ij}$, so that (5.51) in conjunction with (5.52) yields

$$\delta\mathbf{h}_i = -(\nabla\psi_{\mathbf{h}})_i = -\mathbf{h}_j (\epsilon_{ji} + \omega_{ji}) = (-\epsilon_{ij} + \omega_{ij}) \mathbf{h}_j. \quad (5.54)$$

In the last step we made use of the antisymmetry of the rotation tensor ω_{ij} . In words, formula (5.54) states that the shift of each reciprocal lattice point consists of two contributions: $\delta\mathbf{h} = \delta\mathbf{h}^{\text{strain}} + \delta\mathbf{h}^{\text{rot}}$. The first one, due to strain ϵ_{ij} , is *opposite* in sign (or simply *reciprocal*) to the effects in real space. Compressions of the crystal lattice result in elongations of the reciprocal lattice vectors and vice versa, and similarly for a change in angles due to shear strains. The second contribution, due to rotations ω_{ij} , is *identical* in sign to

the real-space rotation of the crystal lattice, and can be written as

$$(\delta \mathbf{h})^{\text{rot}} = \boldsymbol{\omega} \times \mathbf{h} = \begin{pmatrix} \omega_{xz}\mathbf{h}_z - \omega_{xy}\mathbf{h}_y \\ \omega_{yx}\mathbf{h}_x - \omega_{yz}\mathbf{h}_z \\ \omega_{zy}\mathbf{h}_y - \omega_{zx}\mathbf{h}_x \end{pmatrix} \quad (5.55)$$

Qualitatively speaking, the reciprocal lattice is fixed with respect to the real-space crystal lattice and rotates together with it.

For grating structures the strain is most conveniently expressed in the system of reference parallel to the grating wires, where the strain tensor assumes the simple form

$$\epsilon_{ij} = \begin{pmatrix} \epsilon_{xx} & 0 & \epsilon_{xz} \\ 0 & \epsilon_{||}^0 & 0 \\ \epsilon_{xz} & 0 & \epsilon_{zz} \end{pmatrix}. \quad (5.56)$$

The according strain-induced shift in reciprocal lattice vector results to be

$$\delta \mathbf{h}^{\text{strain}} = - \begin{pmatrix} \epsilon_{xx}\mathbf{h}_x + \epsilon_{ex}\mathbf{h}_z \\ \epsilon_{||}^0\mathbf{h}_y \\ \epsilon_{xz}\mathbf{h}_x + \epsilon_{zz}\mathbf{h}_z \end{pmatrix} \quad (5.57)$$

This relation is perfectly general and valid for gratings with any azimuthal orientation of the wires on the sample surface, and for any crystalline structure of the grating material. To give a specific example, let us consider the (HKL) -reflection of a cubic material with a bulk lattice constant a_0 , so that $\mathbf{h} = \frac{2\pi}{a_0}(H, K, L)$ in the crystallographic reference system. Furthermore, let the grating wires be parallel to the $[1\bar{1}0]$ -direction. In this case, $\delta \mathbf{h}$ can be expressed in terms of the integers H, K and L via

$$\delta \mathbf{h}^{\text{strain}} = - \frac{2\pi}{a_0} \begin{pmatrix} \epsilon_{xx}(H+K)/\sqrt{2} + \epsilon_{xz} L \\ \epsilon_{||}^0(K-H)/\sqrt{2} \\ \epsilon_{xz}(H+K)/\sqrt{2} + \epsilon_{zz} L \end{pmatrix} \quad (5.58)$$

There exists an alternative way to derive the change in peak position $\delta \mathbf{h}$. It is based on (1.3) and calculates the change in the three reciprocal basis vectors $\delta \mathbf{Q}^n$ by first finding the shifted real-space vectors \mathbf{a}'^n . This method appears to be slightly less elegant because the practical calculations involved depend more strongly on the choice of coordinate system. However, for the special case of a $[1\bar{1}0]$ -oriented surface grating of cubic material a formula similar to (5.58) was found [DBW98].

In the case of pure triaxial compression or dilatation, in the absence shear strains, equation (5.57) can be interpreted very directly. In fact, $(1+\epsilon_{xx})$ represents the relative dilatation along the x -direction, and the corresponding change in Q_x is given by the inverse factor:

$$Q'_x = \frac{1}{1+\epsilon_{xx}} Q_x \approx (1-\epsilon_{xx}) Q_x. \quad (5.59)$$

This explains expression (5.57), apart from the terms in ϵ_{xz} . However, such a simple approach cannot be used in the general case since the contributions due to shear strain are often important, as has been shown for certain cases in a recent study [DBW98].

To summarize this section, the diffracted intensity from a general, non-uniformly structure is described quantitatively by a combination of equations (5.15), (5.53), (5.55) and (5.57). It is calculated as a sum over contributions from locally uniformly strained regions, which diffract around Bragg peak positions which are shifted due to the effect of strain and rotation of the crystal lattice. Therefore, their shape function Ω^{FT} takes as argument the *distorted* reduced scattering vector \mathbf{q}' . For our practical simulations, these regions are identical to the Finite Element cells introduced in the previous section. For trapezoidal shape of the cells, an analytical expression for Ω^{FT} has already been derived in Section 5.1. The formulae for triangular, rectangular or parallelogram shape result from (5.15) as special cases with $b=0$, $p_{l/r}=0$ and $p_l=p_r$. With this *repertoire* of shapes, almost arbitrarily complicated sample structures can be constructed and subsequently analyzed.

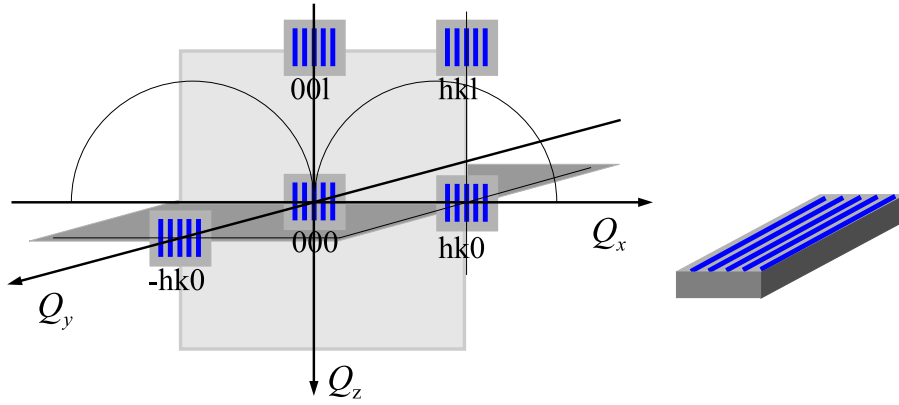


Figure 5.6: Sketch of the different reflections that will be used in our strain investigation procedure: symmetrical reflections (for samples with a [001]-oriented surface, these are the reciprocal lattice points $00L$), asymmetrical reflections (RLPs HKL), and two types of in-plane reflections (RLPs $HK0$). [BL99]

5.5 Conclusion – A general procedure for strain investigation

In this chapter we have developed the theory to calculate diffraction patterns from laterally periodic surface nanostructures. Section 5.1 introduced the general theoretical scheme and derived the expression for the diffracted intensity from a strain-free homogeneous grating. In Section 5.4 we generalized the result to strained gratings. Equation (5.53) constitutes a general recipe for simulating diffracted intensities on the basis of strain fields calculated with the methods presented in Sections 5.2 and 5.3. In this way one can predict the diffraction pattern for a given Bragg reflection \mathbf{h} and given sample parameters.

It is now time to reverse the direction of arguing. The question is: Which kinds of measurements must be done around which crystallographic reflections, and subsequently compared with the corresponding calculations, in order to obtain as reliable and complete information as possible about the strain field in a real sample?

The answer is essentially determined by the fact the the function $U_{\mathbf{h}}$ in (5.47) contains the scalar product of \mathbf{h} and $\mathbf{u}(\mathbf{r})$. The diffraction pattern at reflection \mathbf{h} is therefore influenced by the component of the displacement field $\mathbf{u}(\mathbf{r})$ parallel to the scattering vector \mathbf{Q} , or equivalently by the spacing, shear and rotation of those lattice planes which are perpendicular to \mathbf{Q} .

In order to measure the *complete* strain field, one therefore has to record the diffraction patterns of several reflections. Three categories of reflections can be distinguished (see Fig. 5.6):

Symmetrical reflections: The diffraction pattern around these reflections is influenced by the grating shape and the *vertical* displacement component \mathbf{u}_z .

Asymmetrical reflections Their diffraction pattern is influenced by the grating shape as well as by both the vertical *and* the lateral component of the displacement field \mathbf{u} (more exactly, a linear combination of both).

Grazing incidence diffraction (reflections with $L=0$): In this case the diffraction pattern is exclusively determined by the grating shape and the *lateral* displacement component \mathbf{u}_x .

Grazing incidence diffraction allows to limit the X-ray penetration depth by choosing very small angles of incidence α_i (see Section 2.3). In this way, one can study the lateral strain component as a function of depth below the sample surface [LBP99].

Another advantage of GID in the context of strain investigations in surface gratings is that it allows to selectively “switch on and off” the strain sensitivity: Due to the translational symmetry of a grating along the wire direction \mathbf{e}_y , the material can relax laterally only along the direction of patterning \mathbf{e}_x . Therefore,

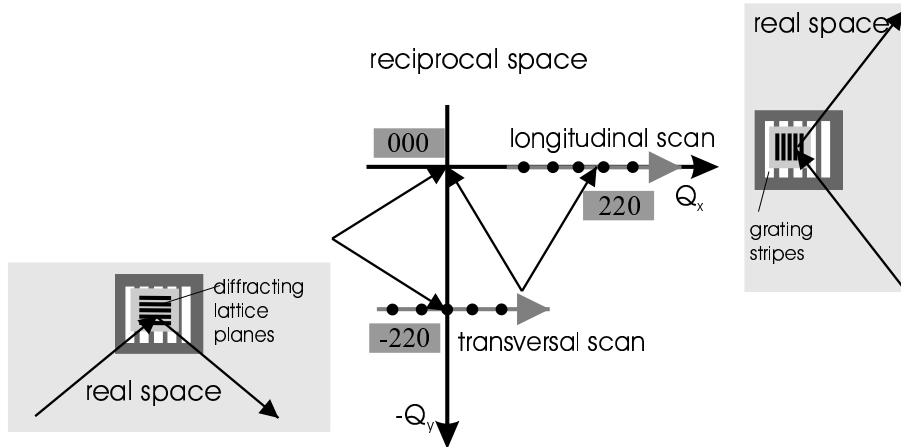


Figure 5.7: Geometry of grazing incidence diffraction measurements from gratings. Transversal scans are exclusively sensitive to the grating shape, whereas longitudinal scans show an additional influence of the grating-induced strain relaxation. [BL99]

at reflections with $\mathbf{h} \parallel \mathbf{e}_y$ the product $\mathbf{h} \cdot \mathbf{u}(\mathbf{r})$ in (5.48) is zero and $U_{\mathbf{h}}$ is identically equal to 1, so that expression (5.49) for the structure amplitude reduces to the one for a non-strained structure, (5.5). Such reflections \mathbf{h} are therefore sensitive to the grating shape only, and not affected by the grating-induced strain; measurements in their vicinity will be called *GID in morphological mode* [BL99].

For reflections which are perpendicular to the grating wires ($\mathbf{h} \parallel \mathbf{e}_x$), on the other hand, the scalar product $\mathbf{h} \cdot \mathbf{u}$ is different from zero, and the diffraction pattern is additionally influenced by strain. Measurements around these reflections will be called *GID in strain-sensitive mode*.

To give an example, let us assume the sample is patterned along the crystallographic [110]-direction, i.e. the quantum wires extend along [1̄10]. In this case, the reciprocal lattice point 220 is a “strain-sensitive” one, while the reciprocal lattice point 2̄20 is a “morphological” one.

An alternative terminology makes use of the notions *transversal scans* and *longitudinal scans*. In fact, at the morphological GID reflections, the series of intersection points of the GTRs with the Q_x - Q_z -plane is aligned *perpendicular* to \mathbf{h} , whereas at the strain-sensitive reflections they are parallel to \mathbf{h} (see Fig. 5.7). Therefore, in order to record the intensity variation along a line through the series of GTRs (at given Q_z) in a strain-insensitive mode, one has to perform a *transversal scan* ($\Delta Q \perp \mathbf{h}$); the same task in a strain-sensitive mode can be completed by a *longitudinal scan* ($\Delta Q \parallel \mathbf{h}$).

With these facts in mind, we can now present our general systematical procedure for investigation of strain relaxation in surface gratings:

1. First, perform grazing incidence diffraction in morphological mode to investigate the grating shape.
2. Then, measure GID-curves in strain-sensitive mode to study the lateral strain component in the sample, including its variation with depth (measurable by tuning the penetration depth of the probing X-ray via the angle of incidence).
3. Record reciprocal space maps around symmetrical reflections in order to additionally probe the vertical strain component.
4. Study one or more asymmetrical reflections to test the combined influence of lateral *and* vertical strain.
5. Simultaneously, the geometrical information obtained in the previous steps can be used to calculate a theoretical strain field, and therefrom to simulate a diffraction pattern I^{sim} .

6. By comparing the simulation with the experimental RSM and successively refining the geometrical parameters, one can reach a maximum correspondence between experimental and simulated data, as determined by the familiar residual error sum

$$\chi^2 = \sum_i \left(\frac{I_i^{\text{exp}} - I_i^{\text{sim}}}{\sigma_i} \right)^2, \quad (5.60)$$

and thus find a best approximation to the actual strain field. For the experimental uncertainties σ_i we use the square root $\sqrt{I_i^{\text{exp}}}$ of the measured intensity. The most efficient algorithms for automatic minimization of (5.60), such as the *Levenberg-Marquardt-method*, require the derivative of I^{sim} with respect to the parameters. In our case, these derivatives are not available analytically. Our quantitative fits will therefore be done with simpler minimization methods like the *simplex method* and *Powell's method* [PTV95].

Chapter 6

Monitoring the strain evolution in the fabrication process of gratings

As mentioned in the Introduction to this thesis, the most popular method to produce surface nanostructures is to first grow a planar strained layer epitaxially on a substrate, and then to structure it laterally via etching. The strain state in the initial planar layer is characterized by tetragonal distortion of the layer lattice which adapts its lateral lattice parameter to the substrate. The vertical lattice parameter reacts in the opposite sense; the exact amount of this reaction depends on the Poisson ratio of the respective material.

The etching of a grating into the strained layer then increases the free, non-constrained surface and therefore allows the material to partially relax the tetragonal strain by expanding or contracting laterally. For device applications, the gratings produced in this way are often overgrown by an embedding layer in order to protect them from corrosion, oxidation and/or mechanical damage. Such an embedding layer modifies the strain state in the sample. As a side effect this will influence the device properties via the electronic band structure. We will see that the burying has a re-straining influence: It partially reverses the grating-induced strain relaxation. The details of this effect are not obvious at first sight. It is therefore necessary to investigate experimentally the strain effects of the burying growth step.

The aim of this Chapter is to describe a systematic experimental study of the strain evolution in the different technological steps of the fabrication process. In particular, we will analyze the effect of the burying growth step on the strain state in the grating with the help of X-ray diffraction and elasticity theory.

6.1 Introduction. The samples

We investigate the strain evolution with the example of $\text{Ga}_x\text{In}_{1-x}\text{As}_y\text{P}_{1-y}$ samples. This material system plays an important role in optoelectronic devices for optical fiber communication [ASD87, Gal91]. Our samples were produced by *CNET France Télécom* (Bagnex). They serve as an example to demonstrate how X-ray methods can be successfully used to study the effect of etching and embedding on the strain state in a semiconductor structure.

The series of three samples was produced as follows: A strained $\text{Ga}_x\text{In}_{1-x}\text{As}_y\text{P}_{1-y}$ layer with a nominal thickness of 200 nm was grown onto an InP substrate via metal-organic vapour phase epitaxy (*MOVPE*). Its composition of $x = 0.22$, $y = 0.44$ leads to a nominal lattice parameter of $a^{\text{layer}} = 5.861 \text{ \AA}$ and a nominal lattice mismatch of $\varepsilon_{xx} \approx +1.2 \cdot 10^{-3}$ with respect to the substrate (lattice parameter $a^{\text{InP}} = 5.869 \text{ \AA}$). The positive sign of ε_{xx} indicates that the layer is under *tensile* strain.

A grating was fabricated in the layer by holographic exposure and subsequent chemical etching, with a nominal grating periodicity of $D=227 \text{ nm}$ and an approximately trapezoidal grating profile. The grating lines were oriented along the $[1\bar{1}0]$ -direction. A second grating was produced similarly and subsequently overgrown with an embedding InP layer with a nominal thickness of 250 nm. A third sample, a “reference sample” without any strain, was produced by etching the same type of grating into the surface of a pure



Figure 6.1: Sketch of the geometries of the three samples investigated in this Chapter: a simple, strain-free grating at the surface of an InP substrate (left), a strained-layer surface grating (center), and a similar grating, additionally buried under an InP layer (right).

InP substrate. The geometry of the whole series of samples is shown schematically in Fig. 6.1. Table 6.1 shows the values of tetragonal and orthorhombic strain which result from the nominal sample parameters.

x	y	a	$\epsilon_{ }$	ϵ_{zz}^0	ϵ_{xx}^{ortho}	ϵ_{zz}^{ortho}
0.78	0.44	5.8616 Å	$+1.235 \cdot 10^{-3}$	$-1.296 \cdot 10^{-3}$	$-2.04 \cdot 10^{-5}$	$-6.37 \cdot 10^{-4}$

Table 6.1: Values of strain in the samples 2 and 3, as predicted from the nominal composition for the two limiting cases of complete lattice matching (tetragonal strain) and full relaxation (orthorhombic strain) (see eqs. (5.33)–(5.36)). From left to right: compositions of the layer material $\text{Ga}_x\text{In}_{1-x}\text{As}_y\text{P}_{1-y}$; lattice parameter; lattice mismatch with InP substrate $\epsilon_{||}$ and resulting tetragonal vertical strain ϵ_{zz}^0 ; lateral and vertical orthorhombic strain ϵ_{xx}^{ortho} , ϵ_{zz}^{ortho} .

Three diffractometers were used to analyze these samples:

- a Philips MRD diffractometer ($\text{Cu}-K_{\alpha 1}$ emission line), for the symmetrical diffraction maps [LBT97]
- the D23 beamline of LURE, Orsay [ELK92], in the triple crystal mode, with a Si-111 double-crystal monochromator, a Ge-111 analyzer crystal and a wavelength of 1.54 Å, for the asymmetrical diffraction maps [BLG99a]
- the BW2 beamline of HASYLAB, Hamburg [DSSS95], also in the triple crystal mode (Si-111 monochromator and analyzer), and with a wavelength of $\lambda = 1.362$ Å, for the grazing incidence diffraction measurements [LBP99].

To characterize the three samples first in view of the grating shape and then in view of their internal strain field, we now apply the strategy exposed in Section 5.5 to each of them in sequence.

6.2 Simple surface grating: a reference case

Since the first sample consists of one material only, there is no reason for any strain or strain relaxation to appear in the volume of the material. The reciprocal space structure of this sample should consist of a characteristic cross pattern, identically replicated around each reciprocal lattice point, as discussed in Chapter 5. In particular, the diffraction pattern should be perfectly symmetrical around the reciprocal lattice point, without any shift of the intensity envelope away from the substrate peak.

6.2.1 Grazing incidence diffraction

Fig. 6.2 shows a transversal scan across the $2\bar{2}0$ -reflection, performed at $q_z = 0.032$ Å⁻¹. The high number of lateral satellites gives evidence of a remarkably perfect lateral periodicity. The detailed form of the scan is determined by the grating shape. In the present context the striking feature is that the intensity

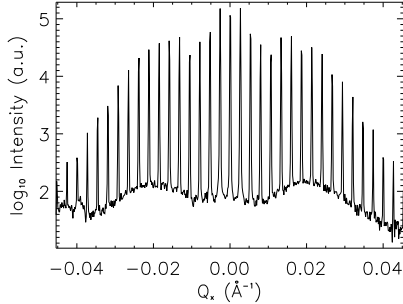


Figure 6.2: Grazing incidence diffraction from a simple InP-grating: transversal Q_x -scan across the $2\bar{2}0$ -reflection.

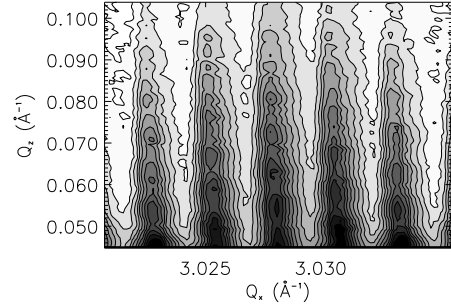


Figure 6.3: Grazing incidence diffraction from a simple InP-grating: reciprocal space map of the 220 -reflection.

distribution is symmetrical with respect to the CTR at $Q_x = 0$. However, this is true for the transversal scan from any symmetrically shaped grating, even in the presence of strain.

The complementary longitudinal scan at the 220 -reflection, on the other hand, now is in principle sensitive to an additional strain influence. Therefore, the fact that the reciprocal space map measured at the 220 -reflection (Fig. 6.3) is also symmetrical around the position of the crystal truncation rod at $Q_x = 3.028 \text{ \AA}^{-1}$ is a clear indication for the absence of any strain in the sample. Even though in GID geometry only the upper half of the diffraction pattern can be detected, we observe a series of thickness fringes which are arranged in branches that progressively shift in q_z from one GTR to the next. The inclination of these branches is related to the sidewall slopes of the grating [BL99]. These can be determined as $p_r = p_l = \frac{dx}{dz} = 0.82 \pm 0.02$, corresponding to a sidewall inclination angle of $(39 \pm 1)^\circ$.

6.2.2 Coplanar diffraction

In the corresponding symmetrical diffraction map measured around the 004 peak (Fig. 6.4), we now observe the full cross-pattern. The grating truncation rods in this map are less intense with respect to the background. This is mainly due to the fact that the map was measured with a laboratory X-ray source. Furthermore, a strong analyzer streak is visible. Nevertheless it is possible to recognize that all four branches of the cross pattern are present, and that their intensities are equilibrated.

We can thus conclude that no evidence of either lateral or vertical strain or strain relaxation is present in this sample. The diffraction patterns are exclusively determined by the grating shape. The geometrical parameters which can be obtained by a quantitative evaluation of the experimental data are given in Table 6.2.

D_{SG}	t	b	g	p_l	p_r
$237 \pm 1 \text{ nm}$	$70 \pm 2 \text{ nm}$	$67 \pm 1 \text{ nm}$	$55 \pm 1 \text{ nm}$	0.83 ± 0.02	0.83 ± 0.02

Table 6.2: Geometrical parameters of the simple InP grating, as obtained from the evaluation of the GID- and 004 -data. D_{SG} is the lateral grating period, t the grating depth, b the grating top width, g the groove width, and p_l and p_r are the left and right grating sidewall slopes.

In summary, the investigation of this sample can be considered as a test case for our experimental method. The study has shown the influence of a one-dimensional lateral patterning onto the diffraction pattern. We could isolate the influence of the grating shape, separately from any strain inhomogeneities. The diffraction patterns at different crystallographic reflections were highly similar to each other, and allowed

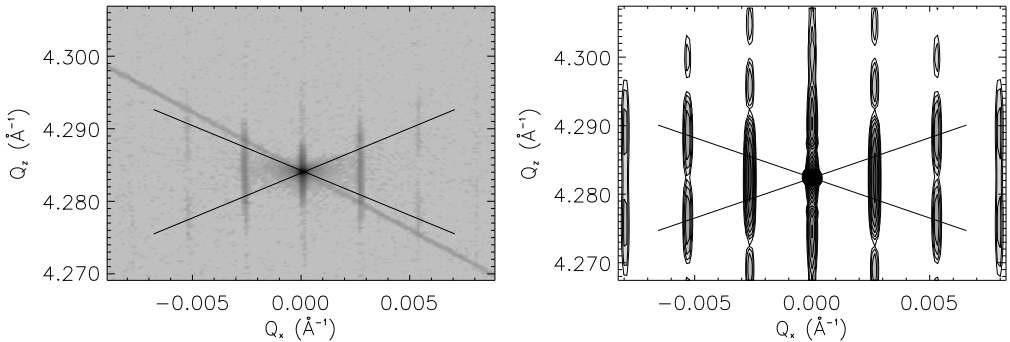


Figure 6.4: Experimental (left) and fitted (right) symmetrical diffraction from a simple InP-grating: reciprocal space map of the 004-reflection. The sample shows no evidence of strain relaxation, since the upper and lower as well as the left and right branch of the cross pattern (indicated by black lines) around the InP-004 Bragg peak are perfectly symmetrical. The strong line which crosses the experimental image from the upper left to the lower right corner is the analyzer streak. [SL97]

to characterize the grating shape in a unique way. If on other samples we now observe relevant differences between complementary reflections, we will be able to identify them as due to the additional influence of strain relaxation.

6.3 Growth of a strained layer. Grating-induced strain relaxation

The strained-layer grating can now be investigated by the same procedure:

6.3.1 Grazing incidence diffraction

Fig. 6.5 shows experimental scans measured in grazing incidence diffraction from the second sample, the strained layer grating. The lowest curve (a) is a transversal scan at the $\bar{2}\bar{2}0$ -reflection for an incidence angle of $\alpha_i = 0.21^\circ$. Since this angle is below the critical angle of bulk InP ($\alpha_c = 0.26^\circ$ at $\lambda = 1.362 \text{ \AA}$), it leads to a penetration depth of 4-5 nm (see the discussion in Section 2.3, in particular eq. (2.39)). The curve is symmetrical around the position of the crystal truncation rod, as expected for a symmetrical grating shape. This changes when the sample is turned by 90° around its surface normal in order to record a longitudinal scan at the $2\bar{2}0$ -reflection (curves (b)-(d) in Fig. 6.5). Now the maximum of the intensity envelope is clearly shifted away from the position of the reciprocal lattice point towards the right hand side, as indicated by the arrows in Fig. 6.5. This shift is a first indication for strain relaxation in the sample, since from a crystallographic point of view the two reflections are equivalent, and the preliminary investigation of the simple grating showed that the grating shape influences both reflections in the same way. A hypothetical surface miscut can also be ruled out as a reason for this asymmetry: It might modify the ratios of absolute intensities between both reflections, but it could not give rise to an asymmetry in just one type of scan. Moreover, the miscut can be found from the 004-maps (see Fig. 6.4 as well as Figs. 6.6 and 6.8 below) to be very small (below 0.05°). Therefore, the asymmetry in the longitudinal scans can only be due to a net strain relaxation in the surface grating.

In curve (b) (measured with an incidence angle of $\alpha_i = 0.1^\circ$, which corresponds to a penetration depth of 2-3 nm) the shift amounts to $\Delta Q / |Q| = 1.1 \cdot 10^{-3}$ towards larger $|Q|$ (smaller lattice parameters), which means that the initial tensile strain (lattice mismatch) in the layer of $1.2 \cdot 10^{-3}$ is almost completely relaxed at the grating top.

The shift varies with the penetration depth: In curve (c) (measured at $\alpha_i = 0.2^\circ$) it is less pronounced, and curve (d) ($\alpha_i = 0.4^\circ$) is already almost symmetrical. Here the penetration depth is as large as some 100 nm. Therefore the X-rays average over the contributions from the grating and from large parts of the

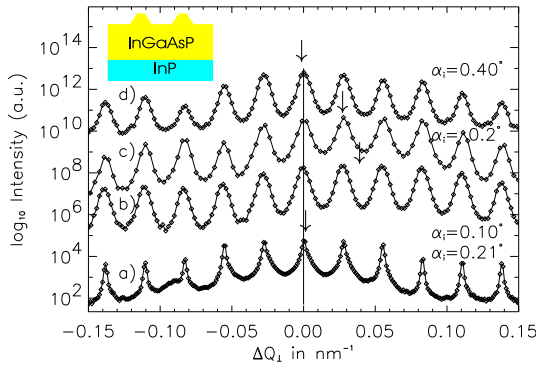


Figure 6.5: *GID from a strained layer surface grating. One transversal (lowest curve (a)) and three longitudinal (upper curves (b)-(d)) GID-scans for different α_i . The transversal scan is symmetric around the substrate reciprocal lattice point, since it is insensitive to strain. The longitudinal scans show a clear shift of the maximum of the intensity envelope away from the substrate RLP. This shift decreases with increasing α_i , i.e. with increasing penetration depth: The strain relaxation is strongest in the top layer of the grating, and decreases as one approaches the interface with the substrate. [LBP99]*

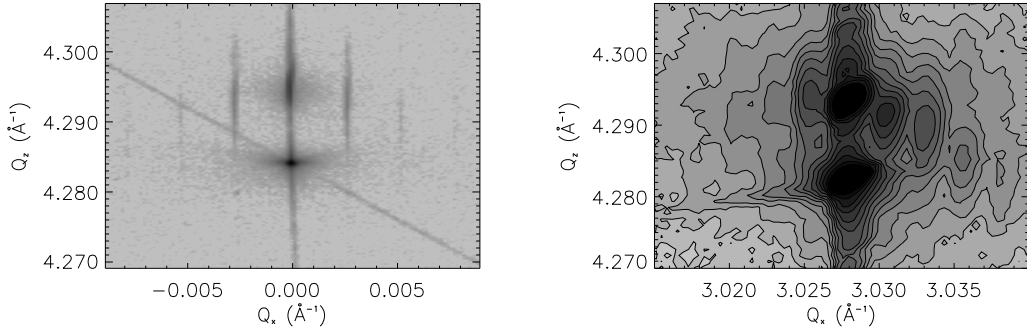


Figure 6.6: *Coplanar diffraction from a strained-layer surface grating. Left: 004-map, right: 224-map. [SL97]*

planar layer below. Since the strain relaxation is important only near the grating top and the planar layer remains almost fully strained, the curve at such high α_i shows no strong shift towards larger $|Q|$.

We have thus seen that GID allows to investigate the lateral strain relaxation in a grating. By performing Q_x -scans for various angles of incidence one can determine the mean relaxation at different penetration depths, and thereby measure the variation of the strain field as a function of the depth below the sample surface.

6.3.2 Coplanar diffraction

In the 004-reciprocal space maps of the same sample (left image in Fig. 6.6), we observe two main peaks, the substrate peak at $Q_z^{\text{InP}} = 4.282 \text{ \AA}^{-1}$, and the layer peak above it. The substrate peak is not surrounded by lateral satellites. The reason is that the substrate material is laterally unstructured, since the grating is etched only into the strained layer and does not reach the substrate.

The layer peak, on the other hand, is indeed surrounded by grating truncation rods. However, the intensity pattern does not exhibit the cross pattern that was to be expected from the trapezoidal grating shape. The arrangement of visible satellites can be interpreted as the lower branch of a cross pattern centered at the layer peak; the upper branches of the cross are considerably weakened. This is an indication for *non-*

homogeneous strain relaxation in the grating: If a simple homogeneous net strain relaxation occurred in the grating, the cross pattern would be shifted in reciprocal space, but its general form would not be affected, as can be seen from eq. (5.4). By inversion of the argument, the disappearance of the upper half is therefore a clear sign of a non-uniform variation of the lattice parameter inside the grating.

The corresponding 224-map on the right side of Fig. 6.6 is less well resolved, due to the less sophisticated triple-crystal arrangement used in the measurement. On the other hand, the much higher flux of X-rays at the synchrotron source allowed to record a larger number of grating truncation rods. Our picture shows GTRs up to the fourth order on each side.

Apart from this, the asymmetrical map exhibits the same general characteristics as before: no (or only very weak) lateral satellites around the substrate peak, and stronger lateral satellites around the layer peak. The satellite pattern shows a strong asymmetry not only between the upper and lower branch, but also between the left and right hand side. The lower right branch is much stronger than the other three. In other words there is a slight shift of the intensity envelope from the layer peak to the right, towards larger $|Q|$, once again indicating a partial relaxation of the tensile lateral strain in the grating region.

6.4 Overgrowth of an embedding layer. Counteraction on strain

In the case of the third sample, the buried grating, the main open questions to be investigated are the following:

- Quality control of the embedding growth step: Is the grating completely buried? Is the surface of the cap layer perfectly planar?
- Influence of the embedding growth step on the strain state: Is there a counteraction of the embedding layer on the strain relaxation in the grating region?

To answer these questions, we start once again by grazing incidence diffraction.

6.4.1 Grazing incidence diffraction

Fig. 6.7 shows two transversal (lower curves) and two longitudinal (upper curves) Q_x -scans for different angles of incidence. The first relevant difference with respect to the previous sample is that in the transversal scans we observe only one main peak, but no lateral satellites. This is due to the fact that the structure factor contrast ($\chi_h^a - \chi_h^b$) between the layer material and the embedding InP is very low at the 220-type of reflections. Therefore, the X-rays in this diffraction geometry “see” a homogeneous crystal, and are not sensitive to the inner compositional modulation of the sample. Also, the $2\bar{2}0$ -reflection is insensitive to the strain modulation. For these two reasons, the diffraction pattern is laterally completely unstructured.

Although the X-rays cannot detect the lateral morphological patterning in the buried grating region they would still be sensitive to the structure factor difference between the sample and the air above it. If there were a remaining periodic modulation of the surface morphology, we would be able to detect it via the appearance of grating truncation rods. They might generally be weak, but their relative intensity should be strongly enhanced for very small angles of incidence, due to the decreasing penetration depth. The fact that even the curve for $\alpha_i = 0.15^\circ$ (penetration depth: 3-4 nm) shows no grating rods thus indicates that the sample surface is perfectly flat. The overgrowth process has terminated with a completely planar surface.

The longitudinal scans (curves (c) and (d) in Fig. 6.7), on the other hand, do show lateral satellites. A remaining compositional variation at the sample surface cannot be the reason, since it has been excluded by the findings in the transversal scans. As all other experimental conditions remained the same, the appearance of satellites can only be explained through the additional strain sensitivity of the 220-reflection. The X-rays in this scattering geometry “see” a laterally periodic modulation of the strain field, more exactly of its lateral component ε_{xx} .

Only one pair of satellites can be observed, and no higher order GTRs are visible. This can be explained by the fact that the strain field varies less abruptly than does the morphology which gave rise to the GTRs of the non-buried sample. The continuity conditions for the displacement field across the interfaces do only allow a smooth, continuous variation of the strain. The lateral modulation is nearly sinusoidal. In a

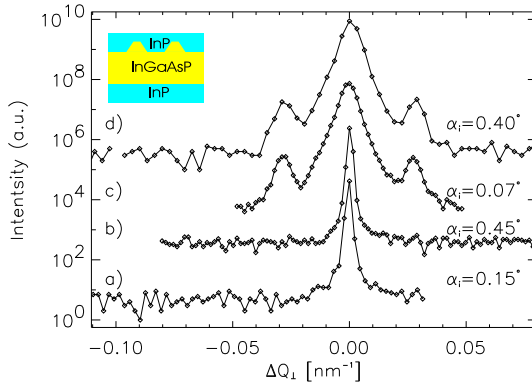


Figure 6.7: *Grazing incidence diffraction from a buried grating. Transversal scans at the $2\bar{2}0$ -reflection (lower curves: (a) and (b)), and longitudinal scans at the 220 -reflection (upper curves: (c) and (d)), each for two different angles of incidence.* [LBP99]

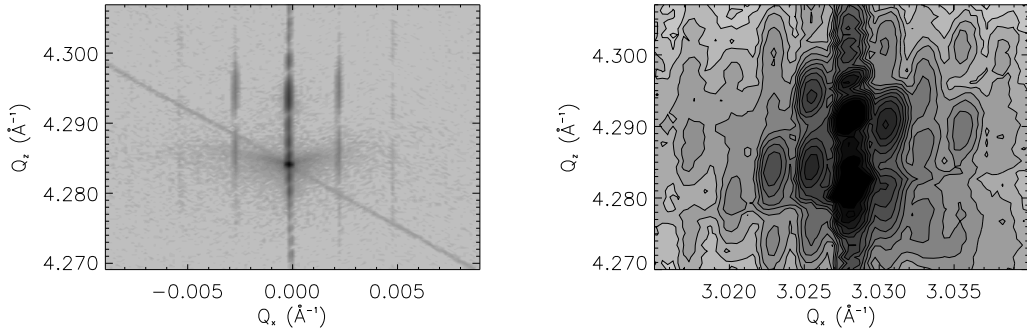


Figure 6.8: *Coplanar diffraction from a buried grating (sample AT6). Left: 004-map, right: 224-map.* [SL97]

first-order approximation (valid for small absolute displacements $\Delta \mathbf{u}$, which is certainly applicable for the weakly strained material in our samples) this then explains that only the first order GTRs have measurable intensity.

6.4.2 Coplanar diffraction

The coplanar reciprocal space maps from the buried sample (004- and 224-map in Fig. 6.8) also show relevant differences with respect to the non-buried case: The upper half of the satellite pattern around the layer peak reappears. This is an indication for a re-straining effect of the embedding material on the grating region. Since the two materials are in contact not only at the substrate-grating interface, but also at the interface between grating and embedding layer (at the grating top as well as at the grating sidewalls), the grating region cannot relax as freely as it could before. Therefore the strain field in the grating is less non-uniform, and we observe a less noticeable deviation from ideal cross pattern in reciprocal space.

Furthermore, the GTRs now have measurable intensity also at the Q_z -height of the substrate peak. This reflects the fact that the substrate material is now laterally structured as well. It fills the “valleys” of the grating and forms what could be called a *negative grating*, which gives rise to satellites around the substrate peak.

Nevertheless, one cannot say that there are two distinct cross patterns around the layer and the substrate peak. The lattice parameters of the two materials are so similar and their 004-peaks so close to one another

that their respective diffraction patterns interfere, causing one single cross-like pattern to appear, which is centered in the middle between the two main peaks.

Another difference with respect to Fig. 6.6 is that there is much less diffuse scattering around the layer peak. In the case of the non-buried sample the diffuse intensity was presumably caused by random strain fluctuations in the grating, which are now partially damped by the influence of the embedding layer. A slightly more speculative interpretation is that a random variation of the grating *morphology* (surface roughness) also contributed to the diffuse scattering, and that this roughness was smoothed by the burying growth step.

The 224-map (right part of Fig. 6.8) reflects the same overall changes in the strain state. GTRs are as clearly visible around the substrate peak as around the layer peak. The left-right-asymmetry of the intensity envelope around the layer peak is less pronounced than in the case of the non-buried grating, which indicates once again a weaker net strain relaxation. However, the reversal of the relaxation is not complete: The satellite on the right of the layer peak is still slightly stronger than the one on the left. This intensity shift towards larger $|Q|$ gives evidence of a small remaining relaxation of the tensile strain in the grating. The contraction of the layer grating has to be compensated by a corresponding expansion of the material in the “negative” grating in order to preserve the overall periodicity. This is indeed the case, as can be seen from the fact that there is a stronger group of satellites on the left side of the substrate peak than on the right.

6.5 Calculation of strain fields and reciprocal space maps

In order to interpret and model these experimental results we calculate theoretically the strain fields in both samples. The calculation is based on the principles presented in Chapter 5. Input data combine the geometrical parameters given as nominal values by the crystal grower and those extracted from the preliminary GID investigation. With the help of the strain fields calculated in this way, we then simulate reciprocal space maps. The aim is to reproduce the experimental maps of Figs. 6.6 and 6.8 and thereby to verify the calculated strain fields not only in view of their main qualitative features but also more quantitatively. The simulation is based on the semi-kinematical approach presented in section 5.4. Fig. 6.9 shows the results for the 004-map (left) and the 224-map (right) of the surface grating (above) and the buried grating (below).

Let us briefly discuss the images in Fig. 6.9 and compare them with their experimental counterparts. All four maps show two main peaks along the crystal truncation rod, one at the InP-004 reciprocal lattice point, and one at the layer material’s 004-peak (above). In the symmetrical diffraction map of the non-buried structure (upper left image), the substrate peak is laterally unstructured, while the layer peak above it is surrounded by the four branches of a cross-pattern. The two lower branches are considerably stronger than the upper ones, just like in the experimental map. The asymmetrical map (upper right) of this sample also shows no lateral satellites at the substrate peak. The cross pattern with all four branches around the layer peak is easier to recognize than in the experimental map — in fact, two branches were hidden in the background of Fig. 6.6. The striking feature is that the simulation reproduces quite well the shift of the intensity envelope to the right, and the general intensity ratios between the satellites.

For the buried grating the symmetrical map (lower left image) shows a cross pattern whose upper and lower parts are of similar intensity. It is centered at a point in the middle between substrate and layer peak - just like in the experimental map (see left image in Fig. 6.8). In the corresponding asymmetrical map (lower right in Fig. 6.9) a cross centered at the same place appears again, but now with first order satellites that are stronger in the lower left and upper right branches than in the other two branches. It was exactly this aspect in the experimental map (right image in Fig. 6.8) which we could interpret as a remaining relaxation in the grating and as a related expansion of the embedding layer.

In summary, the simulated coplanar diffraction maps agree well with the findings in the experimentally measured maps. No attempt has been made here to fit the sample geometries or the material parameters, since the aim was not to obtain a perfect agreement, but only to establish the validity of our methodical approach. Nevertheless, all essential features of the experimental maps are perfectly reproduced.

The same approach can also be used to simulate the grazing incidence diffraction measurements. In this case, the effects of reflection from and transmission through the sample surface and the refraction correction play a more important role than in high-angle coplanar diffraction. Since our simulation method

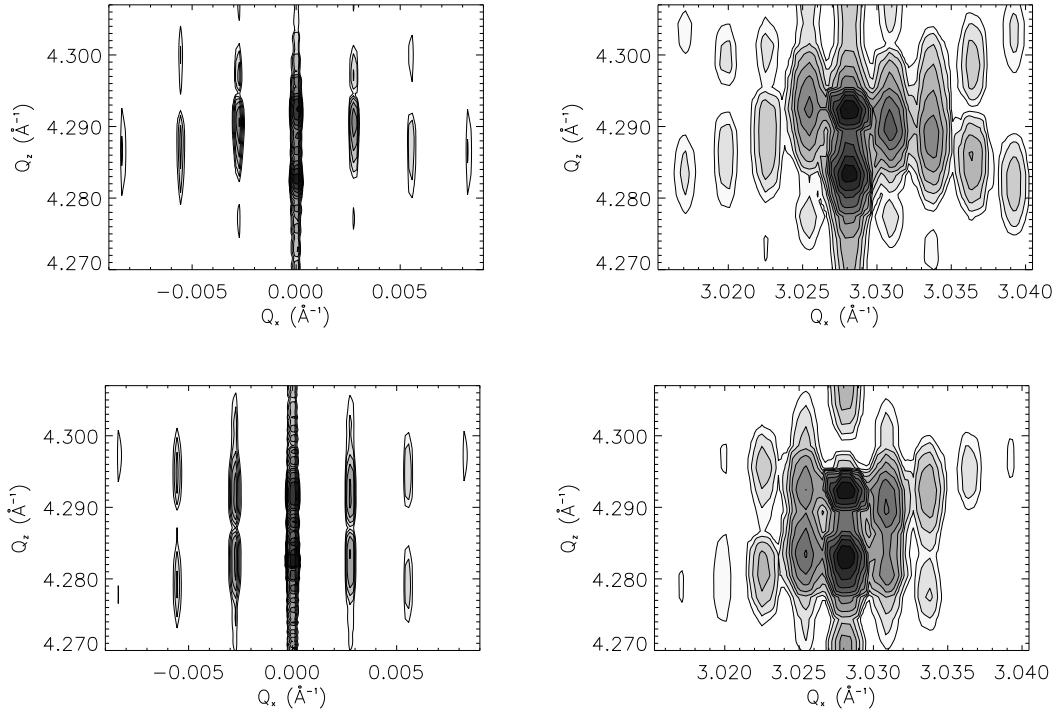


Figure 6.9: Best fit for the 004- (left) and 224- (right) maps of the strained-layer surface grating (above) and the buried grating (below). Although the fit is not perfect, the essential features discussed in the previous sections are all reproduced.

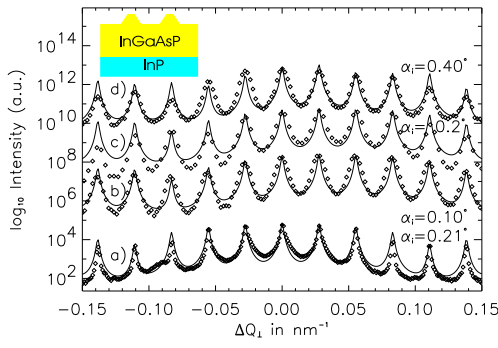


Figure 6.10: Fit of GID scans for the strained layer grating (sample AT5): one transversal (curve (a)) and three longitudinal (curves (b)-(d)) GID-scans for different α_i . Dotted curve: measurements; full line: calculation based on the strain fields given in section 6.5. The strain relaxation is strongest in the top layer of the grating, and decreases as one approaches the interface with the substrate. [LBP99]

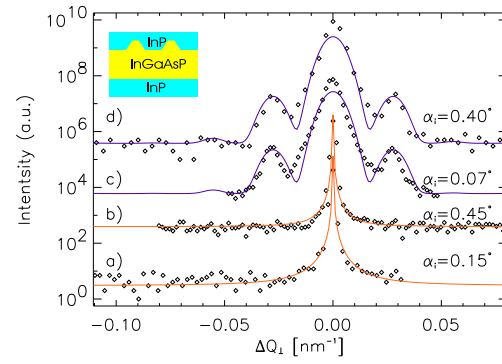


Figure 6.11: Grazing incidence diffraction from a buried grating: transversal (curves (a)-(b)) and longitudinal (curves (c)-(d)) Q_x -scans, each for two different angles of incidence. [LBP99]

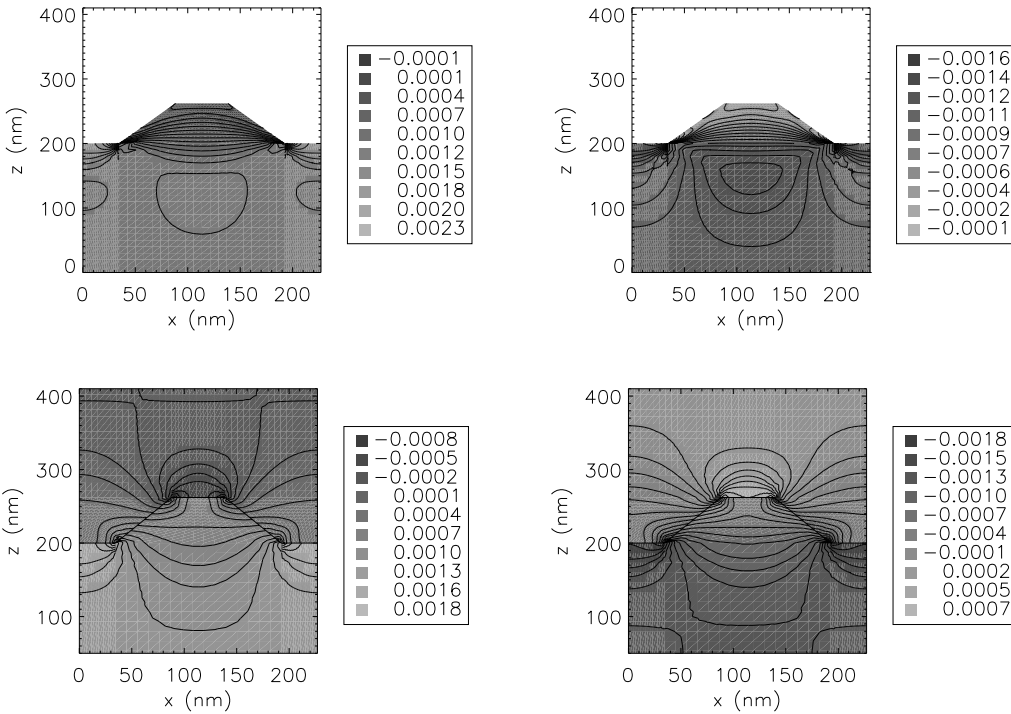


Figure 6.12: Final result for the strain fields of the gratings: lateral (left) and vertical (right) strain component of the strained-layer surface grating (above) and the buried grating (below).

is based on a DWBA, these influences are correctly taken into account in the calculation. The results in Figs. 6.10 and 6.11 demonstrate that a very satisfactory agreement can be achieved in this case as well. The curves for the non-buried sample (Fig. 6.10) reproduce the shift of the intensity envelope to the right in the longitudinal scans at small α_i (curves (b) and (c)). The symmetry is correctly restored for the longitudinal scan at higher α_i (curve (d)). In Fig. 6.11, the transversal scans (curves (a) and (b)) of the buried sample show no lateral satellites, and they do reappear in the longitudinal scans (curves (c) and (d)), just like in the experiment. The fact that the first order grating truncation rods have non-zero intensity even for $\alpha_i = 0.07^\circ$ proves that the remaining periodical strain modulation at the surface of the embedding layer is indeed sufficient to give rise to such lateral satellites.

The resulting strain fields on which these calculations are based are represented in Fig. 6.12. It shows the lateral (left) and vertical (right) components (ϵ_{xx} and ϵ_{zz}) of the strain field in the surface grating (above), and in the buried grating (below).

We see from Fig. 6.12 that the planar layer is under relatively homogeneous tensile strain (positive values close to the lattice mismatch, $\epsilon_{xx} \approx +1.2 \cdot 10^{-3}$). The grating itself can relax laterally. The relaxation increases with distance from the planar layer, up to almost complete relaxation ($\epsilon_{xx} \approx \epsilon_{xx}^{\text{ortho}} = -2 \cdot 10^{-5}$, see Table 6.1) near the grating top. The relaxation (contraction) in the grating induces an opposite strain (expansion) in the planar layer, which is mainly localized near the corners of the grating. This is necessary to preserve the overall periodicity of the structure along the lateral direction (absolute displacement $u_x = 0$ at the boundaries $x = 0$ and $x = D_{\text{SG}}$).

The vertical strain component reacts to the changes in the lateral one. In the planar layer the material is compressed in z -direction (tensile strain $\epsilon_{zz} < 0$). In the grating this strain is increasingly relaxed and approaches the fully relaxed state ($\epsilon_{zz}^{\text{ortho}} = -6.3 \cdot 10^{-4}$, see Table 6.1) at the top of the grating. Once again, the strongest effects are localized near the corners of the grating.

In the buried sample the absolute variation of lateral strain is less strong. Even near the grating top the value of ϵ_{xx} remains positive. The embedding material directly above is slightly compressed (negative ϵ_{xx}) as a reaction to the remaining contraction of the grating material. In the grating valleys, on the other hand, it has to expand slightly (positive ϵ_{xx}) to fill the “gap” opened by the contraction of the grating.

The displacement has to be continuous (condition of pseudomorphic growth) across all the interfaces between the two materials (the grating top and valley bottom as well as the grating sidewalls). This is indeed the case, as can be concluded from the continuity of the contour lines in the plot. The absolute value of lateral strain, on the other hand, jumps at the interface, but this is merely due to the fact that the strains are calculated with respect to two different systems of reference, namely the bulk lattice of the two respective materials.

From both images of the buried grating we see that the strain field is not confined to the grating region, but extends far into both the planar $\text{Ga}_x\text{In}_{1-x}\text{As}_y\text{P}_{1-y}$ layer and the embedding InP layer. In the left image of Fig. 6.12 we can also observe that a periodic lateral strain modulation reaches the sample surface — this agrees very well with our experimental findings in the last section.

Due to the agreement between the measured diffraction patterns and the calculated reciprocal space maps, these strain fields can be considered to be experimentally verified, and our method to calculate them promises to be a valid one.

6.6 Conclusion

In summary, we have presented an experimental method to investigate strain in lateral surface nanostructures, demonstrated with the example of weakly strained surface and buried gratings. The method is based on a combination of different X-ray diffraction geometries: *Grazing incidence diffraction* in two different measuring modes is used to initially determine the grating shape, independently of any strain consideration, and then to probe the lateral strain component in a depth-resolved way. *Symmetrical coplanar diffraction* is sensitive to the complementary vertical strain component, while *asymmetrical diffraction* is employed to investigate both components simultaneously. The data evaluation relies on the calculation of the distortion field in the structures based on elasticity theory, and on a subsequent simulation of the diffraction curves and maps.

The results obtained in this Chapter show that the strain fields in the gratings are strongly non-uniform. The relaxation increases from the substrate-layer interface to the top of the grating. This is the case even for an initial lattice mismatch as low as $1.2 \cdot 10^{-3}$. The buried grating was found to have completely planar surface. The growth of an embedding layer partially reverses the strain relaxation in the grating, but a periodically modulated strain field remains in the grating region and extends into the planar part of the embedding layer up to the sample surface.

The good agreement achieved between experimental and simulated maps can be considered as a first proof that elasticity theory — which is *a priori* a macroscopic theory — is indeed an appropriate tool to calculate the lattice distortion in semiconductor structures even of *nanoscopic* dimensions.

Chapter 7

Strained layer gratings with variable shape

In Chapter 6 we have studied the effects of strain relaxation in surface gratings using the example of two samples with weak tensile strain. The present Chapter continues this investigation with another set of two samples which differ from the previous ones in two respects: The strain in the layer is now compressive rather than tensile, and the absolute value of the lattice mismatch between layer and substrate material is far higher than before. The effects of strain relaxation are therefore more drastic.

We will see how the method of data evaluation via simulation of reciprocal space maps based on calculations of the strain field can be turned into an even more quantitative method, by including a fitting procedure that automatically performs loops over the different parameters. With the help of this optimized procedure we will study to what extent our method is sensitive to parameters such as the material composition and the details of the grating geometry.

7.1 Introduction. The samples.

We study the effects of variations in the grating geometry with the example of two samples grown at the *Ecole Polytechnique Fédérale de Lausanne* (EPFL). A planar layer of $\text{Ga}_x\text{In}_{1-x}\text{As}$ was deposited on an InP substrate by chemical beam epitaxy. The intended composition of $x = 0.40$ corresponds to a lattice parameter of $a^{\text{lay}} = 5.896 \text{ \AA}$ and thus a lateral strain of $\epsilon_{xx} = -4.67 \cdot 10^{-3}$ in the pseudomorphically grown planar layer (with a negative value indicating *compressive* strain in the layer). Two surface gratings were produced by holographic exposure and subsequent chemical etching with a solution of $\text{H}_3\text{PO}_4\text{-H}_2\text{O}_2\text{-H}_2\text{O}$. The direction of patterning was along the crystallographic [110]-direction in one case, and along the [1 $\bar{1}$ 0]-direction in the other case. The etching mechanism is known to be sensitive to such differences in orientation, in that it leads to differently shaped gratings. In the present case, one trapezoidal and one rectangular grating were obtained. Furthermore, the etching solution is very material-selective, and does

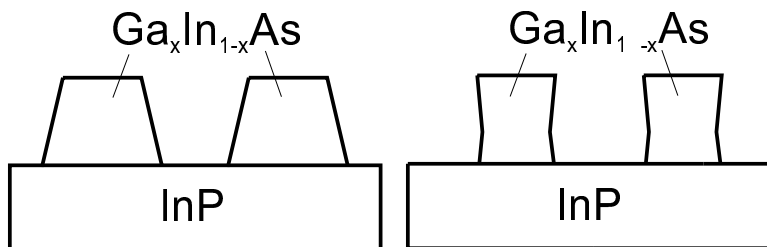


Figure 7.1: Geometry of the samples: trapezoidal grating (left) and nearly rectangular grating (right).

x	a	$\epsilon_{ }$	ϵ_{zz}^0	$\epsilon_{xx}^{\text{ortho}}$	$\epsilon_{zz}^{\text{ortho}}$
0.40	5.8964 Å	$-4.674 \cdot 10^{-3}$	$+4.667 \cdot 10^{-3}$	$+6.15 \cdot 10^{-5}$	$+2.303 \cdot 10^{-4}$

Table 7.1: Values of strain in the gratings, as predicted from the nominal composition for the two limiting cases of complete lattice matching (tetragonal strain) and full relaxation (orthorhombic strain) (see eqs. (5.33)-(5.36)). From left to right: compositions of the layer material $\text{Ga}_x\text{In}_{1-x}\text{As}$; lattice parameter; lattice mismatch with InP substrate $\epsilon_{||}$ and resulting tetragonal vertical strain ϵ_{zz}^0 ; lateral and vertical orthorhombic strain $\epsilon_{xx}^{\text{ortho}}$, $\epsilon_{zz}^{\text{ortho}}$.

almost not attack the InP substrate. Therefore, the etching process stops at the interface with the substrate, and the bottom of the grating valleys is nearly flat. A sketch of the sample geometries is presented in Fig. 7.1. SEM images of both samples are shown in Fig. 7.2. The values of tetragonal and orthorhombic strain resulting from the nominal parameters are calculated in Table 7.1.

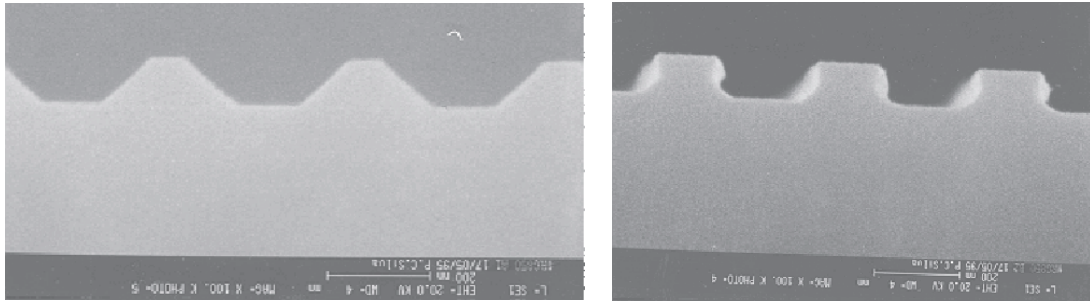


Figure 7.2: Scanning electron microscopy (SEM) images of the samples to be discussed in this Chapter. Left: trapezoidal grating, right: (nearly) rectangular grating. [Gai98]

7.2 Trapezoidal grating

7.2.1 Shape investigation

The microscopic image in Fig. 7.2 shows that the grating shape is an approximately symmetrical trapeze — at least at the special spot on the sample surface where the image was recorded. In order to obtain more representative information on the grating shape and its variation over the whole surface of the sample we performed an initial study of this sample by *grazing incidence diffraction* at the BW2 beamline of HASYLAB, Hamburg. The method was identical to the one used in Chapter 6, and included Q_x scans in a *morphological mode* and in a *longitudinal mode*, as well as Q_z -scans to determine the intensity profile along the grating truncation rods. Detailed results of this investigation, concerning the grating shape as well as the depth profile of lateral strain relaxation, can be found in a recent article ([BLG99b], see also [BL99]). The important point in our present context are the mean geometrical parameters which could be extracted from the mentioned study, and on which our further investigation will be based. They are summarized in Table 7.2.

7.2.2 Coplanar diffraction: influence of strain

In order to obtain detailed information also about the vertical strain component and its spatial distribution we mapped the whole two-dimensional diffraction pattern in symmetrical and asymmetrical coplanar diffraction geometry. The experiments around the 004- and the 224-reciprocal lattice point were performed at the D23 beamline of the synchrotron at LURE, Orsay, with a Si-111 monochromator and a Ge-111 an-

t_{lay}	D_{SG}	t_{SG}	b	g	p_r/p_l
$99 \pm 1 \text{ nm}$	$390 \pm 2 \text{ nm}$	$99 \pm 1 \text{ nm}$	$65 \pm 3 \text{ nm}$	$120 \pm 3 \text{ nm}$	≈ 1

Table 7.2: Geometrical parameters of the trapezoidal grating sample, extracted from the preliminary grazing incidence diffraction analysis. From left to right: layer thickness, lateral grating periodicity, grating height (etching depth), grating top width, groove width and grating sidewall slopes. [BLG99b, BL99]

alyzer. Narrow slits were employed to limit the extension of the monochromator streak and the analyzer streak in the diffraction pattern. A wavelength of $\lambda = 1.54 \text{ \AA}$ was used.

The experimental reciprocal space map recorded around the reciprocal lattice point 004 (top row of Fig. 7.4, on page 75) shows two main peaks, the substrate peak at $Q_z = 4.282 \text{ \AA}^{-1}$, and the layer peak which now lies below, since the layer material has a *larger* bulk lattice parameter than the substrate. Both are surrounded by a series of lateral satellites. For the layer peak this was to be expected, since the sequence of grating truncation rods is the reciprocal space equivalent of the lateral grating periodicity in real space. For the substrate peak, on the other hand, the presence of lateral satellites is more surprising. The SEM images as well as the GID investigation have shown that the grating height is equal to the layer thickness, i.e. the etching process has stopped at the layer-substrate interface and has not affected the substrate. Since a lateral modulation of the morphology can ruled out, these side peaks indicate a periodic modulation of vertical *strain* in the substrate, which is induced by the strain relaxation in the grating and has the same lateral periodicity. We thus find once again a pure “strain grating”, just like in the buried sample of Chapter 6, but now induced in the planar substrate *below* the etched structure. From the intensity and the vertical widths of the grating rods we conclude that the measurable vertical extension of the lateral strain modulation in the substrate is of the same magnitude as the surface grating height above it.

The diffraction pattern around the layer peak also shows interesting effects: The cross pattern which was to be expected theoretically is not complete; rather, the two lower branches have almost completely disappeared. In this respect, the picture shows the same tendency as observed in the previous Chapter already. However, the deformation is even more pronounced here: For the peaks within the two upper branches, further deviations from the ideal cross can be noticed. The main maxima of the grating truncation rods do not lie on two straight lines that go through the layer RLP, but the inner three grating order maxima remain on the same Q_z -height. Only from about the fourth order onwards they start to bend upwards. The overall form is somewhat reminiscent of a saucer. Since both the SEM images and the GID investigation gave evidence for a relatively perfect trapezoidal shape, this deformation cannot be due to the grating shape. In fact, the observed deformation of the diffraction pattern is a proof of a strongly non-uniform strain relaxation in this grating.

The 224-map in the top row of Fig. 7.5, though less well resolved along the Q_x -direction due to the instrumental resolution function, shows the same overall effects. The substrate peak is surrounded by a large cloud of lateral satellites, giving evidence for a laterally periodic lateral *and* vertical strain field induced in the substrate. The GTR maxima around the layer peak, on the other hand, are now arranged on a straight line, which may be interpreted as the upper left and lower right branches of a cross pattern. Once again, this disappearance of single branches must be due to a non-homogeneous relaxation in the grating. The same qualitative effects are found in both the symmetrical and the asymmetrical coplanar reciprocal space maps.

7.2.3 Numerical simulation and fit

In order to interpret these findings, we apply a simulation procedure similar to the one presented in the previous Chapter. Apart from reproducing the experimentally observed effects in the corresponding calculated diffraction maps, it is desirable to get a more intuitive “feeling” for the mechanism of distortion of the diffraction pattern, and to see how it gradually arises with increasing mismatch between the two materials. In other words, our aim is now to determine the actual lattice deformation in our sample by comparing measurements and calculated diffraction maps as a function of the actual grating set-up.

To this end, we incorporate an additional feature into our simulation procedure: an automatic fit loop over parameters such as the layer material composition x , or over geometrical parameters like the grating height. This project demands additional programming effort. In order to calculate a series of reciprocal space maps, for instance for different sample compositions x , the following tasks must be automatized:

1. The lattice parameters and the cubic elastic constants C_{11} , C_{12} and C_{44} must be interpolated via Vegard's law, and the "engineering version" of the elastic constants calculated for the [110]-frame of reference (see Appendix A).
2. The Finite Element program must be launched, instructed to create the grating geometry and to attribute the respective material properties to the substrate and the grating layer.
3. The solution must be calculated, and the results in terms of displacement and strain must be saved to files.
4. Then, the simulation program for the different reciprocal space maps must be started and needs to be provided with the filenames containing the latest strain results.
5. Finally, in order to visualize the results systematically, the simulated reciprocal space maps as well as the calculated strain fields must be automatically plotted and the plots saved to files.

We realized the different steps of this procedure by a combination of the C++ programming language, the ANSYS Finite Element program and the IDL visualization package, the contact between the different ingredients being established by a script written in the PERL programming language. The calculations were performed on the UNIX workstations at the ESRF.

It must be stressed here that the procedure described above is not a *fitting procedure* in the strict sense of the term, like for example the methods for non-linear least squares fitting described in [PTV95]. No mechanism is included which, after completing the simulation for one set of parameters, decides automatically which parameter to vary next, and in which direction. Due to the large number of free parameters and the complexity of their influence on the diffraction pattern, such an approach seemed bound to fail, either simply by being far too slow or by getting blocked in *local minima* in parameter space [PTV95].

It is more promising to vary different parameters systematically, to understand their influence on the diffraction pattern, and then to achieve a "best fit" by hand. This approach does not guarantee that the final result is the best of all possible results, but under certain conditions it can lead to a very good agreement between measured and calculated maps. Therefore, we adopted the strategy to have the program calculate systematically a series of reciprocal space maps with a constant step width of one parameter.

Fig. 7.3 shows the results for a series of material compositions $\text{Ga}_x\text{In}_{1-x}\text{As}$, with x ranging from 32 % (top row, strong compressive strain in the grating) to 52 % (bottom row, moderate tensile strain). The image in the fifth row ($x = 48$ %) is very close to the ideal cross-shaped pattern of a strain-free homoepitaxial grating: In fact, its composition is near the lattice-matched case of $x \approx 47$ %.

In this series of 004-maps, two general effects can be observed. First, the layer peak moves further and further away from the substrate peak as the lattice mismatch between the two materials increases. In the symmetrical maps (left column), this happens along a vertical line, while in the asymmetrical maps (central column), the same movement takes place in both the vertical and the lateral direction. Second, the diffraction pattern surrounding the layer becomes the more the further the two lattice parameters deviate from one another. When studying the maps from the fourth row up to the first row of Fig. 7.3 (in the direction of increasing compressive strain in the layer) we observe the following: In the fourth row, the cross pattern is still well observable, while in the third row the lower branches are already strongly suppressed. In the second row, the remaining upper branches are very noticeably deformed, and in the image in the first row, they reach a perfectly horizontal slope.

The corresponding maps for *tensile* strain in the grating ($x > 0.47$) show the same effects in the opposite direction: In fact, these maps are nearly mirror images of the ones calculated for compressive strain. Therefore, they are not shown systematically in Fig. 7.3; only the one for $x = 0.52$ is reproduced in the bottom row to indicate the general tendency.

A remark of more general nature is due here: The horizontal slope of the branches in the first row of Fig. 7.3 shows the danger that lies in immediate, non-quantitative interpretations of such reciprocal space

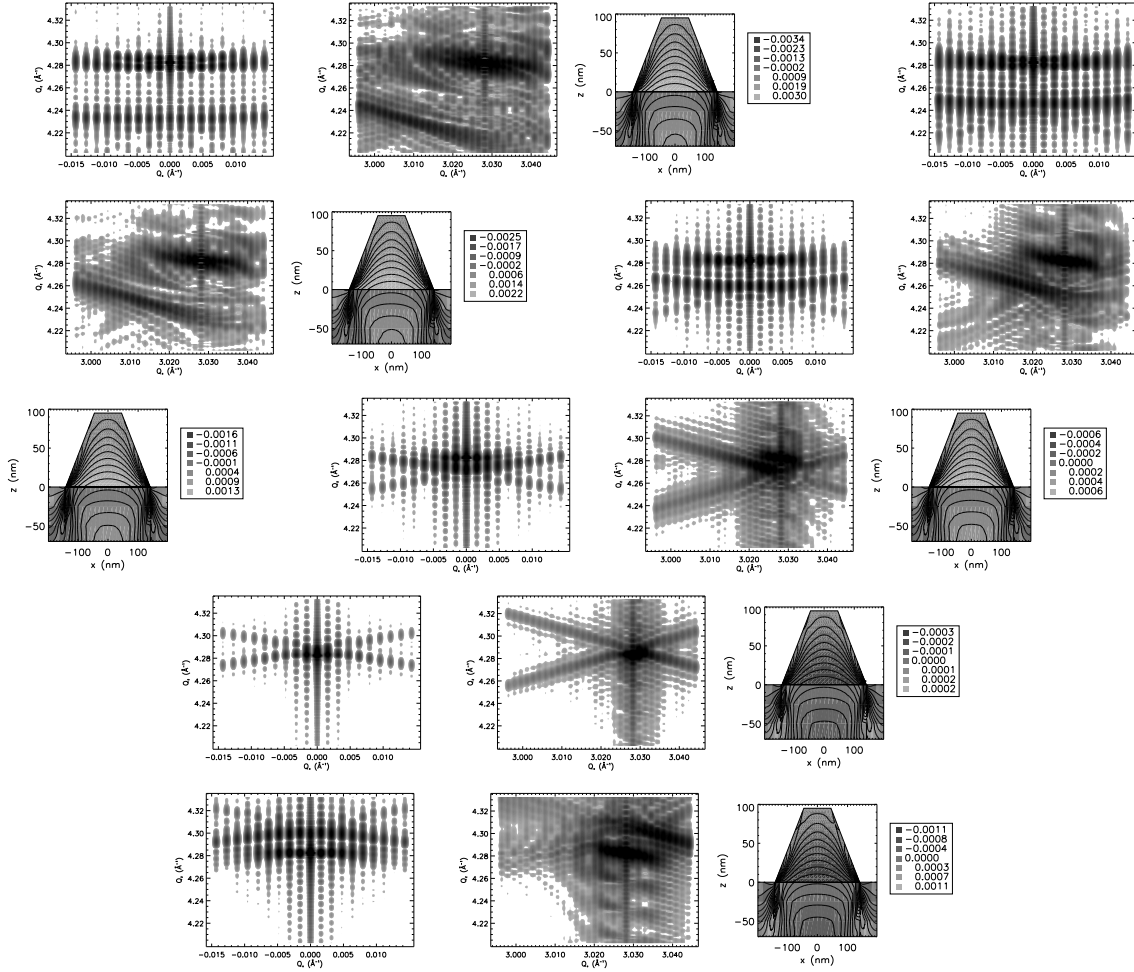


Figure 7.3: Numerical fit of the 004- and 224-reciprocal space maps from a trapezoidal grating: calculated map for various material compositions $\text{Ga}_x\text{In}_{1-x}\text{As}$, with x ranging from 32 % (top) to 52 % (bottom) in steps of $\Delta x = 4 \%$. The vertical component of the respective strain fields is also shown in the right column. A complete lattice matching with the InP substrate would be reached for $x \approx 47\%$ (close to the fifth row in our figure). Note that the gray scales for the strain images are optimized for each case individually, and are not comparable between different images. Thus, an apparently similar form of the contour lines in two images does not indicate that the absolute values of strain are comparable. In this figure, the focus is on the general evolution of the diffraction patterns; details like axis labels are to be neglected.

maps. If a similar map was measured experimentally, one might be tempted to misinterpret it as a “typical diffraction pattern of a *rectangular* grating” — an interpretation which would represent not only a small quantitative error, but a real *qualitative* mistake. We conclude that it is indispensable to perform extensive simulations before drawing quantitative or even qualitative conclusions from the experimental findings.

The final result of our evaluation procedure is shown in Fig. 7.4 for the symmetrical map, and in Fig. 7.5 for the asymmetrical map. For direct comparison, the top row shows the experimental maps, while the middle row shows the simulated ones. In the third row the vertical (left) and lateral (right) components of the best fit for the strain field are shown. The best agreement was obtained for a composition of $x = 0.395 \pm 0.005$, which is very close to the nominal value of $x = 0.40$.

The vertical strain in the layer has its positive maximum near the grating substrate interface; this corresponds to the maximum negative (compressive) lateral strain in the same region. Both components are

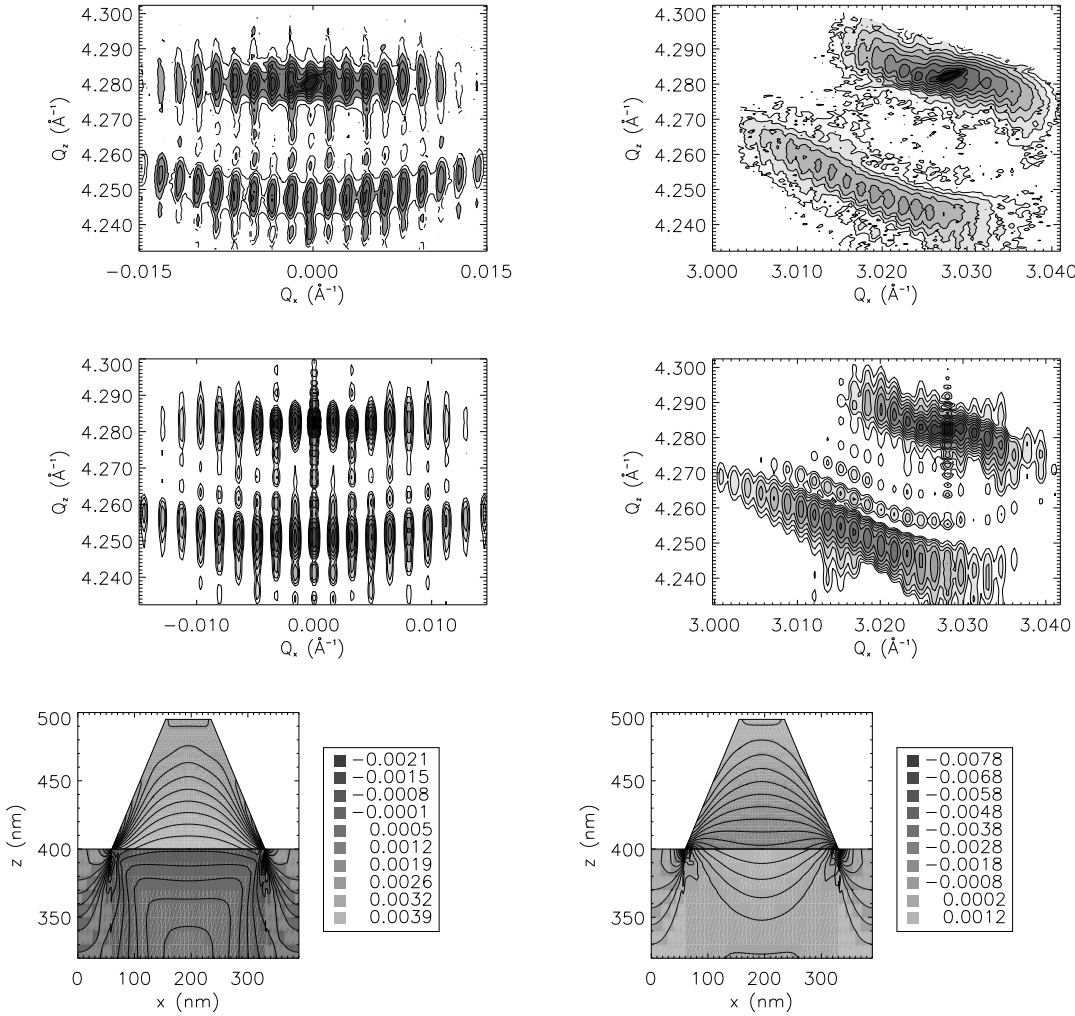


Figure 7.4: Symmetrical diffraction from strained-layer surface grating: Experimental map (top), best numerical fit (center), and the corresponding vertical component ϵ_{zz} of the strain field on which the calculation is based (bottom).

Figure 7.5: Asymmetrical diffraction from a strained-layer surface grating: Experimental map (top), best numerical fit (center), and the corresponding lateral component ϵ_{xx} of the strain field on which the calculation is based (bottom).

increasingly relaxed towards the grating top and sidewalls, and reach their values expected for the case of complete orthorhombic relaxation (i.e. a vertical misfit of $6.65 \cdot 10^{-3}$ and a lateral misfit of $4.46 \cdot 10^{-3}$) close to the grating surface. Due to the non-uniform strain relaxation in the substrate, a strain field of similar amplitude and vertical extension is induced in the substrate.

The comparison of the reciprocal space maps calculated from these strain fields with the experimental results shows that the strain relaxation can indeed account for the experimentally observed distortion of the diffraction pattern. The agreement of both maps is very satisfactory, since all essential features of the experimental maps were reproduced in the simulation. A sequence of lateral satellites is generated around the substrate peak, both in the symmetrical and in the asymmetrical simulated map, and the ideal layer cross-pattern is strongly deformed, with only the upper two branches (Fig. 7.4) or the upper left and lower right branch (Fig. 7.5) remaining. Not only maxima around the layer and substrate peak coincide with

the measurement, but also the series of intermediate thickness fringes show remarkable similarity with the experimental data.

7.3 Rectangular grating

7.3.1 Experimental results

The experimental reciprocal space maps of the second sample, the grating with nearly rectangular shape, are shown in the top row of Figs. 7.7 and 7.8 (on page 78). As in Fig. 7.4, both maps show once again two main groups of peaks, one around the InP-004 Bragg peak at $Q_z = 4.282 \text{ \AA}^{-1}$, and one around the layer peak below it.

The substrate Bragg peak is once again surrounded by a series of equidistant lateral satellites. We conclude that, just like in the case of the trapezoidal sample, a laterally periodic “strain grating” is induced in the substrate also for the rectangular grating. On the other hand, the group of lateral grating maxima at the height of the layer peak does less obviously deviate from the ideal pattern. For a rectangular grating shape the upper and lower branches of the cross coincide, and a purely horizontal diffraction pattern is to be expected. In the experimental map of the symmetrical reflection, both the main maxima on the grating truncation rods and the thickness fringes above and below them do follow this horizontal slope. In the asymmetrical reciprocal space map, however, a distortion can be observed. Although the single grating truncation rods are not well separated due to the different instrumental resolution function at this reflection, it is obvious that the envelope of the intensity distribution around both peaks follows an inclined direction, from the upper left to the lower right. This inclination is an indication for a non-homogeneous strain relaxation also in the rectangular grating.

7.3.2 Numerical simulation and fit

In order to gain a deeper understanding of the details of the strain field in the sample we applied our systematic simulation procedure based on the principles presented in Section 7.2. Once again, a loop over the material composition was performed. The details are not shown here, since the results are similar to those obtained for the trapezoidal grating, in terms of overall shift of the layer peak with respect to the substrate peak. However, the deformation effect is less drastic, and the pattern around the layer peak remains essentially horizontal for a large range of compositions.

Another kind of parameter loop is more interesting in the present context: Fig. 7.6 shows the results of a systematic variation of the grating shape, more specifically of the width of the lower part of the grating. From top to bottom in Fig. 7.6, the slope of the grating sidewall with its kink in the middle changes from concave to convex. The effect on the reciprocal space maps is shown in the left columns of the same figure. While the appearance of the pattern around the substrate peak is relatively constant, the pattern around the layer peak changes. There is one strong branch of peaks along a nearly horizontal line. This group of maxima obviously stems from the upper two thirds of the grating, whose sidewall slope changes less drastically than the one in the lower third. The lower part, in turn, gives rise to a weaker second branch in the diffraction pattern, whose inclination changes from upwards (top row) to downwards (bottom row) and thereby reproduces the corresponding change of inclination of the grating sidewalls.

The final results of the fitting procedure are shown in Fig. 7.7 for the 004-map, and in Fig. 7.8 for the 224-map. We see that the strain field induced in the substrate can indeed account for the generation of lateral satellites around the substrate peak in both the symmetrical and the asymmetrical reciprocal space map. In the asymmetric case, the inclination of the group of maxima around the layer peak is very well reproduced. This proves that our description of the strain field also in the grating region is quantitatively correct.

Remaining differences are partly due to the instrumental resolution function, which has been taken into account only very approximately for the calculation (see in particular the analyzer streak around the substrate peak in the experimental maps). Furthermore, no attempt has been made to include the diffuse scattering which is visible in the experimental maps into the calculation. It may be due to roughness of the grating surface and sidewalls, to non-homogeneities of the grating shape over the sample surface, and to

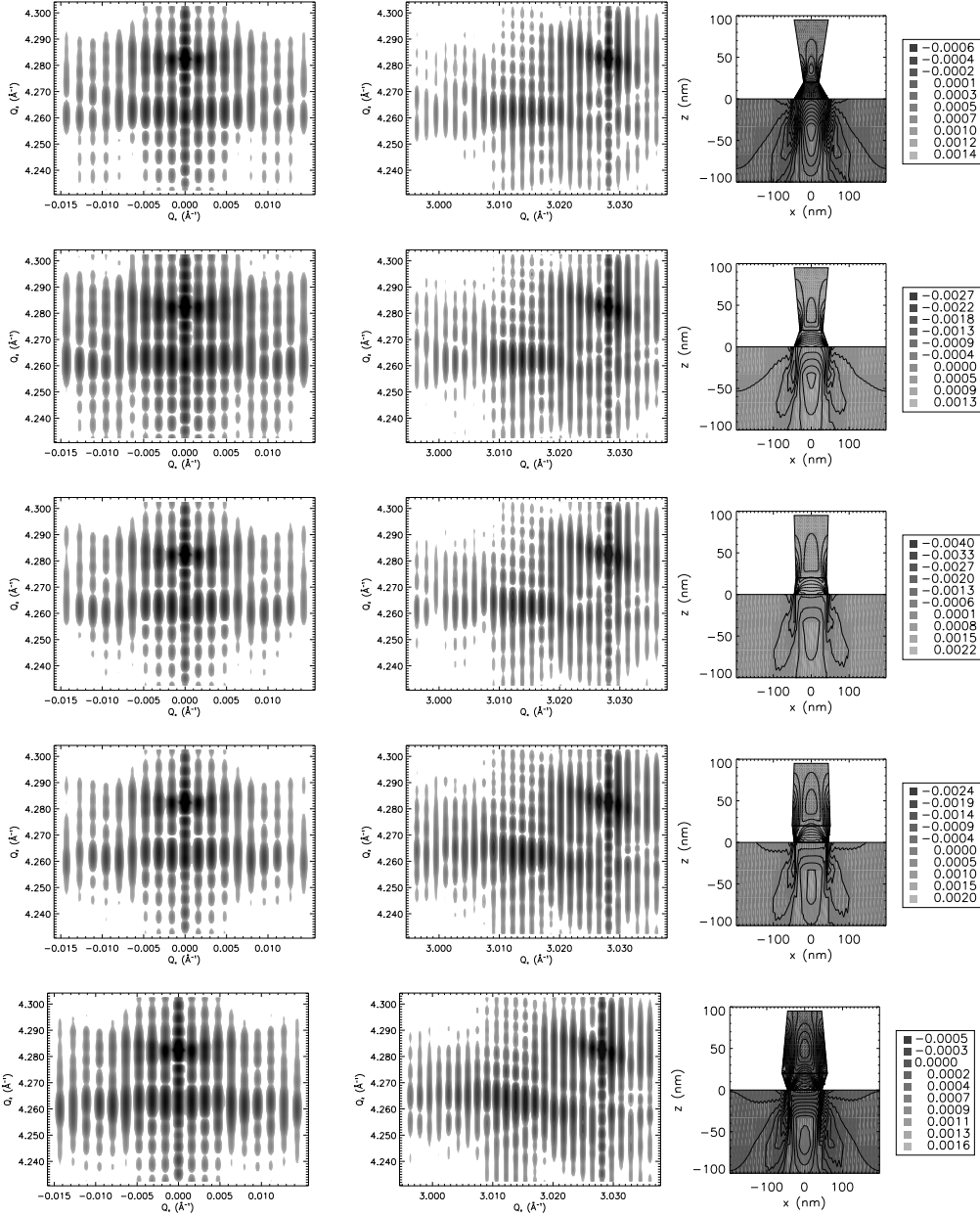


Figure 7.6: Numerical fit of the 004- and the 224- reciprocal space map from a strained grating: calculated map for various shapes of the grating. The width in the middle of the grating varies from 40 nm (top row) to 120 nm (bottom row) in steps of 20 nm. The vertical component of the respective strain fields is also shown on the right. Once again, the focus lies on the general evolution of the diffraction pattern.

resulting strain fluctuations. Nevertheless, the overall agreement is very satisfactory. In both maps not only the diffraction patterns around the substrate and layer peaks, but also the intermediate thickness fringes resemble closely the experimental data.

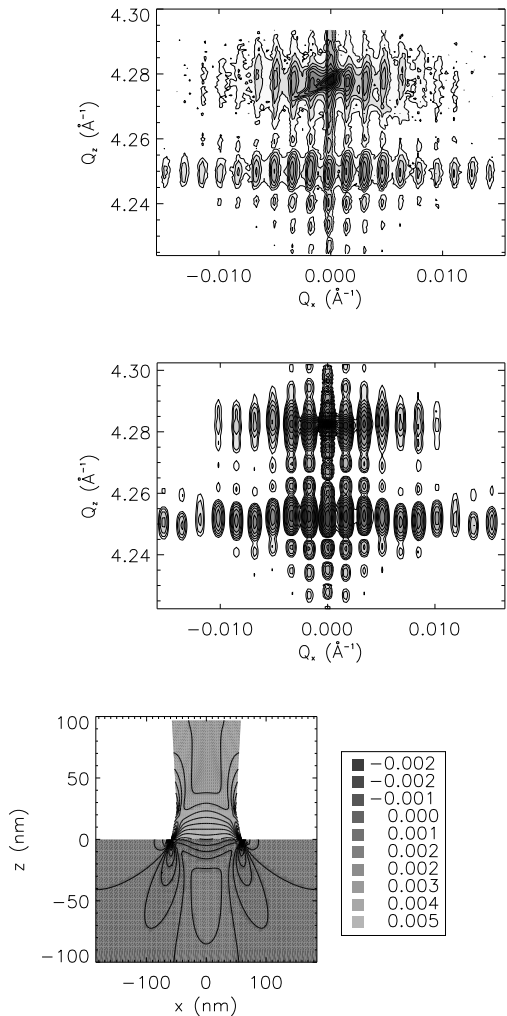


Figure 7.7: Symmetrical diffraction from a rectangular strained-layer grating: Experimental map (top), best numerical fit (center), and the corresponding vertical component ϵ_{zz} of the strain field on which the calculation is based (bottom).

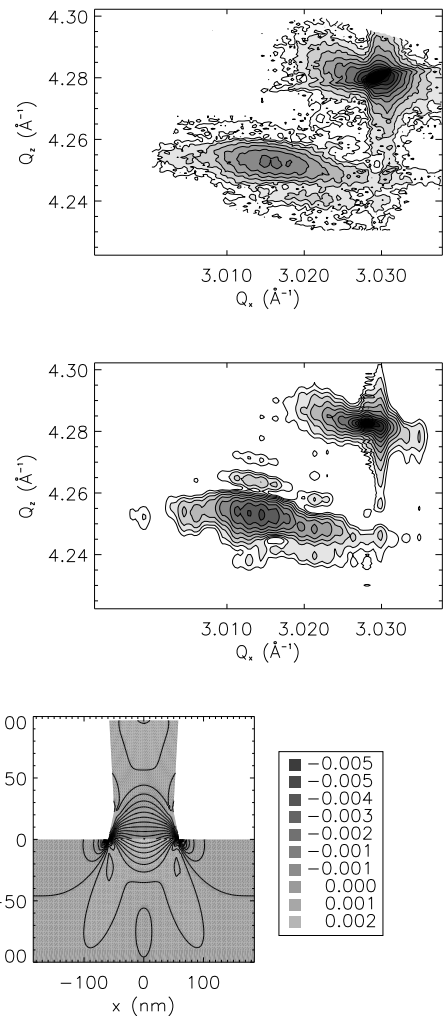


Figure 7.8: Asymmetrical diffraction from a rectangular strained-layer surface grating: Experimental map (top), best numerical fit (center), and the corresponding lateral component ϵ_{xx} of the strain field on which the calculation is based (bottom).

7.4 Conclusion

This Chapter has demonstrated our method for grating strain investigation on two more strongly, now compressively strained gratings. As before we were able to analyze the grating shape and the lateral strain relaxation (independently) by GID measurements, and to additionally enlighten the vertical strain components via coplanar XRD. Due to the stronger lattice distortions, the change in the diffraction pattern was even more drastic.

For the trapezoidal grating we found a strongly non-uniform strain field in the grating region. A laterally periodic strain field of similar strength and extension was induced in the substrate below the grating. For the rectangular grating we could similarly observe deviations from the diffraction pattern to be expected for non-strained samples, even though they were not as characteristic as for the trapezoidal grating. Nev-

ertheless, the data evaluation allows to draw similar conclusions as for the trapezoidal sample: The grating is non-uniformly distorted, and the substrate is affected in the opposite sense.

The procedure for simulation of reciprocal space maps was turned into a real quantitative one by additionally introducing a simulation *loop* over material composition as well as over the sample geometry. The calculated strain field can account for the effects observed in the experimental diffraction patterns. Very good agreement is achieved. We observed that the diffraction patterns are highly sensitive to changes in the material compositions, due to the resulting changes in lattice mismatch between the different layers and the related changes in strain fields. The sensitivity to details of the grating shape was found to be slightly less pronounced.

Chapter 8

Superlattice gratings

In Chapters 6 and 7 we have studied the effects of strain relaxation in two different examples of gratings etched into a single strained layer. The present Chapter extends our method of strain investigation to a more complicated sample type: a superlattice, i.e. a sample whose vertical compositional setup is characterized by a periodically alternating sequence of two or more different materials. The lateral structure is of the same kind as before.

Superlattices are particularly interesting for technological purposes, mainly for two reasons. First, they can be used as high-efficiency reflecting structures (so-called distributed Bragg reflectors, or DBR) in a vertically emitting semiconductor laser [Cor98]. They replace the traditional mirrors and selectively reflect only those wavelengths which are compatible with the superlattice period. Second, they show new “physics”, i.e. new effects in the electronic band structure (mini-bands), which makes them attractive for device applications [Kel95].

A superlattice is also an especially interesting object in the context of strain investigations. As in the case of a simple grating, the planar strained layers are tetragonally distorted during the growth phase, and become partially free to relax after the etching. But unlike before, there is not only one single interface between the two materials, but a whole series of interfaces with the corresponding boundary conditions. Each individual layer is thus constrained not only from below, but — to a certain extent — from both sides.

8.1 Introduction. The sample

We study the strain relaxation in superlattices (SLs) with the example of a $\text{Ga}_x\text{In}_{1-x}\text{As}/\text{InP}$ multilayer grown on an InP (001) substrate by chemical beam epitaxy. The nominal composition of the ternary layers was $x = 0.44$, which leads to a lattice parameter of $a = 5.880 \text{ \AA}$ and thus a tetragonal strain in the planar $\text{Ga}_x\text{In}_{1-x}\text{As}$ layers of $\epsilon_{xx} = -1.93 \cdot 10^{-3}$ (where the negative sign once again indicates compressive strain in the layer). The superlattice consists of four and a half periods, i.e. nine layers, starting and ending with $\text{Ga}_x\text{In}_{1-x}\text{As}$. The nominal thicknesses of the single $\text{Ga}_x\text{In}_{1-x}\text{As}$ and InP layers in the SL period were 30 nm and 50 nm, respectively. This leads to a net misfit of the averaged multilayer with respect to the substrate of $\epsilon_{xx}^- = -0.72 \cdot 10^{-3}$.

x	a	$\epsilon_{ }$	ϵ_{zz}^0	$\epsilon_{xx}^{\text{ortho}}$	$\epsilon_{zz}^{\text{ortho}}$
0.44	5.8802 \AA	$-1.931 \cdot 10^{-3}$	$+1.914 \cdot 10^{-3}$	$+2.70 \cdot 10^{-5}$	$+9.44 \cdot 10^{-4}$

Table 8.1: Values of strain in the gratings, as predicted from the nominal composition for the two limiting cases of complete lattice matching (tetragonal strain) and full relaxation (orthorhombic strain). From left to right: compositions of the layer material $\text{Ga}_x\text{In}_{1-x}\text{As}$; lattice parameter; lattice mismatch with InP substrate $\epsilon_{||}$ and resulting tetragonal vertical strain ϵ_{zz}^0 ; lateral and vertical orthorhombic strain $\epsilon_{xx}^{\text{ortho}}$, $\epsilon_{zz}^{\text{ortho}}$ (see eqs. (5.33) - (5.35)).

The compositional profile of the planar structure was verified experimentally by double-crystal X-ray diffraction with a conventional sealed tube. The rocking curves could be fitted with a model based on thicknesses of 27.5 nm for the $\text{Ga}_x\text{In}_{1-x}\text{As}$ layer and a total superlattice period of $D_{\text{SL}} = 76.2 \text{ nm}$ [BLG00], slightly less than the intended value of 80 nm.

A laterally periodic pattern was produced on the sample surface by holographic lithography and subsequent etching with a solution of Br_2 in CH_3OH . Just like in the case of simple gratings (see Chapter 7), different grating shapes can be obtained for different crystallographic orientations of the etching mask. In the present Chapter a sample patterned along the [110]-direction with a resulting trapezoidal grating shape shall be studied.

In Fig. 8.1 we show two microscopic images of the sample, recorded at different positions on the sample surface. On top of the grating structure parts of the photo-resist used for the lithography process are still visible. Apart from this, a relatively perfect trapezoidal grating shape can be recognized. However, the shape varies slightly between the two images: the grating top width, for instance, is larger in the right picture. It must be left to the X-ray characterization to determine *representative*, statistically averaged values for the geometrical parameters.

Fig. 8.2 shows schematically the geometry of the sample. The corresponding reciprocal space structure is visible in Fig. 8.3. It shows a 004-map simulated for the hypothetical case of a superlattice grating without any strain. “Without strain” means that an imaginary, infinitely thin vacuum layer is inserted at each interface to prevent the contact between the two adjacent materials. No adaptation of lateral lattice parameters occurs, and each individual layer can relax completely. With this model calculation we can isolate the influence of the pure grating *shape* on the diffraction pattern.

In the image we see a series of vertical satellites along the grating truncation rod, which is due to the compositional periodicity of the superlattice. Their spacing in reciprocal space is related via $2\pi/D_{\text{SL}}$ to the superlattice period. Each superlattice satellite is surrounded by a cross pattern, which is characteristic for the trapezoidal grating shape. This is completely analogous to the case of the simple gratings studied before, except that the cross occurs not only once, but is now replicated around each of the superlattice satellites. This image represents the ideal diffraction pattern of a non-distorted sample. Deviations of the experimental data from this ideal pattern will represent evidence of strain relaxation in the real sample.

X-ray diffraction experiments on this sample were performed at two facilities:

- the undulator beamline BW2 at HASYLAB, Hamburg, with a Si-111 double crystal monochromator selecting a wavelength of $\lambda=1.181 \text{ \AA}$, a Si-111 analyzer crystal to obtain high resolution in the $Q_x Q_y$ -plane, and narrow slits to achieve a moderate resolution also along Q_z ($\Delta Q_z \approx 0.005 \text{ \AA}^{-1}$);
- the beamline D23 of LURE, Orsay, with a Si-111 double crystal monochromator selecting a wavelength of $\lambda=1.54 \text{ \AA}$, a Ge-111 channel-cut analyzer and narrow detector slits to limit the extension of the analyzer streak in the coplanar reciprocal space maps.

The wavelengths chosen were 1.181 Å for grazing incidence diffraction at BW2, and 1.54 Å for coplanar diffraction at D23.

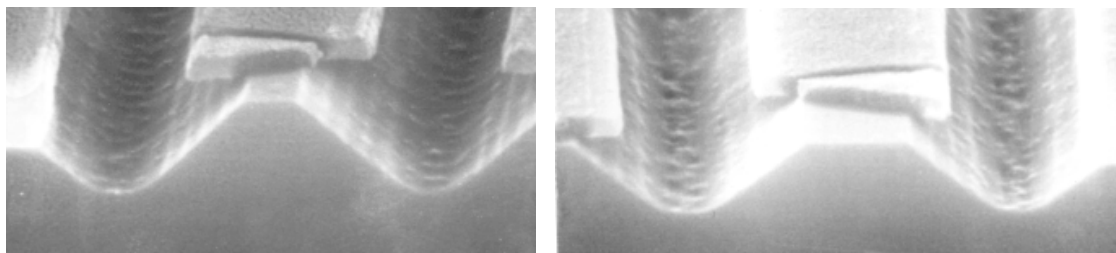


Figure 8.1: SEM images of the sample studied in this Chapter, recorded at two different spots on the sample surface. [BLG00]

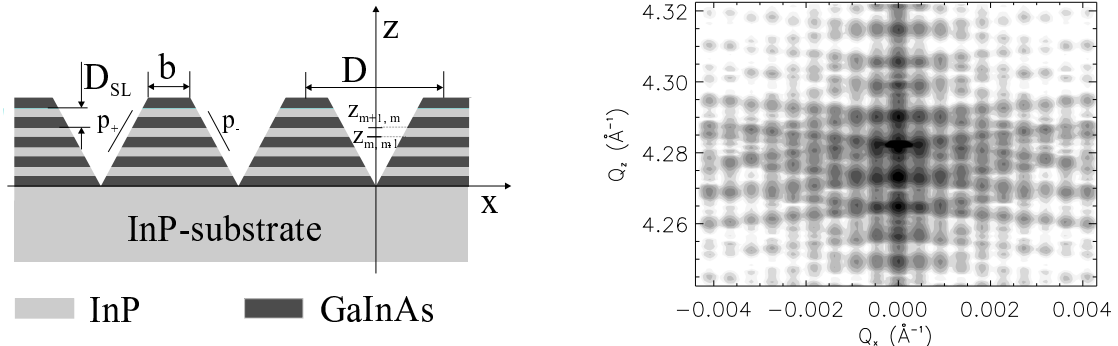


Figure 8.2: Geometry of a superlattice grating in real space. D is the lateral (grating) period, D_{SL} the vertical (superlattice) period, b the grating top width and $p_{l/r}$ the sidewall slopes. [BLG00]

Figure 8.3: Structure of the sample in reciprocal space: Simulation of a diffraction map for the hypothetical case without strain. The image shows the pure influence of the grating shape on the diffraction pattern: The periodical layer setup in real space leads to a series of satellites along the vertical direction in reciprocal space.

8.2 Symmetrical and asymmetrical diffraction

In order to investigate experimentally the grating shape of our sample, independently from any strain consideration, we performed an initial study by grazing incidence diffraction. Detailed results can be found in [BLG00]; the values of the geometrical parameters deduced from this study are summarized in Table 8.2.

t_{InP}	t_{GaInAs}	D	t_{SG}	b	g	p_l	p_r
47.2 ± 5	28.5 ± 2	1380 ± 5	70 ± 1	485 ± 15	5 ± 10	6.3 ± 0.3	6.3 ± 0.3

Table 8.2: Geometrical parameters of the superlattice grating, as obtained from the evaluation of grazing incidence diffraction. t_{InP} and $t_{\text{Ga}_x\text{In}_{1-x}\text{As}}$ are the layer thicknesses, D is the lateral grating period, t_{SG} the etching depth, b the grating top width, g the groove width, and p_l and p_r sidewall slopes (as before). All lengths are given in units of nm.

To detect the additional influence of lateral strain in the grating we recorded coplanar diffraction maps at the 002- and the 224-reflection. The 002-peak was preferred to the stronger 004-peak, although the latter has a higher strain-sensitivity. The reason were resolution considerations: Since the grating has a relatively large real-space period, the grating truncation rods are very close to each other in reciprocal space. In order to resolve them with a given angular resolution and angular step width of the instrument, it is advantageous to choose a reciprocal lattice point with short length $|\mathbf{h}|$.

In the experimental map (Fig. 8.6) we observe the substrate 002-peak at $Q_z = 2.141 \text{ \AA}^{-1}$, and a large number of strong superlattice satellites equidistantly distributed along the vertical direction. The substrate peak does not coincide with the zero-order superlattice satellite, but lies between the 0th and the +1st order peak. This is due to the fact that the average lattice parameter of the superlattice is larger than the one of InP.

The vertical satellites appear not only on the CTR, but similarly on each of the lateral grating truncation rods. Their position shifts upwards, towards higher Q_z , for increasing grating rod order: The satellites form bent branches. For some of these branches (especially the zeroth-order one), below the substrate

peak) one can observe a far weaker, but still noticeable “mirror” branch which is bent in the opposite direction. In other words, we find a feature which is very similar to the observations made in the previous Chapters: a cross pattern with a pronounced asymmetry between the upper and the lower branch. The relevant difference to the case of simple gratings is that the cross pattern is now replicated around each of the vertical superlattice satellites, and each cross is deformed individually. For higher vertical satellite orders the deformation is enhanced, and the lower branch disappears completely.

In order to investigate also the lateral component of the strain field we measured the diffraction pattern around the 224 Bragg peak, in the geometry of large incident angles and low exit angles (upper image in Fig. 8.7). Due to the different resolution function at this reflection, the single grating truncation rods are not well separated in the experimental map; only the intensity envelope could be measured. The envelope is sufficient, however, to recognize two important things: There is once again a series of vertical superlattice satellites, and the cross pattern around each of them is strongly deformed. The combined influence of vertical *and* lateral strain on the asymmetrical diffraction pattern results in diagonal lines of strong intensity around each superlattice satellite. These lines can be interpreted as the remaining upper left and lower right branches of the theoretical cross pattern. Upon closer examination, one can also notice that the center of mass of the vertical satellites is shifted to the left with respect to the substrate peak.

8.3 Theoretical calculation and fit of the results

In order to analyze the experimental findings we apply our evaluation procedure based on X-ray diffraction theory and elasticity theory. An elastic description of the strain field in a superlattice grating relies on the same basic equations as for simple gratings, but has to take into account additional constraints. The one-to-one correlation between atoms in adjacent layers (condition of pseudomorphic growth) must be preserved across each of the interfaces in the superlattice, in the same way as across the grating-substrate interface. Moreover, the stresses have to be continuous across all interfaces. This leads to a whole series of additional boundary conditions for the elastic calculation. To solve the complete set of differential equations and accompanying boundary conditions, we use once again a numerical solution by the Finite Element Method. Apart from the additional interface conditions, the principle is unaltered with respect to Chapter 7, but the task becomes more demanding from a computational point of view.

The resulting strain and displacement fields are then fed into our simulation program to calculate the corresponding reciprocal space maps. No explicit adaptation of the program to the new sample type is required: In our semi-kinematical formalism the single cells of the structure contribute independently to the total diffracted signal, so that for the calculation algorithm it makes no difference whether the layers consist of a homogeneous material, as in the previous Chapters, or whether they are compositionally modulated along the vertical direction.

To obtain the best agreement between experimental and simulated data we use the fitting possibility introduced in Chapter 7. The results for a fit loop over the Ga-content x in the $\text{Ga}_x\text{In}_{1-x}\text{As}$ layer are shown in Fig. 8.4. From top to bottom, x assumes the values 0.40, 0.44, 0.47, 0.50 and 0.54, so that the strain in the ternary layers varies from compressive ($\epsilon_{||} = -4.7 \cdot 10^{-3}$) to tensile ($\epsilon_{||} = 4.9 \cdot 10^{-3}$). The middle row is close to the lattice-matched case. Indeed, it shows a relatively perfect symmetrical cross pattern around each superlattice satellite. For increasing compressive strain (decreasing x) the lower branch of each single cross becomes weaker (image in the second row) and is finally completely suppressed (first row). For higher mismatch the upper branch of the cross is also affected: It does not remain straight, but becomes deformed in a way that reminds of the saucer-like shape observed in Chapter 7. For *tensile* strain in the layers ($x > 0.47$, fourth and fifth row in Fig. 8.4), very similar effects can be observed. The only difference is that it is now the upper branch of the cross which disappears.

The vertical component of the strain fields on which the calculations are based are shown in the right column of Fig. 8.4. When comparing the simulated maps and the corresponding strain fields, it is interesting to observe a correlation between two kinds of bending. In the first image, where the branches of the cross pattern are bent upwards, the interfaces visible in the strain image are curved downwards. In fact, all the diffracting lattice planes in the structure are concavely bent in a similar way. In the last image row, on the other hand, for which the cross pattern is strongly distorted downwards, the diffracting lattice planes are

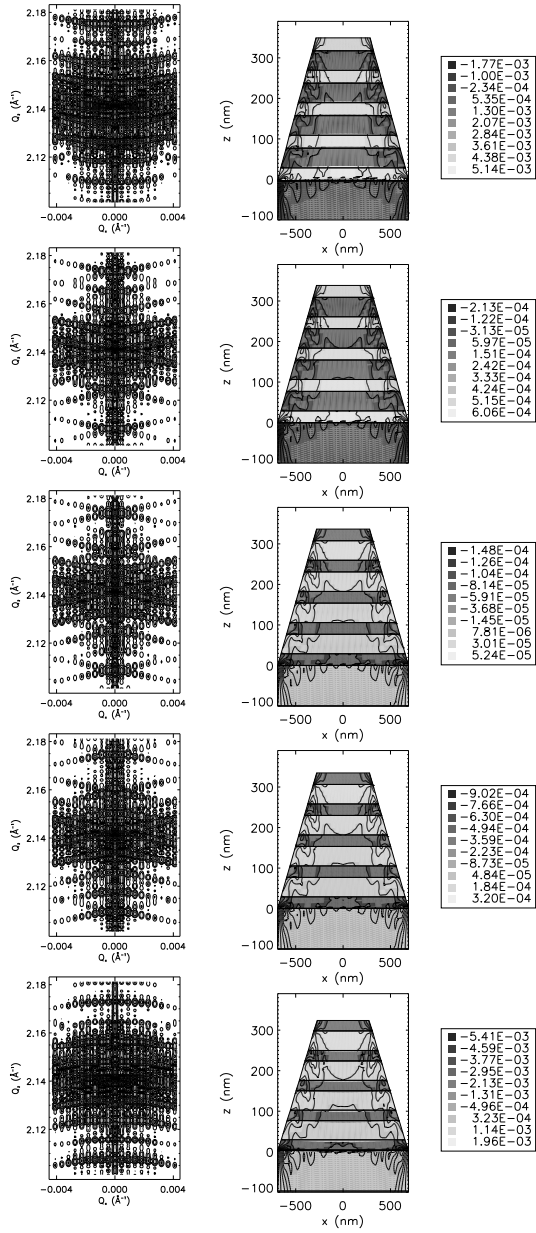


Figure 8.4: Fitting procedure: simulated 004-maps for various material compositions x of the $\text{Ga}_x\text{In}_{1-x}\text{As}$ layer. From top to bottom: $x = 0.40$, $x = 0.44$, $x = 0.47$, $x = 0.50$ and $x = 0.54$. The diffraction pattern at this reflection is influenced by the vertical strain component only, which is shown for comparison in the right column. The strain in the ternary layers varies from compressive to tensile. The middle row corresponds approximately to the lattice-matched case: the strain field shown on the right has much lower absolute values than in all other cases.

convexly bent. In this way the deformation of the planes of atoms in the crystal can yield an illustrative explanation for the observed deformation of the diffraction pattern.

In the corresponding series of simulated 224-maps (Fig. 8.5) we observe similar effects as in the symmetrical case: a series of vertical satellites. The pattern surrounding them is reduced to a simple cross shape for the lattice-matched case (middle row), but becomes strongly deformed for both compressive and tensile strain in the grating (second and fourth row). For even stronger absolute values of strain only one diagonal line of satellite maxima remains, which represents the upper left and lower right branch of the

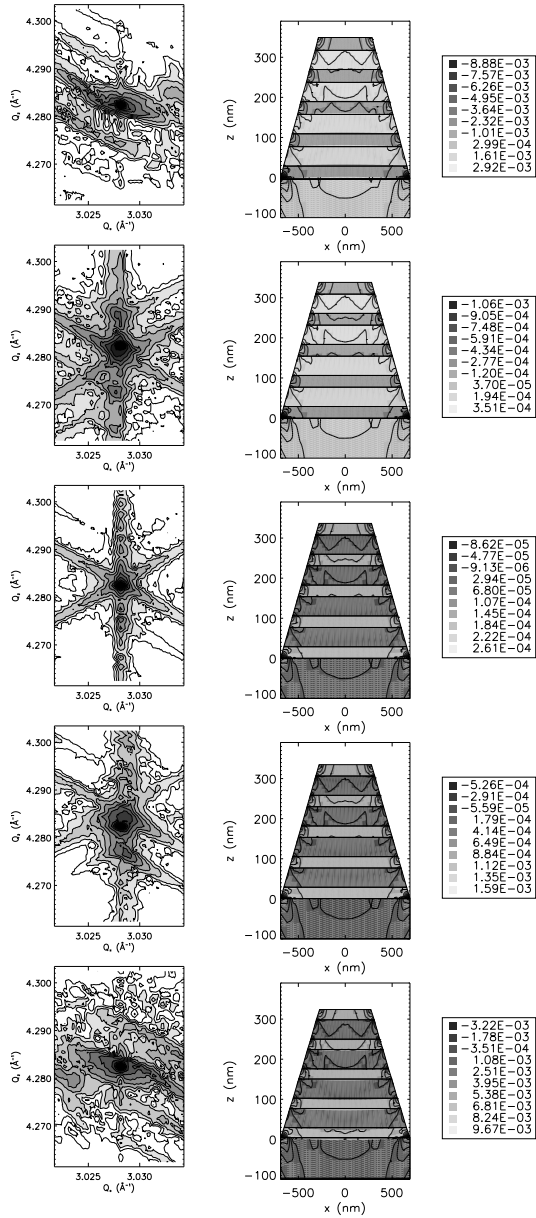


Figure 8.5: Fitting procedure: simulated 224-map for the same series of material compositions as in Fig. 8.4. The lateral strain component, to which this reflection is additionally sensitive, is given in the right column.

former cross pattern. Note that this is similar for both compressive strain (first row) and tensile strain (fifth row). There is a difference, however, between the two cases: In the image in the first row, the intensity envelope exhibits a net shift towards smaller Q_x , whereas in the fifth image it is shifted towards larger Q_x . This shift is an indication for a net relaxation of lateral strain in the whole grating, as we had concluded already when interpreting the experimental data.

The best fits of the coplanar reciprocal space maps are shown in Fig. 8.6 (for the 002-reflection) and Fig. 8.7 (for the 224-reflection). In both cases very good agreement is achieved. The relative intensity of most of the superlattice peaks is reproduced, as is the deformation of the cross patterns. Let us stress the fact that the same set of parameters and the same strain fields allow to fit both experimental maps simultaneously. Remaining differences may be due to variations in the grating shape and resulting strain

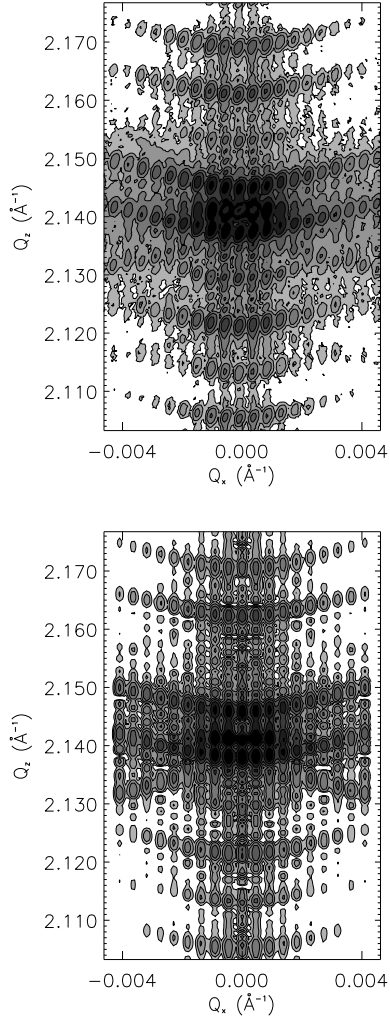


Figure 8.6: Symmetrical diffraction from a superlattice grating. Experimental (above) and fitted (below) reciprocal space map of the 002-reflection.

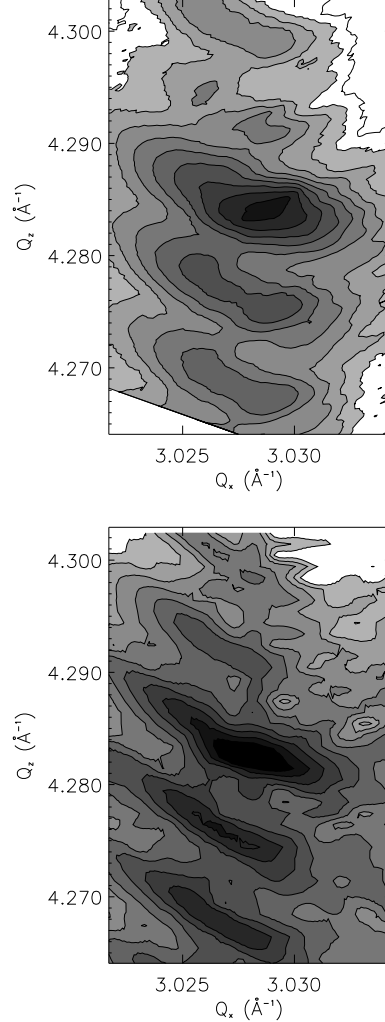


Figure 8.7: Asymmetrical diffraction from a superlattice grating. Experimental (above) and fitted (below) reciprocal space map of the 224-reflection.

fluctuations along the sample surface, and/or to roughness of the grating sidewalls induced by the etching process.

The strain field on which the calculation of the best-fit maps is based is shown in Fig. 8.8. Opposite strain behaviour can be observed in the two types of layers: a progressive relaxation of compressive strain in the $\text{Ga}_x\text{In}_{1-x}\text{As}$ layer with increasing distance from the substrate, and a related expansion (tensile strain) in the respective InP layers. The strongest relaxation takes place near the grating sidewalls, close to the free surface.

In order to generate a more immediate impression of the whole deformation field in the superlattice and its continuity across the interfaces, we plot not only the strain field, but also the two components of the displacement field \mathbf{u} (lower row in Fig. 8.8), more exactly its “relaxation” component $\Delta\mathbf{u}(\mathbf{r})$ (see eq. (5.31)). The lateral displacement u_x is obviously continuous across all the interfaces. This is precisely the boundary condition which we applied in the elastic calculation (one-to-one correlation of atoms adjacent in adjacent layers), and which is correctly preserved in our solution. Furthermore, u_x exhibits an oscil-

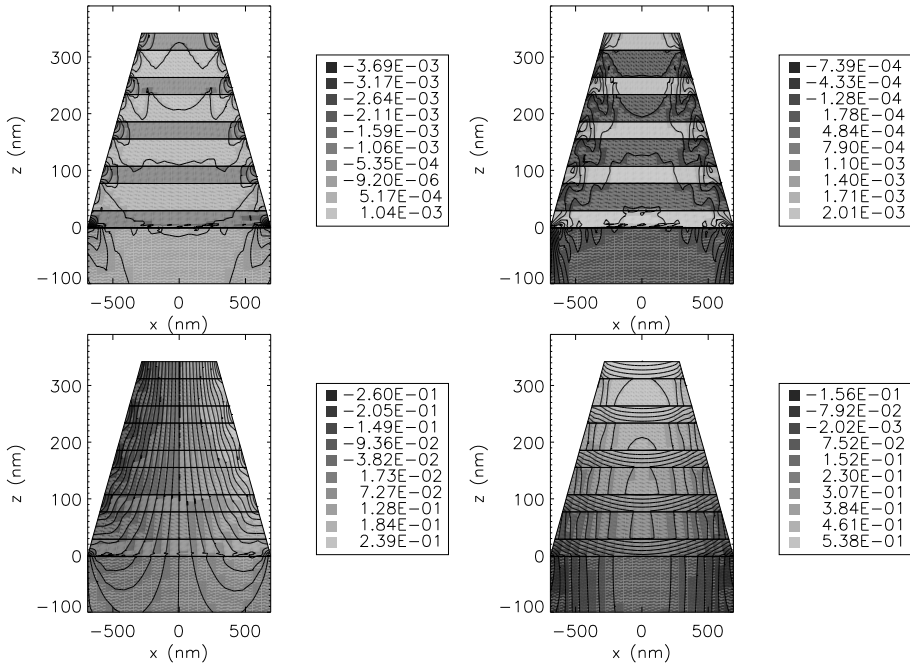


Figure 8.8: Final result of the fitting procedure: lateral component (left) and vertical component (right) of the strain field ϵ (top row) and of the displacement field \mathbf{u} (bottom row, in units of nm) in the superlattice grating.

lating behaviour which follows the compositional periodicity, especially near the sidewalls. The vertical displacement \mathbf{u}_z (lower right image in Fig. 8.8) is continuous across the interfaces as well, but can be seen to have a much stronger gradient in the strained ternary layers than in the InP layers. The derivative of the lateral displacement, the lateral strain ϵ_{xx} , is *not* continuous, because it is calculated with respect to different systems of reference, namely the bulk lattice of the two respective layers.

8.4 Conclusion

We have extended our method of strain investigation to a more complicated type of samples, namely superlattice gratings which are characterized by a periodic layer sequence (vertical compositional periodicity). In reciprocal space this gives rise to a set of superlattice satellites along the Q_z -direction. Each of these satellites on the crystal truncation rod is — in theory — surrounded laterally by the same kind of cross pattern as expected for a simple trapezoidal grating.

In the experimental coplanar reciprocal space maps we found strong deviations from this model. The deformation of the experimentally observed cross patterns could be interpreted as an indication for strain relaxation. The effects were successfully explained within the same evaluation formalism as presented in the previous Chapters. Our analysis method was transferred and applied without substantial changes to these more complicated samples. This demonstrates its flexibility.

The maps showed the influence onto the strain field in the superlattices of (a) the net mismatch between the different layers in the superlattice period, and of (b) the grating-substrate interface. The latter has an important influence on the relaxation of the net misfit in the multilayer towards the free surface. The compositional profile, on the other hand, manifests itself in the strain relaxation of the $\text{Ga}_x\text{In}_{1-x}\text{As}$ layers and in an opposite stress induced in the InP layers.

Chapter 9

Dynamic patterning by surface acoustic waves

The aim of this chapter is to show the applicability of our method of strain analysis to a different type of laterally periodic structures. We will study surface structures which show a highly regular lateral ordering, although they are not artificially structured via etching: dynamically formed “gratings” which are generated at the surface of crystalline substrates under the influence of piezoelectrically induced surface acoustic waves (SAW). X-ray diffraction from these acoustic gratings can be studied with an experimental approach similar to the one used in the previous chapters. The application of our simulation procedure to this new subject constitutes a test of the flexibility and robustness of the whole evaluation formalism, and simultaneously can contribute to a deeper understanding of surface acoustic waves as well as of the mechanism of X-ray diffraction from them.

9.1 Introduction

Surface acoustic waves in crystals have been studied in a series of articles by a variety of methods: neutron scattering [KPW67, HY99], X-ray diffractometry [Har67, ERS89, RBdB92, RB93, RTM98] and X-ray topography in a stroboscopic mode [WGT82, ZSS98, SSM99], and photoluminescence [ZPB97, SRJ98]. Their propagation has been investigated in superlattices [AT98], quantum wells [RZW97] and quantum dots [NBB99]. A first quantitative analysis of X-ray diffraction curves from acoustically excited GaAs crystals has appeared in the literature very recently [SSM99, Sau99].

One possible application of surface acoustic waves is to use them in order to “store” light (delay its propagation) in novel optoelectronic devices [RZW97]. The interest in these waves is partly also due to their potential application as X-ray optical elements. A surface acoustic wave corresponds to a laterally periodic deformation field in a crystal, which gives rise to lateral “grating” satellites that appear on the right and left side of the central X-ray diffraction peak at each single reciprocal lattice point. This is perfectly analogous to the grating truncation rods generated by the morphological periodicity in the case of etched gratings.

Surface acoustic waves can occur in two different forms: *travelling waves* or *standing waves*. In the former case the shape of the wave field remains constant in time and propagates along the crystal surface. In the latter case a spatially immobile wave field oscillates in time, with an amplitude that varies periodically between 0 and some maximum amplitude. Therefore the X-ray diffraction pattern from standing SAW varies periodically with the same frequency as the acoustic wave. This effect has been observed experimentally [RB93, RTM98]. Our experimental setup is expected to generate *standing* acoustic waves.

The application in X-ray optics relies on the use of acoustically excited crystals as monochromators or beam deviators. If one uses narrow slits to let pass for instance the first order lateral satellite beam only, and to block the intensity from the main Bragg peak, it is possible to switch this filtered beam on and off by altering the voltage applied to the piezoelectric transducer which generates the acoustic waves. In the case

of standing waves the diffracted intensity has a further property of interest: It is modulated in time with the same frequency as the acoustic wave field (in the MHz range) [RTM98].

By additionally varying the acoustic frequency and thus the wavelength of the deformation field one can gradually change the angular position of the satellite beam. Applications of this variant lie in the field of scanning X-ray imaging. The possible movement of the beam [TBR98] has been proposed as an attractive alternative to the classical method of mechanically displacing the sample with respect to the (fixed) beam [CDL95].

9.2 Experimental rocking curves

The experimental setup [Tuc99] is shown schematically in Fig. 9.1. An acoustic transducer, fabricated lithographically on the surface of a LiNbO_3 crystal, is fed by a radio-frequency signal ($f_0 \sim 10^8$ Hz). Since the SAW velocity is of the order of 3 km/s, wavelengths of some $10 \mu\text{m}$ are obtained. The acoustic wave field excited by the transducer is mainly concentrated at the sample surface. Its amplitude in the volume of the crystal is progressively damped for increasing depth below the surface, with a characteristic penetration depth of the same order of magnitude as the SAW wavelength (some $10 \mu\text{m}$).

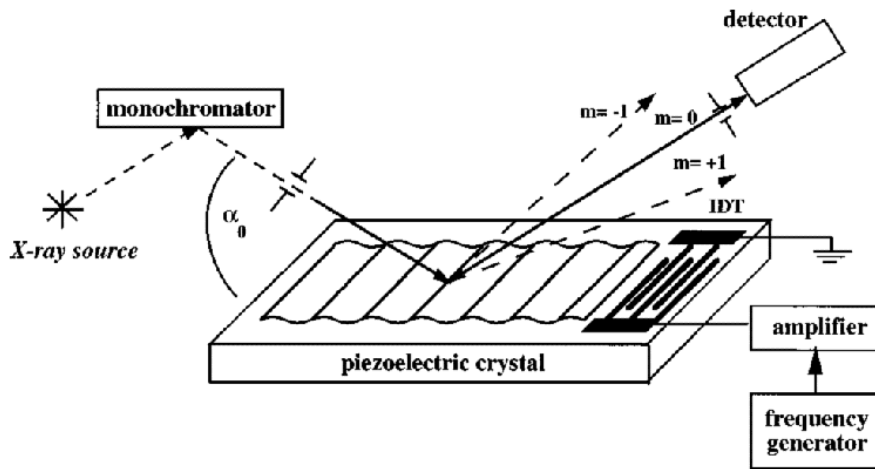


Figure 9.1: Schematic setup of the experiment: An acoustic wave field is generated at the surface of a LiNbO_3 crystal by a piezoelectric transducer (marked “IDT” in the image). The lateral periodicity of the surface acoustic wave field gives rise to a series of lateral satellites that appear around the central reflected or Bragg-diffracted X-ray beam. [TBR98]

The X-ray diffraction experiments were performed in the double-crystal mode at the beamline BM5 of the ESRF [Tuc99]. A wavelength of 1.54 \AA was used. Rocking curve profiles were recorded by rotating the sample across the Bragg peak of the 003-reflection. In the reciprocal space image this corresponds approximately to a Q_x -scan across the whole series of lateral satellite peaks. In fact, all the information is contained in this lateral direction. Unlike the case of etched gratings, no layer thickness or vertical grating shape is to be determined. Therefore we do not need to record the variation of diffracted intensity along the Q_z -direction.

This measurement was repeated for a series of voltages applied to the transducer, ranging from 0 mV to 150 mV. The amplitude of the wave excited in the crystal is expected to be roughly proportional to the voltage, with a proportionality constant of about 0.1 \AA/mV [Tuc99]. However, this correlation is subject to considerable experimental uncertainty; the details of the exact relationship remain to be verified.

The experimental results, converted to a reciprocal space scale, are plotted in Fig. 9.2 for selected voltages. The lowest curve (0 mV) corresponds to the rocking curve of a simple bulk crystal; it shows one

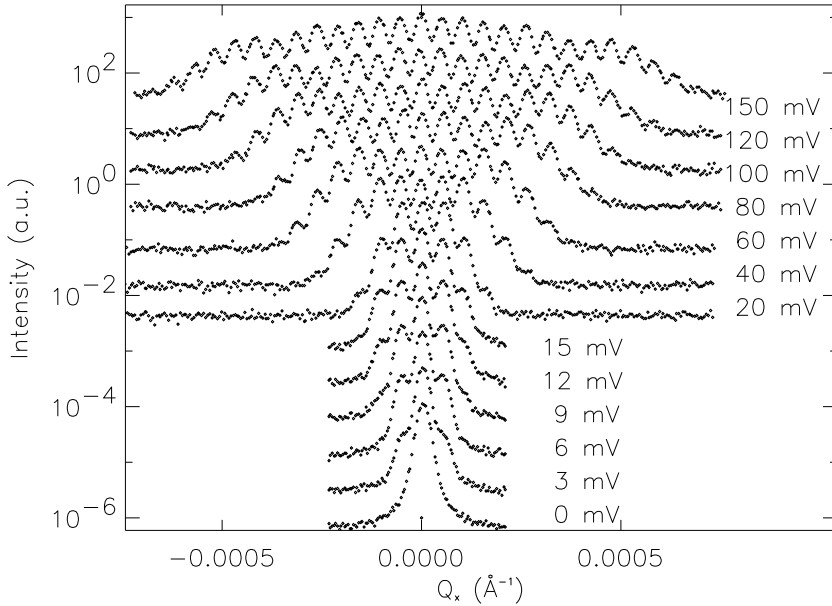


Figure 9.2: Series of experimental rocking curves measured on an acoustically excited LiNbO_3 crystal. The voltage applied to the piezoelectric transducer is indicated on the right of each curve. [Tuc99]

main peak with a certain half width, and no further lateral structure. As soon as a small voltage is applied to the transducer, the picture changes: Small lateral satellites emerge from the tails of the main peak. With increasing voltage their intensity rises. The satellite position, on the other hand, is constant in reciprocal space. In fact, the distance from the central Bragg peak is given by $\frac{2\pi}{D_{\text{SAW}}}$, where D_{SAW} is the wavelength of the acoustic waves which is kept constant. For even higher applied voltages second and higher order satellites appear. Their intensity increases until they eventually reach and (partially) exceed the intensity of the central peak.

9.3 Adaptation of the simulation procedure. Fit of experimental results

In order to interpret these experimental findings and to reproduce them in a theoretical calculation, we introduce a modification to the simulation procedure used in the previous chapters. There is no need any more to employ elasticity theory for the calculation of the strain field. Instead, we simply *assume* that the surface acoustic wave gives rise to a displacement field which varies sinusoidally along the lateral x -direction, and whose amplitude decays exponentially as a function of depth z below the sample surface. The wave is supposed to be purely transversal, i.e. all displacements are directed along the vertical direction, and no lateral deformation of any kind occurs. The complete displacement field is thus given by

$$\mathbf{u}(\mathbf{r}) = \begin{pmatrix} u_x \\ u_y \\ u_z \end{pmatrix} (\mathbf{r}) = \begin{pmatrix} 0 \\ 0 \\ A \cdot e^{z/z_{\text{SAW}}} \cos\left(\frac{2\pi}{D_{\text{SAW}}} \cdot x\right) \end{pmatrix}. \quad (9.1)$$

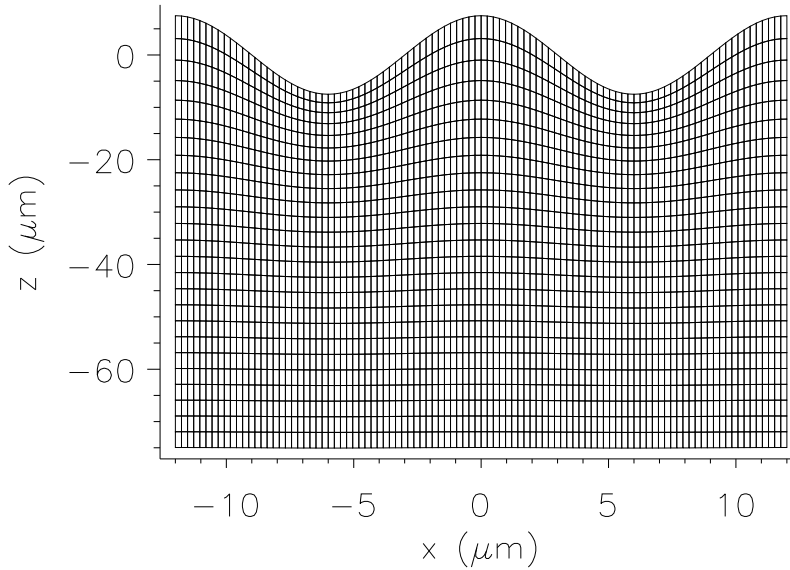


Figure 9.3: Plot of a typical lattice distortion as used for the calculations in this chapter, generated by applying the displacement field $\mathbf{u}(\mathbf{r})$ in (9.1) to an initially rectangular grid of points. The surface acoustic wave has a lateral period of 12 μm . The amplitude of the vertical displacement in the image is exaggerated by a factor 10^4 for better visibility. In reality, the absolute displacements are of the order of some \AA only.

The resulting non-zero components of the strain tensor $\epsilon_{ij} = \frac{1}{2} \left(\frac{\partial \mathbf{u}_i}{\partial x_j} + \frac{\partial \mathbf{u}_j}{\partial x_i} \right)$ are:

$$\epsilon_{xz} = -\frac{1}{2} A \cdot \frac{2\pi}{D_{\text{SAW}}} \cdot e^{z/z_{\text{SAW}}} \sin \left(\frac{2\pi}{D_{\text{SAW}}} \cdot x \right) \quad (9.2)$$

$$\epsilon_{zz} = A \cdot \frac{1}{z_{\text{SAW}}} \cdot e^{z/z_{\text{SAW}}} \cos \left(\frac{2\pi}{D_{\text{SAW}}} \cdot x \right) \quad (9.3)$$

All other components of the strain tensor vanish; in particular, no lateral strain ϵ_{xx} occurs. An image of a (formerly planar) structure distorted according to these formulae is shown in Fig. 9.3.

We would like to stress the fact that this is a mere *simplified model*, which does not fulfil the equations of elasticity theory. In a realistic description any vertical compression or expansion would have to be accompanied by a corresponding reaction in the lateral direction. However, the model can potentially yield correct simulated rocking curves since the measurements were done in *symmetrical* diffraction geometry, which is exclusively sensitive to the vertical displacement component. Taking into account an additional lateral displacement component would not alter the simulated version of this kind of curves. Finally, the comparison of measured and calculated rocking curve profiles will show that the model is indeed justified.

In order to simulate the diffraction pattern from a crystal under the influence of such a distortion field, we first create a rectangular grid of points equidistributed in one lateral period between $x = 0$ and $x = D_{\text{SAW}}$, and between the sample surface at $z = 0$ and a depth $z = -N \cdot z_{\text{SAW}}$. N is an integer number which is sufficiently large to ensure that the wave field is more or less totally damped at the corresponding depth below the surface ($N \approx 5 - 10$). For each of these nodes a vertical shift is calculated as a function of its x and z -position, according to the model given above. The values of displacement and strain are interpolated from the nodes to the *cells* of the grid, and then fed into our well-known simulation program for X-ray diffraction from strained structures.

In this way the diffracted intensity is calculated for each of the lateral satellite peak maxima. These values are finally convoluted with a resolution function, which is taken as a weighted average of a Gaussian and a Lorentzian curve profile. This procedure yields a complete simulated rocking curve for one special set of parameters (lateral period, penetration depth of the acoustic wave, acoustic amplitude, and width of the resolution function). In order to reproduce the experimental curves as exactly as possible, the free parameters must then be varied until a best fit is found. In a first step the parameters of the resolution function (width σ and ratio of Gaussian to Lorentzian contributions) are determined from a fit to the curve without acoustic excitation (lowest curve in Fig. 9.2). For the remaining parameters a fitting procedure is introduced, based on a non-linear least-squares minimization algorithm [PTV95]. In contrast to the previous chapters, it is now a “real” fit in the sense that it includes an automatic decision on the parameter values to be used for the next step as a function of the deviations between the latest simulation and the experimental curve. The fit loop is interrupted when sufficient agreement is achieved.

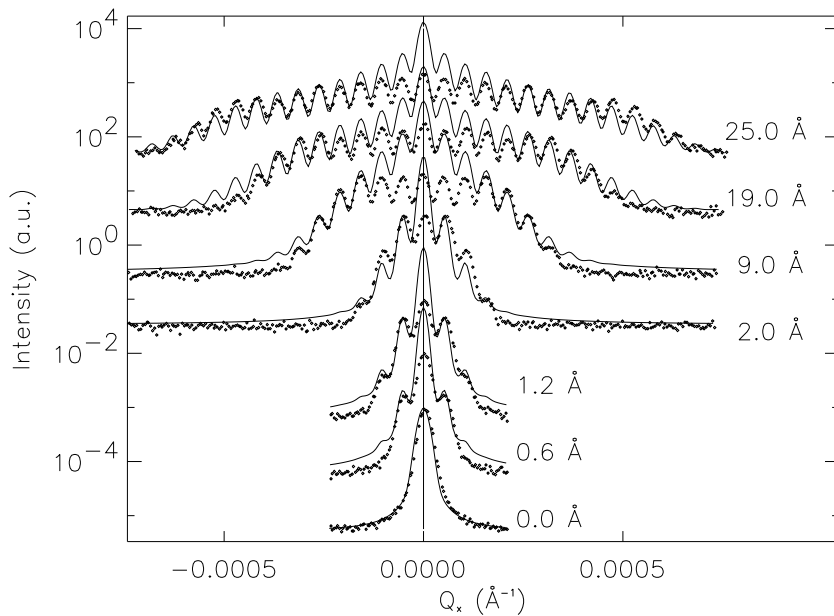


Figure 9.4: Comparison of measured (dotted) and fitted (full lines) rocking curves for selected amplitudes of the acoustic excitation. For reasons of clarity, only every second curve from the series in Fig. 9.2 is shown, together with the corresponding calculation. The numbers at the right end of each curve give the best-fit values of the acoustic amplitude.

The results are shown in Fig. 9.4, together with the experimental curves (for better comparison). All the simulated curves were generated with the same set of structural parameters, namely a lateral period of 12 μm and a penetration depth of the acoustic wave of 15 μm .¹ Only the amplitude was adapted individually for each case. In order to reduce the complexity of the image, only every second curve from the series of amplitudes in Fig. 9.2 is depicted in this image. The comparison shows that our model of the displacement field can indeed account for the experimentally observed effects. Satellite peaks at the different grating orders emerge for small amplitudes of the acoustic wave field, and grow with increasing excitation. Their slope is in good agreement with the experimental values, especially for the higher grating orders.

¹In any case, the acoustic penetration is not crucial: From the simulation it turns out that a variation of z_{SAW} in the range of 5–50 μm does not affect the rocking curves noticeably. This becomes understandable if one takes into account that the penetration depth of the probing X-rays is even lower. They interact essentially only with the completely deformed layer very close to the surface, independently of how the acoustic deformation decays in the region below.

In the central regions (main peak and low-order grating satellites) some discrepancies remain: The simulated curves are systematically higher than their experimental counterparts. This is an indication that we have now reached the limits of validity of the semi-kinematical diffraction model on which our simulation formalism is based. In fact, it is well known that for relatively large, perfect crystals the kinematical diffraction theory yields an intensity which is proportional to the *square* of a structure factor $|F_{HKL}^2|$, whereas dynamical diffraction theory leads to a simple proportionality $I \sim |F_{HKL}|$. In other words, a kinematical approach *overestimates* the diffracted intensity from anything but very thin or highly disturbed samples. Now, the thickness of the SAW layer is orders of magnitude larger than the etched layer thicknesses dealt with in the preceding chapters. The penetration depth of the acoustic wave is of the order of some $10 \mu\text{m}$, while typical heights of our etched gratings were approximately 100 nm. Therefore the deviations around the central Bragg peak can be easily understood. The higher grating orders with their corresponding smaller structure factors are not affected by this argumentation.

The amplitudes used for the best fit of each single curve are indicated on the right in Fig. 9.4. They are approximately of the order expected from the voltages applied (and the proportionality factor 0.1 \AA/mV), especially for the lower curves. In order to obtain good agreement also for the upper curves, slightly larger amplitudes had to be used; the value found for the top curve deviates by a factor 1.4 from the nominal value. Such a deviation is acceptable since it remains within the limits of experimental uncertainty for the transducer.

One more point deserves to be mentioned here: In order to obtain the best agreement, we needed to assume that the acoustic waves were *standing* waves. For standing waves the displacement oscillates periodically in time, with an amplitude of the sinusoidal spatial wave which varies between 0 and a maximum value. Therefore the diffraction pattern from a standing wave with a given maximum amplitude (as determined by the voltage applied to the transducer) must be calculated as an average. Each intermediate deformation state between zero and maximum amplitude must be taken into account, weighted with the time spent in the respective configuration. For the same maximum amplitude this leads to satellite peaks which are weaker than the satellites in the case of travelling waves, since the maximum deviation from equilibrium is adopted only for a short portion of total time. Therefore, in order to fit the same experimental curves with a model of *travelling* waves, we would need to use amplitude values very much lower than the expected ones, far beyond the limits of experimental uncertainty.

Some possibilities to further improve the agreement have not been exploited yet. The most obvious is to additionally introduce *higher harmonic* components of the acoustic wave field. A component with a wavelength of $\lambda_0/2$, for instance, would selectively affect the intensity of every second lateral satellite in the rocking curve. In this way, by taking into account a large set of higher harmonic frequencies, the whole series of lateral satellites can be fitted quasi *individually* to almost arbitrary perfection.

9.4 Conclusion

In summary, we have extended our method to a completely different type of laterally periodic structures. The samples studied in this chapter were not permanently laterally structured via etching, but temporarily patterned under the influence of surface acoustic waves. In a certain sense, this kind of patterning represents the purest possible form of a “strain grating”, a notion which we have encountered before in chapters 6 and 7.

The experimentally measured rocking curves were analyzed with the help of a modified version of our evaluation procedure. Instead of calculating a grating-induced strain field by elasticity theory, we made the simplifying assumption that the vertical displacement varies sinusoidally as a function of lateral distance. From this displacement field we calculated the rocking curve profile with the same simulation mechanism as exposed before.

Good agreement was achieved for the whole set of acoustic amplitudes and over the whole range of the respective curves, with best-fit parameters that are close to the nominal values that were to be expected due to the experimental conditions. The only systematic deviations between simulation and experiment occur in the immediate vicinity of the Bragg peak. This deviation indicates that the limits of validity of our semi-kinematical diffraction model start to be reached, since the deformed region is now orders of magnitude

thicker than the patterned layers in previous chapters. Apart from this detail, the successful application of our simulation procedure to this new kind of lateral patterning can be regarded as a proof for the robustness of the method.

Summary and perspectives

This work has shown how semiconductor structures can be universally characterized in view of lattice distortions by X-ray diffraction techniques using synchrotron radiation. A broad spectrum of sample types can be investigated in this way, reaching from semiconductor wafers [LBH00] via planar multilayers, surface gratings and quantum wires [LJB99] to complete mounted semiconductor devices under operation [ZBG99]. Two kinds of examples were selected to demonstrate the experimental techniques and analysis procedures: wafers and gratings.

Part II presented an experimental method that was developed for the direct measurement of lattice distortions in crystalline structures with spatial variations on a length scale of some μm . By combining the respective advantages of X-ray diffractometry with those of X-ray diffraction topography, it became possible to measure quantitatively the detailed spatial distribution of rocking curve half widths (which are taken as a local crystalline quality parameter) and of microscopic lattice tilts, as well as the macroscopic sample curvature. The speed, flexibility and high spatial resolution of the technique, ensured by the special properties of synchrotron X-ray beams and by the availability of a fast digital X-ray camera, make it a very attractive tool for the quantitative investigation of problems arising in crystal growth and engineering.

An instrumental equipment and a data analysis software were developed and installed at the ID19 beamline of the ESRF to implement the method. This allowed to demonstrate the feasibility and to carry out a first series of experiments. Chapter 4 showed results obtained on semiconductor wafers of two different materials, namely GaAs and SiC. The rocking curve half widths of locally perfect crystallites and of regions containing defects could be measured separately. In this way, the method allows to correlate the variations in macroscopic quality parameters with the underlying microscopic mechanisms (defects of the crystal lattice).

Two kinds of further developments and methodical improvements are envisaged for the future: First, the technique for μm -resolved rocking curve imaging can be applied to the study not only of wafers, but of complete semiconductor devices under operation conditions. In the example of the semiconductor laser diodes [ZBG99], this will allow to monitor *in situ* and in real-time the thermal strain and the formation of defects in the active layer of the laser, and thus to clarify further the mechanisms which ultimately lead to the degradation of device performance. Second, by adding an analyzer crystal to the experimental setup, it will be possible to extend the scope of the investigation and to measure also variations in the local lattice parameters in highly perturbed samples. These two perspectives show how the method can be used to answer further relevant questions arising in applied as well as in fundamental semiconductor physics.

Part III of the thesis was dedicated to the study of lattice distortions on an even smaller length scale, namely of the coherent strain and strain relaxation occurring in lattice-mismatched surface gratings and quantum wires with a lateral period of some 10 – 100 nanometers. Strain fields in structures of this size cannot be observed “directly”, due to the lack of sufficient *real-space* resolution in present X-ray methods. Instead, they can be investigated due to interference effects by high-resolution X-ray diffractometry, thus separating the contributions from different materials in *reciprocal space*. The grating truncation rod patterns in reciprocal space maps contain information about both the grating geometry and the grating-induced strain relaxation. By simultaneous use of elasticity theory and semi-kinematical X-ray diffraction theory it became possible for the first time to evaluate quantitatively the complete inhomogeneous strain fields in nanoscopic semiconductor structures.

The method has been successfully applied to a detailed experimental investigation of various aspects of strain fields in surface gratings. Chapter 6 revealed the depth-dependent character of the strain relaxation

in $\text{Ga}_x\text{In}_{1-x}\text{As}_y\text{P}_{1-y}/\text{InP}$ gratings induced by the etching process, and its evolution in the subsequent burying growth step. The relaxation could be shown to be partially reversed by the action of the embedding layer which, in turn, gets strained in this process. A periodic distortion field in this homogeneous cap layer, a “strain grating”, could be revealed for the first time by a combination of two complementary measuring modes in grazing incidence diffraction. Chapter 7 addressed the issue of variations in the grating shape and their effect on the diffraction pattern via the comparative study of trapezoidal and rectangular gratings, both etched into $\text{Ga}_x\text{In}_{1-x}\text{As}/\text{InP}$. Detailed simulations, clarifying the influence of all relevant parameters by automatic fit loops, secured the validity of the analysis. Chapter 8 extended the method to a more complicated sample type, to superlattices. Their strain relaxation properties could be shown to reflect the vertically periodic layer setup: In the case of a compressively strained $\text{Ga}_x\text{In}_{1-x}\text{As}/\text{InP}$ superlattice, the ternary layers were found to relax by expanding, while the binary layers experience additional tensile in the same process.

From the very good agreement achieved between experimental and simulated reciprocal space maps two more general conclusions can furthermore be drawn: First, continuum elasticity theory can provide a valid description of the lattice distortions in epitaxial structures with dimensions in the range of 10–100 nm. Second, a semi-kinematical approximation of X-ray scattering theory is sufficient to explain the relevant features observed in typical diffraction patterns obtained from our type of samples.

The final Chapter 9 demonstrated how the analysis procedure can be extended to a completely different type of lateral patterning, namely the case of surface acoustic waves. The successful transfer of the formalism from artificially etched gratings to acoustically excited surfaces contributed to proving the flexibility and general applicability of the investigation method. In fact, surface acoustic waves represent just one example out of a larger class of semiconductor structures which exhibit lateral periodicity without being artificially etched. Remarkably perfect lateral periodicities can also be realized in a *self-organized* way: either via step bunching in the growth of strained multilayers on vicinal surfaces [BGL99, GBL00], or by the formation of periodic arrays of dislocations in twist-bonded Si wafers [BER99]. Both types of self-organized patterning have recently been investigated by X-ray methods. The strain fields in these samples promise to be amenable to quantitative analysis with the same methods as exposed in this work.

Appendix A

Transformation of elastic constants into different coordinate systems

In order to perform correctly the Finite Element calculations according to the method exposed in Section 5.3, it is important to first convert the elastic constants of the material to the system of reference used in the calculation. Therefore, we document here the main steps involved in this conversion.

Hooke's law states that the strains are proportional to stresses. In the general case of anisotropic bodies (such as crystals) it can be written as

$$\epsilon_{ij} = S_{ijkl} \cdot \sigma_{kl}, \quad (\text{A.1})$$

where S is called the *compliance* tensor. Its inverse is the *stiffness* tensor C :

$$\sigma_{ij} = C_{ijkl} \cdot \epsilon_{kl}. \quad (\text{A.2})$$

In this appendix we will study the symmetries and transformation properties of S_{ijkl} and C_{ijkl} , the knowledge of which is a precondition for performing numerical calculations of strain fields.

Coordinate transformations

The numerical values of the S_{ijkl} and C_{ijkl} depend on the system of reference. A transformation between two coordinate systems can be described with the help of a rotation matrix \mathcal{R} . The components r'_i of a vector in the new system follow from those in the old system (r_j) by

$$r'_i = \mathcal{R}_{ij} \cdot r_j \quad (\text{A.3})$$

Strain and stress are *tensors*, in the sense that they transform according to [CP92]

$$\epsilon'_{ij} = \mathcal{R}_{ik} \mathcal{R}_{jl} \cdot \epsilon_{kl} \quad (\text{A.4})$$

S_{ijkl} and C_{ijkl} are also tensors (of fourth order) [CP92, AL88], i.e. they transform according to

$$S'_{ijkl} = \mathcal{R}_{im} \mathcal{R}_{jn} \mathcal{R}_{kp} \mathcal{R}_{lq} \cdot S_{mnpq} \quad (\text{A.5})$$

Symmetry of strain and stress tensors. Shorthand notation

The strain tensor ϵ_{ij} is symmetrical by definition (5.20), $\epsilon_{ij} = \epsilon_{ji}$, and σ_{ij} can also be defined so as to be symmetrical [LL86]. Therefore, they do not have 9, but only 6 independent components, which can be written in a shorthand notation as column vectors. For stresses, the common definition is [Nye95]:

$$\sigma_1 = \sigma_{11}, \quad \sigma_2 = \sigma_{22}, \quad \sigma_3 = \sigma_{33}, \quad \sigma_4 = \sigma_{23}, \quad \sigma_5 = \sigma_{13}, \quad \sigma_6 = \sigma_{12}. \quad (\text{A.6})$$

For the strains, additional factors of 2 are required:

$$\epsilon_1 = \epsilon_{11}, \quad \epsilon_2 = \epsilon_{22}, \quad \epsilon_3 = \epsilon_{33}, \quad \epsilon_4 = 2 \cdot \epsilon_{23}, \quad \epsilon_5 = 2 \cdot \epsilon_{13}, \quad \epsilon_6 = 2 \cdot \epsilon_{12}, \quad (\text{A.7})$$

Compliance and stiffness can similarly be written as matrices with 2 instead of 4 indices. For the stiffness, the two pairs of indices are contracted independently, according to the same rule as in (A.6). For the compliance, factors of 2 and 4 need to be introduced:

$$S_{mn} = \begin{cases} S_{ijkl} & \text{if } m, n \in [1,3] \\ 2 \cdot S_{ijkl} & \text{if } m \in [1,3] \text{ and } n \in [4,6] \text{ (or vice-versa)} \\ 4 \cdot S_{ijkl} & \text{if } m, n \in [4,6] \end{cases} \quad (\text{A.8})$$

These factors are in fact necessary in order Hooke's law to be valid in the new form

$$\epsilon_i = S_{ij} \cdot \sigma_j \quad \text{and} \quad \sigma_i = C_{ij} \cdot \epsilon_j. \quad (\text{A.9})$$

In the literature, numerical values for the elastic constants are often given in the form of the elements of the stiffness matrix C_{ij} . This matrix is symmetrical, and can have a maximum of 21 independent components. For cubic crystals, symmetry conditions show that this number is reduced to 3, and C_{ij} assumes the form

$$C_{ij} = \left(\begin{array}{ccc|ccc} C_{xxxx} & C_{xxyy} & C_{xyyy} & 0 & 0 & 0 \\ C_{xxyy} & C_{xyyy} & C_{xxxx} & 0 & 0 & 0 \\ C_{xyyy} & C_{xxxx} & C_{xxxx} & 0 & 0 & 0 \\ \hline . & . & . & C_{zxxz} & 0 & 0 \\ . & . & . & . & C_{zxxz} & 0 \\ . & . & . & . & . & C_{zxxz} \end{array} \right) \quad (\text{A.10})$$

The values of $C_{11} = C_{xxxx}$, $C_{12} = C_{xxyy}$ and $C_{44} = C_{zxxz}$ are well documented in the literature for material systems like $\text{Ga}_x\text{In}_{1-x}\text{As}_y\text{P}_{1-y}$ or $\text{Ga}_x\text{Al}_{(1-x)}\text{As}$ [Ada82, Ada85]. The compliance matrix S_{ij} can be found from C_{ij} via simple 6×6 matrix inversion.

The main drawback of the shorthand formulation is that S_{ij} and C_{ij} , unlike S_{ijkl} and C_{ijkl} are not tensors any more. Their components in a rotated frame of reference can *not* be calculated according to the transformation law for second-order tensors (eq. (A.4)). This fact is important when the coordinate system for the strain calculation is not chosen parallel to the crystallographic axes of cubic symmetry, but differently, such as we did in the case of [110]-oriented gratings in Chapters 6-8. Many FEM programs then require as input the values of C'_{ij} in the rotated system of reference, or even (as in the case of the program available for this thesis) the values of the "engineering" elastic constants, namely the *Young moduli* E_i , the *shear moduli* G_{ij} and the *Poisson ratio* ν_{ij} [TG87]. These are related to the compliance in the same reference system via

$$E'_i = \frac{1}{S'_{iiii}} \quad \nu'_{ij} = -\frac{S'_{iiji}}{S'_{iiii}} \quad G'_{ij} = \frac{1}{4 \cdot S'_{ijij}} \quad (\text{A.11})$$

Before proceeding to a practical FEM calculation, one therefore has to perform a transformation of the elastic constants in several consecutive steps. The general scheme can be summarized as:

$$\left. \begin{array}{c} C_{11} \\ C_{12} \\ C_{44} \end{array} \right\} \Rightarrow C_{ij} \Rightarrow S_{ij} \Rightarrow S_{ijkl} \Rightarrow S'_{ijkl} \Rightarrow \left\{ \begin{array}{c} E'_i \\ \nu'_{ij} \\ G'_{ij} \end{array} \right.$$

More explicitly, the calculation involves the following steps:

- Find a complete set of elastic constants, e.g. (for a cubic material) C_{11} , C_{12} and C_{44} .
- Construct the 6×6 stiffness matrix C_{ij} via (A.10).

-
- Calculate the compliance S_{ij} by 6×6 matrix inversion.
 - From S_{ij} , construct S_{ijkl} by inversion of (A.8).
 - Rotate S_{ijkl} according to (A.5) to get S'_{ijkl} .
 - Find the values of E'_i , ν'_{ij} and G'_{ij} from (A.11).

For the calculations shown in the experimental part of the present thesis, these steps were automatized in a C++-program. Such an automatic procedure is particularly useful for fit loops over different material compositions, such as the one shown in Fig. 7.3.

Let us mention that the formulae for the transformation of S_{ijkl} and C_{ijkl} to a rotated system of reference have been re-expressed by ANASTASSAKIS and LIAROKAPIS [AL88] in a form which simplifies the explicit calculation “by hand”. However, we believe the concatenation of the different steps exposed in this Appendix to be more transparent and to be more easily implemented for the numerical calculation in a computer program.

For easy reference, we finally document here the values of C_{11} , C_{12} and C_{44} (expressed in 10^{11}dyn/cm^2) for the binary compounds of the material system $\text{Ga}_x\text{In}_{1-x}\text{As}_y\text{P}_{1-y}$ [Ada82]:

	C_{11}	C_{12}	C_{44}
GaAs	11.88	5.38	5.94
GaP	14.120	6.253	7.047
InAs	8.329	4.526	3.959
InP	10.22	5.76	4.60

The values for ternary and quaternary semiconductors can be calculated via linear interpolation between the values of the corresponding binary compounds (*Vegard's law*).

Bibliography

- [Abe50] F. ABELÈS. *Recherche sur la propagation des ondes électromagnétiques sinusoïdales dans les milieux stratifiés*. Ann. Phys. (Paris) **5**, p. 596–640 (1950).
- [Ada82] S. ADACHI. *Material parameters of $In_{1-x}Ga_xAs_yP_{1-y}$ and related binaries*. J.Appl.Phys. **53**(12), p. 8775–8792 (1982).
- [Ada85] S. ADACHI. *GaAs, AlAs, and $Al_xGa_{1-x}As$: material parameters for use in research and device applications*. J.Appl.Phys. **58**(3), p. R1–R29 (1985).
- [Ada86] A. ADAMS. Electron. Lett. **22**, p. 249 (1986).
- [AKK74] L. AZAROFF, R. KAPLOW, N. KATO, R. WEISS, A. WILSON, and R. YOUNG. *X-ray diffraction*. McGraw-Hill Book Company (1974).
- [AL88] E. ANASTASSAKIS and E. LIAROKAPIS. *A macroscopic application of the Wigner-Eckart theorem*. Phys.Stat.Sol. **149**, p. K1 (1988).
- [ALK86] N. ANDERSON, W. LAIDIG, R. KOLBAS, and Y. LO. *Optical characterization of pseudo-morphic $In_xGa_{1-x}As$ – GaAs single-quantum-well heterostructures*. J.Appl.Phys. **60**(7), p. 2361–2367 (1986).
- [ALT96] A. AUTHIER, S. LAGOMARSINO, and B. K. TANNER, editors. *X-ray and Neutron Dynamical Diffraction - Theory and Applications*. Volume 357 of *NATO ASI Series B: Physics*. Plenum Press (1996).
- [AMS86] M. ASADA, Y. MIYAMOTO, and Y. SUEMATSU. *Gain and the threshold of the three-dimensional quantum-box lasers*. IEEE J. Quantum Electr. **QE-22**, p. 1915 (1986).
- [AS82] Y. ARAKAWA and H. SAKAKI. *Multidimensional quantum well laser and temperature dependence of its threshold current*. Appl.Phys.Lett. **40**(11), p. 939–941 (1982).
- [ASD87] M. ADAMS, A. STEVENTON, W. DEVLIN, and I. HENNING. *Semiconductor Lasers for Long-Wavelength Optical-Fiber Communication Systems*. Peter Peregrinus Ltd. (1987).
- [AT98] T. AONO and S.-I. TAMURA. *Surface and pseudosurface acoustic waves in superlattices*. Phys. Rev. B **58**(8), p. 4838–4845 (1998).
- [Aut77] A. AUTHIER. *Section Topography*. In Queisser [Que77].
- [Aut93] A. AUTHIER. *Dynamical theory of X-ray diffraction*. In U. SHMUELI, editor, *International Tables for Crystallography*. Volume B. Kluwer Academic Publishers (1993).
- [Aza68] L. AZAROFF. *Elements of X-ray crystallography*. McGraw-Hill Book Company 6 edition (1968).
- [Bar45] C. BARRETT. Trans. A.I.M.E. **161**, p. 15 (1945).

- [BBF98] O. BUCHINSKY, M. BLUMIN, and D. FEKETE. *n-type delta-doped strained quantum well lasers for improved temperature-dependent performance*. Appl.Phys.Lett. **72**(12), p. 1484–1486 (1998).
- [BBP92] L. BRÜGEMANN, R. BLOCH, W. PRESS, and M. TOLAN. *Resolution Investigation of X-ray Three-Crystal Diffractometers*. Acta Cryst. A **48**, p. 688–692 (1992).
- [BC64] B. W. BATTERMAN and H. COLE. *Dynamical Diffraction of X Rays by Perfect Crystals*. Rev.Mod.Phys. **36**(3), p. 681–717 (1964).
- [BEM97] N. BOUDET, J. EYMERY, and N. MAGNÉA. *X-ray diffraction study of the lattice distortions induced by a fractional monolayer: ZnTe embedded in vicinal CdTe(001)*. Phys. Rev. B **55**(23), p. 15804–15812 (1997).
- [BER99] D. BUTTARD, J. EYMERY, F. RIEUTORD, F. FOURNEL, D. LÜBBERT, T. BAUMBACH, and H. MORICEAU. *Grazing incidence X-ray studies of twist-bonded Si/Si and Si/SiO₂ interfaces*. Proceedings of the Sixth International Conference on Surface X-ray and Neutron Scattering (6SNXS) (1999).
- [BES99] J. BUNDGAARD, K. ENEVOLDSEN, and P. SKAARUP. *TASCOM user manual*. Risø National Laboratory Roskilde, Denmark (1999).
- [BG95] T. BAUMBACH and M. GAILHANOU. *X-ray diffraction from epitaxial multilayered surface gratings*. J.Phys.D:Appl.Phys. **28**, p. 2321–2327 (1995).
- [BGL99] G. T. BAUMBACH, C. GIANNINI, D. LÜBBERT, R. FELICI, L. TAPFER, T. MARSCHNER, and W. STOLZ. *Investigation of Strain Induced Patterning in Superlattices by Grazing Incidence Diffraction - Comparison of Morphological and Strain Ordering*. J.Phys.D:Appl.Phys. **32**, p. A212–A215 (1999).
- [BH81] U. BONSE and I. HARTMANN. *X-ray measurement of minute lattice strain in perfect silicon crystals*. Z.f. Kristallographie **156**, p. 265–279 (1981).
- [BHP94] T. BAUMBACH, V. HOLÝ, U. PIETSCH, and M. GAILHANOU. *The influence of specular interface reflection on grazing incidence X-ray diffraction and diffuse scattering from superlattices*. Physica B **189**, p. 249–252 (1994).
- [BL67] W. R. BUSING and H. A. LEVY. *Angle Calculations for 3- and 4-Circle X-ray and Neutron Diffractometers*. Acta Cryst. **22**, p. 457–464 (1967).
- [BL99] T. BAUMBACH and D. LÜBBERT. *Grazing incidence diffraction by laterally patterned semiconductor nanostructures*. J.Phys.D:Appl.Phys. **32**, p. 726–740 (1999).
- [BLG99a] G. T. BAUMBACH, D. LÜBBERT, and M. GAILHANOU. *X-ray structure investigation of lateral surface nano-structures - a full quantitative analysis of non-uniform lattice strain*. J.Phys.D:Appl.Phys. **32**, p. A208–A211 (1999).
- [BLG99b] T. BAUMBACH, D. LÜBBERT, and M. GAILHANOU. *Strain relaxation in surface nanostructures studied by X-ray diffraction methods*. Jap.J.Appl.Phys., Part I **38**(12A), p. 6591–6596 (1999).
- [BLG00] T. BAUMBACH, D. LÜBBERT, and M. GAILHANOU. *Strain and shape analysis of multi-layer surface gratings by coplanar and by grazing incidence X-ray diffraction*. accepted for publication in J.Appl.Phys. **87**(8), p. 3744–3758 (2000).
- [Blo85] J. M. BLOCH. *Angle and Index Calculations for a 'z-axis' X-ray Diffractometer*. J.Appl.Cryst. **18**, p. 33–36 (1985).
- [BPB92] O. BRANDT, K. PLOOG, R. BIERWOLF, and M. HOHENSTEIN. *Breakdown of Continuum Elasticity Theory in the Limit of Monatomic Films*. Phys. Rev. Lett. **68**, p. 9 (1992).

- [Bra97] D. BRAESS. *Finite elements. Theory, fast solvers and applications in solid mechanics*. Cambridge University Press (1997).
- [BT98] D. K. BOWEN and B. K. TANNER. *High Resolution X-ray Diffractometry and Topography*. Taylor & Francis (1998).
- [BTP95] T. BAUMBACH, S. TIXIER, U. PIETSCH, and V. HOLÝ. *Grazing-incidence diffraction from multilayers*. Phys. Rev. B **51**(23), p. 16848–16859 (1995).
- [BW80] M. BORN and E. WOLF. *Principles of Optics*. Pergamon Press 6 edition (1980).
- [CAS94] S. CHRISTIANSEN, M. ALBRECHT, H. STRUNK, and H. MAIER. *Strained state of Ge(Si) islands on Si: Finite element calculations and comparison to convergent beam electron-diffraction measurements*. Appl.Phys.Lett. **64**(26), p. 3617–3619 (1994).
- [CDL95] P. CHEVALLIER, P. DHEZ, F. LEGRAND, M. IDIR, G. SOULLIE, A. MIRONE, A. ERKO, A. SNIGIREV, I. SNIGIREVA, A. SUVOROV, A. FREUND, P. ENGSTRÖM, J. ALS NIELSEN, and A. GRÜBEL. *First test of the scanning X-ray microprobe with Bragg-Fresnel multilayer lens at ESRF beam line*. Nucl. Instr. Meth. A **354**, p. 584–587 (1995).
- [Ced99] A. CEDOLA. *Production des faisceaux de rayons X submicroniques par guide d'onde en couches minces*. PhD thesis Université Joseph Fourier, Grenoble, France (1999).
- [Cer99] Certified Scientific Software Cambridge, Massachusetts. *SPEC user manual* (1999). version 2.7.
- [Clo99] P. CLOETENS. *Contribution to Phase Contrast Imaging, Reconstruction and Tomography with Hard Synchrotron Radiation*. PhD thesis Vrije Universiteit Brussel, Belgium (1999).
- [CNM99] F. COMIN, M. NAVIZET, P. MANGIAGALLI, and G. APOSTOLO. *An industrial TXRF facility at ESRF*. Nucl. Instr. Meth. B **150**, p. 538–542 (1999).
- [Cor98] S. W. CORZINE. *Semiconductor light-source essentials*. IEEE Spectrum p. 44–45 (1998).
- [Cow87] R. COWLEY. *Resolution Function on an X-ray Triple-Crystal Diffractometer*. Acta Cryst. A **43**, p. 825–836 (1987).
- [CP92] P. C. CHOU and N. J. PAGANO. *Elasticity. Tensor, dyadic and engineering approaches*. Dover (1992).
- [CRS94] Y.-P. CHEN, J. D. REED, W. J. SCHAFF, and L. EASTMAN. *Measurement of nonuniform distribution of strain in InGaAs/GaAs quantum wires*. Appl.Phys.Lett. **65**(17), p. 2202–2204 (1994).
- [Dar14a] C. DARWIN. *The theory of x-ray reflection*. Philos.Mag. **27**, p. 315–333 (1914).
- [Dar14b] C. DARWIN. *The theory of x-ray reflection, Part II*. Philos.Mag. **27**, p. 675–690 (1914).
- [Dar99] N. DAROWSKI. *Untersuchung vergrabener Lateralstrukturen auf Halbleiteroberflächen mit Hilfe der Methode der Röntgenbeugung unter streifendem Einfall (GID)*. PhD thesis Universität Potsdam (1999).
- [dB94] D. DE BOER. *Influence of the roughness profile on the specular reflectivity of x rays and neutrons*. Phys. Rev. B **49**(9), p. 5817–5820 (1994).
- [DBW98] A. DARHUBER, G. BAUER, P. WANG, and C. SOTOMAYOR TORRES. *Shear strains in dry etched GaAs/AlAs wires studied by high resolution x-ray reciprocal space mapping*. J.Appl.Phys. **83**(1), p. 126–131 (1998).

- [DCST94] L. DE CARO, P. SCIACOVELLI, and L. TAPFER. *Double crystal x-ray diffraction from periodically corrugated crystalline semiconductor surfaces*. Appl.Phys.Lett. **64**(1), p. 34–36 (1994).
- [DCT93] L. DE CARO and L. TAPFER. *Elastic lattice deformation of semiconductor heterostructures grown on arbitrarily oriented substrate surfaces*. Phys. Rev. B **48**(4), p. 2298–2303 (1993).
- [DCT94] L. DE CARO and L. TAPFER. *Elastic lattice deformation in quantum-wire heterostructures*. Phys. Rev. B **49**(16), p. 11127–11133 (1994).
- [DCT95a] L. DE CARO and L. TAPFER. *Strain and piezoelectric fields in arbitrarily oriented semiconductor heterostructures. I. Multiple quantum wells*. Phys. Rev. B **51**(7), p. 4373–4380 (1995).
- [DCT95b] L. DE CARO and L. TAPFER. *Strain and piezoelectric fields in arbitrarily oriented semiconductor heterostructures. II. Quantum wires*. Phys. Rev. B **51**(7), p. 4381–4387 (1995).
- [DCTG96] L. DE CARO, L. TAPFER, and A. GIUFFRIDA. *Finite-size effects in one-dimensional strained semiconductor heterostructures*. Phys. Rev. B **54**(15), p. 10575–10584 (1996).
- [DHH99] M. DUDLEY, X. HUANG, W. HUANG, A. POWELL, S. WANG, P. NEUDECK, and M. SKOWRONSKI. *The mechanism of micropipe nucleation at inclusions in silicon carbide*. Appl.Phys.Lett. **75**(6), p. 784–786 (1999).
- [DKB95] A. DARHUBER, E. KOPPENSTEINER, G. BAUER, P. WANG, Y. SONG, C. SOTOMAYOR TORRES, and M. HOLLAND. *Structural investigations of GaAs/AlAs quantum wires and quantum dots by x-ray reciprocal space mapping*. J.Phys.D:Appl.Phys. **28**, p. A195–A199 (1995).
- [Dos87] H. DOSCH. *Evanescence absorption in kinematic surface Bragg diffraction*. Phys. Rev. B **35**(5), p. 2137–2143 (1987).
- [Dos92] H. DOSCH. *Critical phenomena at surfaces and interfaces*. Volume 126 of *Springer Tracts in Modern Physics*. Springer (1992).
- [DSSS95] W. DRUBE, H. SCHULTE-SCHREPPING, H.-G. SCHMIDT, R. TREUSCH, and G. MATERLIK. *Design and performance of the high-flux/high-brightness x-ray wiggler beamline BW2 at HASYLAB*. Rev. Sci. Instr. **66**(2), p. 1668–1670 (1995).
- [DuM37] J. W. DUMOND. *Theory of the Use of More Than Two Successive X-Ray Crystal Reflections to Obtain Increased Resolving Power*. Phys.Rev. **52**, p. 872–883 (1937).
- [ELK92] E. ELKAIM, S. LEFEBVRE, R. KAHN, J. BERAR, M. LEMONNIER, and M. BESSIÈRE. *Diffraction and diffuse scattering measurements in material science: Improvement brought to a six-circle goniometer on a synchrotron beamline*. Rev. Sci. Instr. **63**(1), p. 988–991 (1992).
- [ELT95] K. W. EVANS-LUTTERODT and M.-T. TANG. *Angle Calculations for a '2+2' Surface X-ray Diffractometer*. J.Appl.Cryst. **28**, p. 318–326 (1995).
- [ERS89] A. ERKO, D. ROSHCHUPKIN, A. SNIGIREV, A. SMOLOVICH, A. NIKULIN, and G. VERESHCHAGIN. *X-ray diffraction on a multilayer structure modulated by surface acoustic waves*. Nucl. Instr. Meth. A **282**, p. 634–637 (1989).
- [Ewa13] P. EWALD. Phys.Z. **14**, p. 465 (1913).
- [Ewa16a] P. EWALD. *Zur Begründung der Kristalloptik. Teil I: Theorie der Dispersion*. Ann. der Physik **49**, p. 1–38 (1916).

- [Ewa16b] P. EWALD. *Zur Begründung der Kristalloptik. Teil II: Theorie der Reflexion und Brechung.* Ann. der Physik **49**, p. 117–143 (1916).
- [Ewa17] P. EWALD. *Zur Begründung der Kristalloptik. Teil III: Die Kristalloptik der Röntgenstrahlen.* Ann. der Physik **54**, p. 519–597 (1917).
- [FKK97] C. FERRARI, D. KORYTAR, and J. KUMAR. *Study of residual strains in wafer crystals by means of lattice tilt mapping.* Il Nuovo Cimento **19D**(2-4), p. 165–173 (1997).
- [FKL12] W. FRIEDRICH, P. KNIPPING, and M. v. LAUE. Proc. Bav. Acad. Sci. p. 303 (1912).
- [Gai95] M. GAILHANOU. *Étude de la structure latérale de monocristaux semiconducteurs par diffraction de rayons X triple cristal.* PhD thesis Ecole Polytechnique Fédérale de Lausanne (1995).
- [Gai98] M. GAILHANOU. *Personal communication.* (1998).
- [Gal91] Y. GALEUCHET. *Metalorganic vapor-phase epitaxy on patterned substrates for the fabrication of in situ-buried $\text{Ga}_x\text{In}_{1-x}\text{As}/\text{InP}$ nanostructures.* PhD thesis Ecole Polytechnique Fédérale de Lausanne (1991).
- [GBL00] C. GIANNINI, T. BAUMBACH, D. LÜBBERT, R. FELICI, L. TAPFER, W. MARSCHNER, T. STOLZ, N. JIN-PHILLIPP, and J. PHILLIPP. *Strain-driven transition from stepped interface to regularly spaced macrosteps in $(\text{GaIn})\text{As}/\text{Ga}(\text{AsP})$ symmetrically strained superlattices.* Phys. Rev. B **61**(3), p. 2173–2179 (2000).
- [GBM93] M. GAILHANOU, T. BAUMBACH, U. MARTI, P. SILVA, F. REINHART, and M. ILEGEMS. *X-ray diffraction reciprocal space mapping of a GaAs surface grating.* Appl.Phys.Lett. **62**(14), p. 1623–1625 (1993).
- [GC90] E. GARTSTEIN and R. COWLEY. *The Intensity Distribution Observed with a Multi-Crystal X-ray Diffractometer.* Acta Cryst. A **46**, p. 576–584 (1990).
- [GMM97] M. S. GOORSKY, K. MATNEY, M. MESHKINPOUR, D. STREIT, and T. BLOCK. *Reciprocal space mapping for semiconductor substrates and device heterostructures.* Il Nuovo Cimento **19D**(2-4), p. 257–266 (1997).
- [GRT93] H. GOERING, H.-G. ROOS, and L. TOBISKA. *Finite-Element-Methode.* Akademie Verlag 3rd edition (1993).
- [Gui94] A. GUINIER. *X-Ray Diffraction in crystals, imperfect crystals and amorphous bodies.* Dover Publications, Inc. (1994).
- [Gün96] T. GÜNZEL. *Comparison of different diffractometer types* (1996). ESRF Experiments Division Programming Group - internal report.
- [Har67] K. HARUTA. *Intensity of X-rays Diffracted from an Elastic Vibrating Single-Crystal.* J.Appl.Phys. **38**(8), p. 3312–3316 (1967).
- [HB94] V. HOLÝ and T. BAUMBACH. *Nonspecular x-ray reflection from rough multilayers.* Phys. Rev. B **49**(15), p. 10668–10676 (1994).
- [HC89] M.-P. HOUNG and Y.-C. CHANG. *Electronic Structure of $\text{In}_{1-x}\text{Ga}_x\text{As} - \text{InP}$ strained-layer quantum wells.* J.Appl.Phys. **65**(8), p. 3096–3100 (1989).
- [HDV99] X. HUANG, M. DUDLEY, W. VETTER, W. HUANG, S. WANG, and C. CARTER. *Direct evidence of micropipe-related pure superscrew dislocations in SiC.* Appl.Phys.Lett. **74**(3) (1999).

- [HKS91] J.-I. HASHIMOTO, T. KATSUYAMA, J. SHINKAI, I. YOSHIDA, and H. HAYASHI. *Effects of strained-layer strcutres on the threshold current density of AlGaInP/GaInP visible lasers.* Appl.Phys.Lett. **58**(9), p. 879–880 (1991).
- [HM96] V. HOLÝ and P. MIKULÍK. *Theoretical description of multiple crystal arrangements.* In Authier et al. [ALT96].
- [HPB98] V. HOLÝ, U. PIETSCH, and T. BAUMBACH. *High Resolution X-Ray Scattering from Thin Films and Multilayers .* Volume 149 of *Springer Tracts in Modern Physics*. Springer (1998).
- [HTK93] V. HOLÝ, L. TAPFER, E. KOPPENSTEINER, G. BAUER, H. LAGE, O. BRANDT, and K. PLOOG. *Triple crystal x-ray diffractometry of periodic arrays of semiconductor quantum wires.* Appl.Phys.Lett. **63**(23), p. 3140–3142 (1993).
- [HY99] W. HAMILTON and M. YETHIRAJ. *Effects of traveling surface acoustic waves on neutron Bragg scattering from perfect crystals.* Phys. Rev. B **59**(5), p. 3388–3392 (1999).
- [Jac98] K. A. JACKSON, editor. *Compound Semiconductor Devices - Structures and Processing.* Wiley-VCH (1998).
- [Jan97] P. A. JANSSON. *Deconvolution of Images and Spectra.* Academic Press (1997).
- [JHA95] S. JAIN, A. HARKER, A. ATKINSON, and K. PINARDI. *Edge-induced stress and strain in stripe films and substrates: A two-dimensional finite element calculation.* J.Appl.Phys. **78**(3), p. 1630–1637 (1995).
- [JK88] B. JENICHEN and R. KÖHLER. *Deformationen in LEC-GaAs.* Proceedings of RöTo 1988, Clausthal (Germany) p. 132–142 (1988).
- [Kel95] M. KELLY. *Low-dimensional semiconductors. Materials, physics, technology, devices.* Oxford University Press 3 edition (1995).
- [KPW67] A. KLEIN, P. PRAGER, H. WAGENFELD, P. ELLIS, and T. SABINE. *Diffraction of neutrons and X-rays by a vibrating quartz crystal.* Appl.Phys.Lett. **10**(10), p. 293–295 (1967).
- [Kur67] M. KURIYAMA. *Theory of X-ray Diffraction by a Distorted Crystal.* J.Phys.Soc.Japan **23**(6), p. 1369–1379 (1967).
- [Lan58] A. LANG. J.Appl.Phys. **29**, p. 597 (1958).
- [Lan59] A. LANG. *The projection topography: A new method in X-Ray Diffraction Microradiography.* Acta Cryst. **12**, p. 249 (1959).
- [Lan78] A. LANG. *Techniques and Interpretation in X-ray Topography.* In *Diffraction and Imaging Techniques in Material Science* p. 623. North-Holland (1978).
- [Lau31] M. v. LAUE. *Die dynamische Theorie der Röntgenstrahlinterferenzen in neuer Form.* Ergeb.Exakt.Naturwiss. **10**, p. 133–158 (1931).
- [LBG99] D. LÜBBERT, T. BAUMBACH, and C. GIANNINI. *X-ray diffraction analysis of strain-induced patterning in superlattices grown on vicinal surfaces - experiment and simulation.* (1999).
- [LBH00] D. LÜBBERT, T. BAUMBACH, J. HÄRTWIG, E. BOLLER, and E. PERNOT. *μ m-resolved high resolution X-ray diffraction imaging for semiconductor quality control.* Nucl. Instr. Meth. B **160**(4), p. 521–527 (2000).
- [LBP99] D. LÜBBERT, T. BAUMBACH, S. PONTI, U. PIETSCH, L. LEPRINCE, J. SCHNECK, and A. TALNEAU. *Strain investigation of low strained buried gratings by grazing incidence X-ray diffraction and elasticity theory.* Europhys.Lett. **46**(4), p. 479–485 (1999).

- [LBT97] L. LEPRINCE, T. BAUMBACH, A. TALNEAU, M. GAILHANOU, and J. SCHNECK. *Observation of strain relaxation phenomena in buried and non buried III-V surface gratings through high resolution x-ray diffraction.* Appl.Phys.Lett. **71**(22), p. 3227–3229 (1997).
- [LCC98] S. LAGOMARSINO, A. CEDOLA, P. CLOETENS, S. DI FONZO, W. JARK, and G. SOULLIÉ. *Phase contrast hard X-ray microscopy with submicron resolution.* Appl.Phys.Lett. **71**(13), p. 2557–2559 (1998).
- [Lel55] J. LELY. Ber.Deut.Keram.Ges. **32**, p. 229 (1955).
- [LGC89] C. LUCAS, E. GARTSTEIN, and R. COWLEY. *The Resolution Function of an X-ray Triple-Crystal-Diffractometer: Comparison of Experiment and Theory.* Acta Cryst. A **45**, p. 416–422 (1989).
- [LHH90] J. LEE, K. HSIEH, Y. HWANG, and R. KOLBAS. *Stimulated emission from monolayer-thick Al_xGa_{1-x}As – GaAs single quantum well heterostructures.* Appl.Phys.Lett. **56**(7), p. 626–628 (1990).
- [LJB99] D. LÜBBERT, B. JENICHEN, T. BAUMBACH, H. GRAHN, G. PARIS, A. MAZUELAS, T. KOJIMA, and S. ARAI. *Elastic stress relaxation in GaInAsP quantum wires in InP.* J.Phys.D:Appl.Phys. **32**, p. A21–A25 (1999).
- [LL86] L. LANDAU and E. LIFSHITZ. *Theory of elasticity.* Pergamon Press (1986).
- [LSPvB96] J.-C. LABICHE, J. SEGURA-PUCHADES, D. VAN BRUSSEL, and J. MOY. *FRELON Camera: Fast REadout LOw Noise.* ESRF Newsletter **25**, p. 41–43 (1996).
- [LTV90] J. A. LEBENS, C. S. TSAI, and K. J. VAHALA. *Application of selective epitaxy to fabrication of nanometer scale wire and dot structures.* Appl.Phys.Lett. **56**(26), p. 2642–2644 (1990).
- [Lüb96] D. LÜBBERT. *Anwendungen systemtheoretischer Verallgemeinerungen von Algorithmen der Gitterfeldtheorie.* Diploma thesis Universität Hamburg (1996).
- [LV93] M. LOHMEIER and E. VLIEG. *Angle Calculations for a Six-Circle Surface X-ray Diffractometer.* J.Appl.Cryst. **26**, p. 706–716 (1993).
- [Man98] L. MANCINI. *Etude des défauts dans les quasicristaux en utilisant les aspects nouveaux de l'imagerie aux rayons X associés aux sources synchrotron de troisième génération.* PhD thesis Université Joseph Fourier, Grenoble, France (1998).
- [MB74] J. MATHEWS and A. BLAKESLEE. Journal of Crystal Growth **27**, p. 118 (1974).
- [McM45] E. McMILLAN. Phys.Rev. **68**, p. 143 (1945).
- [MEC79] W. MARRA, P. EISENBERGER, and A. CHO. J.Appl.Phys. **50**, p. 6927 (1979).
- [Mik97] P. MIKULÍK. *X-ray reflectivity from planar and structured multilayers.* PhD thesis Université Joseph Fourier, Grenoble, France (1997).
- [Mik98] P. MIKULÍK. *Program xtrace* (1998).
- [Mil99] S. MILITA. *Etude par imagerie au rayonnement synchrotron de matériaux semi-conducteurs (Si poreux et SiC).* PhD thesis Université Joseph Fourier, Grenoble, France (1999).
- [MMH97] A. MAZUELAS, S. MILITA, J. HÄRTWIG, J. BARUCHEL, T. BAUMBACH, J. FROUIN, and B. CAPELLE. *High resolution diffraction and imaging in a new diffractometer for synchrotron radiation.* In A. YAVARI, editor, *Proceedings of the “Meeting of the French-Spanish Group on new materials”.* (1997).

- [Moc88] S. MOCHRIE. *Four-Circle Angle Calculations for Surface Diffraction*. *J.Appl.Cryst.* **21**, p. 1–3 (1988).
- [Moc99] V. MOCELLA. *Cohérence d'un faisceau synchrotron et théorie dynamique de la diffraction: simulations et expériences*. PhD thesis Université Joseph Fourier, Grenoble, France (1999).
- [MS90] A. MACRANDER and S. SLUSKY. *X-ray diffraction from corrugated crystalline surfaces and interfaces*. *Appl.Phys.Lett.* **56**(5), p. 443–445 (1990).
- [NBB99] G. NASH, S. BENDING, M. BOERO, M. RIEK, and K. EBERL. *Surface-acoustic-wave absorption by quantum-dot arrays*. *Phys. Rev. B* **59**(11), p. 7649–7655 (1999).
- [Nel63] H. NELSON. *RCA Review* **24**, p. 603–626 (1963).
- [NHW95] M. NOTOMI, J. HAMMERSBERG, H. WEMAN, S. NOJIMA, H. SUGIURA, M. OKAMOTO, T. TAMAMURA, and M. POTEMSKI. *Dimensionality effects on strain and quantum confinement in lattice-mismatched $InAs_xP_{1-x}/InP$ quantum wires*. *Phys. Rev. B* **52**(15), p. 11147–11158 (1995).
- [Nye95] J. NYE. *Physical Properties of Crystals. Their Representation by Tensors and Matrices*. Oxford University Press (1995).
- [PB99] S. PONTI and T. BAUMBACH. *Non-uniform strain in epitaxial surface gratings: Beyond the ordinary elastic description*. *Phys.Lett. A* **251**(1), p. 61–66 (1999).
- [Pea82] T. PEARSALL. *InGaAsP alloy semiconductors*. John Wiley & Sons (1982).
- [Pfe99] F. PFEIFFER. *X-ray waveguides*. Diploma thesis Ludwig-Maximilians-Universität München (1999).
- [Pin78] Z. PINSKER. *Springer series in solid-state sciences*. In M. CARDONA, P. FULDE, and H. QUEISSER, editors, *Dynamical scattering of X-rays in crystals*. Volume 3. Springer Verlag 6 edition (1978).
- [PMR93] U. PIETSCH, H. METZGER, S. RUGEL, B. JENICHEN, and I. ROBINSON. *Depth-resolved measurement of lattice relaxation in $Ga_{1-x}In_xAs/GaAs$ strained layer superlattices by means of grazing-incidence x-ray diffraction*. *J.Appl.Phys.* **74**(4), p. 2381–2387 (1993).
- [PTV95] W. H. PRESS, S. A. TEUKOSKY, W. T. VETTERLING, and B. P. FLANNERY. *Numerical Recipes in C: The Art of Scientific Programming*. Cambridge University Press 2nd edition (1995).
- [PWS89] L. PFEIFFER, K. WEST, H. STORMER, and K. BALDWIN. *Electron mobilities exceeding $10^7 \text{ cm}^2/\text{Vs}$ in modulation-doped GaAs*. *Appl.Phys.Lett.* **55**(18), p. 1888–1890 (1989).
- [Que77] H.-J. QUEISSER, editor. *X-ray Optics*. Volume 22 of *Topics in Applied Physics*. Springer (1977).
- [Rao93] D. RAOUX. *Introduction to synchrotron radiation and the physics of storage rings*. In *Neutron and synchrotron radiation for condensed matter studies*. Volume 1. Les Editions de Physique - Springer Verlag (1993).
- [RB93] D. ROSHCHUPKIN and M. BRUNEL. *Time modulation of an x-ray beam by surface acoustic waves*. *Rev. Sci. Instr.* **64**(2), p. 379–382 (1993).
- [RBdB92] D. ROSHCHUPKIN, M. BRUNEL, F. DE BERGEVIN, and A. ERKO. *X-ray space modulation by diffraction on an ultrasonic superlattice*. *Nucl. Instr. Meth. B* **72**, p. 471–476 (1992).
- [Rob86] I. ROBINSON. *Crystal truncation rods and surface roughness*. *Phys. Rev. B* **33**(6), p. 3830–3836 (1986).

- [RTM98] D. ROSHCHUPKIN, R. TUCOULOU, A. MASCLET, M. BRUNEL, I. SCHELOKOV, and A. KONDAKOV. *X-ray diffraction by standing surface acoustic waves*. Nucl. Instr. Meth. B **142**, p. 432–436 (1998).
- [RVG95] G. RENAUD, B. VILLETTÉ, and P. GUÉNARD. *Apparatus for 3D surface X-ray scattering during in situ molecular beam deposition*. Nucl. Instr. Meth. B **95**, p. 422–430 (1995).
- [RZW97] C. ROCKE, S. ZIMMERMANN, A. WIXFORTH, J. KOTTHAUS, G. BÖHM, and G. WEIZMANN. *Acoustically Driven Storage of Light in a Quantum Well*. Phys. Rev. Lett. **78**(21), p. 4099–4102 (1997).
- [Sau99] W. SAUER. *Abbildende und nichtabbildende Röntgenbeugung an Galliumarsenid bei Anregung von Oberflächenwellen*. PhD thesis Ludwig-Maximilians-Universität, Kiel, Germany (1999).
- [SK97] Q. SHEN and S. KYCIA. *Determination of interfacial strain distribution in quantum-wire structures by synchrotron x-ray scattering*. Phys. Rev. B **55**(23), p. 15791–15797 (1997).
- [SKP98] M. STRASSBURG, V. KUTZER, U. POHL, A. HOFFMANN, I. BROSER, N. LEDENTSOV, D. BIMBERG, A. ROSENAUER, U. FISCHER, D. GERTHSEN, I. KRESTNIKOV, M. MAXIMOV, P. KOP’EV, and Z. I. ALFEROV. *Gain studies of (Cd, Zn)Se quantum islands in a ZnSe matrix*. Appl.Phys.Lett. **72**(8), p. 942–944 (1998).
- [SKS96] A. SNIGIREV, V. KOHN, I. SNIGIREVA, and B. LENGELE. *A compound refractive lens for focusing high-energy X-rays*. Nature **384**, p. 49 (1996).
- [SKT96] Q. SHEN, S. W. KYCIA, E. TENTARELLI, W. SCHAFF, and L. EASTMAN. *X-ray-diffraction study of size-dependent strain in quantum-wire structures*. Phys. Rev. B **54**(23), p. 16381–16384 (1996).
- [SL97] J. SCHNECK and L. LEPRINCE. *Personal communication*. (1997).
- [SRJ98] P. SANTOS, M. RAMSTEINER, and F. JUNGNICKEL. *Spatially resolved photoluminescence in GaAs surface acoustic wave structures*. Appl.Phys.Lett. **72**(17), p. 2099–2101 (1998).
- [SSG88] S. SINHA, E. SIROTA, S. GAROFF, and H. STANLEY. *X-ray and neutron scattering from rough surfaces*. Phys. Rev. B **38**(4), p. 2297–2311 (1988).
- [SSM99] W. SAUER, M. STREIBL, T. METZGER, A. HAUBRICH, S. MANUS, W. A., J. PEISL, J. MAZUELAS, J. HÄRTWIG, and J. BARUCHEL. *X-ray imaging and diffraction from surface phonons on GaAs*. Appl.Phys.Lett. **75**(12), p. 1709–1711 (1999).
- [SUW93] Q. SHEN, C. UMBACH, B. WESELAK, and J. BLAKELY. *X-ray diffraction from a coherently illuminated Si(001) grating surface*. Phys. Rev. B **48**(24), p. 17967–17971 (1993).
- [SUW96] Q. SHEN, C. UMBACH, B. WESELAK, and J. BLAKELY. *Lateral correlation in mesoscopic structures on the silicon (001) surface determined by grating x-ray diffuse scattering*. Phys. Rev. B **53**(8), p. R4237–R4240 (1996).
- [Tak62] S. TAKAGI. *Dynamical theory of diffraction applicable to crystals with any kind of small distortion*. Acta Cryst. **15**, p. 1311–1312 (1962).
- [Tak69] S. TAKAGI. *A Dynamical Theory of Diffraction for a Distorted Crystal*. J.Phys.Soc.Jpn **26**(5), p. 1239–1253 (1969).
- [Tau64] D. TAUPIN. *Théorie dynamique de la diffraction des rayons X par les cristaux déformés*. Bull.Soc.Franc.Minér.Crist. **87**, p. 469–511 (1964).

- [TBR98] R. TUCOULOU, M. BRUNEL, D. ROSHCHUPKIN, and I. SCHELOKOV. *One and two dimensional space scannings of x-ray beams by diffraction on surface acoustic waves: Application to x-ray imaging*. Rev.Sci.Instr. **69**(7), p. 2704–2707 (1998).
- [TG87] S. P. TIMOSHENKO and J. GOODIER. *Theory of Elasticity*. McGraw-Hill (1987).
- [TG90] L. TAPFER and P. GRAMBOW. *X-ray Bragg Diffraction on Periodic Surface Gratings*. Appl. Phys. A **50**, p. 3–6 (1990).
- [TKB92] M. TOLAN, G. KÖNIG, L. BRÜGEMANN, W. PRESS, F. BRINKOP, and J. KOTTHAUS. *X-Ray Diffraction from Laterally Structured Surfaces: Total External Reflection and Grating Truncation Rods*. Europhys.Lett. **20**(3), p. 223–228 (1992).
- [TLRL92] L. TAPFER, G. LA ROCCA, H. LAGE, R. CINGOLANI, P. GRAMBOW, A. FISCHER, D. HEITMANN, and K. PLOOG. *Observation and analysis of quantum wire structures by high-resolution X-ray diffraction*. Surface Science **267**, p. 227–231 (1992).
- [TMY92] I.-H. TAN, R. MIRIN, T. YASUDA, E. L. HU, H. BOWERS, C. B. PRATER, P. K. HANSMA, M. Y. HE, and A. G. EVANS. *Study of partial strain relase and surface states formed on the sidewall of InGaAs quantum-well wires*. J.Vac.Sci.Technol.B **10**(4), p. 1971–1974 (1992).
- [Tol93] M. TOLAN. *Röntgenbeugung an strukturierten Oberflächen - Experiment & Theorie*. PhD thesis Christian-Albrechts-Universität, Kiel, Germany (1993).
- [TPB94] M. TOLAN, W. PRESS, F. BRINKOP, and J. KOTTHAUS. *X-ray diffraction from laterally structured surfaces: Crystal truncation rods*. J.Appl.Phys. **75**(12), p. 7761–7769 (1994).
- [TPB95] M. TOLAN, W. PRESS, F. BRINKOP, and J. KOTTHAUS. *X-ray diffraction from laterally structured surfaces: Total external reflection*. Phys. Rev. B **51**(4), p. 2239–2251 (1995).
- [TSDC95] L. TAPFER, P. SCIACOVELLI, and L. DE CARO. *Double- and triple-crystal X-ray diffraction analysis of semiconductor quantum wires*. J.Phys.D:Appl.Phys. **28**(7), p. A179 (1995).
- [TT78] Y. TAIROV and V. TSVETKOV. J.Crystal Growth **43**, p. 209 (1978).
- [Tuc99] R. TUCOULOU. *Personal communication*. (1999).
- [Vek45] V. VEKSLER. J.Phys. (U.S.S.R.) **9**, p. 153 (1945).
- [Vin21] G. H. VINEYARD. *Die Konstitution der Mischkristalle und die Raumfüllung der Atome*. Z. Phys. **5**, p. 17 (1921).
- [Vin82] G. H. VINEYARD. *Grazing incidence diffraction and the distorted-wave approximation for the study of surfaces*. Phys. Rev. B **26**(8), p. 4146–4159 (1982).
- [vL60] M. VON LAUE. *Röntgenstrahlinterferenzen*. Akademische Verlagsgesellschaft 3 edition (1960).
- [Vli98] E. VLIEG. *A (2+3)-Type Surface Diffractometer: Mergence of the z-Axis and (2+2)-Type Geometries*. J.Appl.Cryst. **31**, p. 198–203 (1998).
- [VVdVM87] E. VLIEG, J. VAN DER VEEN, J. MACDONALD, and M. MILLER. *Angle Calculations for a Five-Circle Diffractometer Used for Surface X-ray Diffraction*. J.Appl.Cryst. **20**, p. 330–337 (1987).
- [War90] B. WARREN. *X-ray diffraction*. Dover Publications, Inc. (1990).
- [WGT82] R. WHATMORE, P. GODDARD, B. TANNER, and G. CLARK. *Direct imaging of travelling Rayleigh waves by stroboscopic X-ray topography*. Nature **299**, p. 44–46 (1982).

-
- [WHW99] O. WADA, H. HASEGAWA, and C. WADA. *InP-Based Materials and Devices: Physics and Technology*. John Wiley & Sons (1999).
- [Wil95] A. WILSON, editor. *International Tables for Crystallography*. Volume A. Kluwer Academic Publishers (1995).
- [Wil96] K. WILLE. *Physik der Teilchenbeschleuniger und Synchrotronstrahlungsquellen*. Teubner, Stuttgart 2. edition (1996).
- [Yar88] A. YARIV. *Scaling law and minimum threshold currents for quantum-confined semiconductor lasers*. Appl.Phys.Lett. **53**(12), p. 1033–1035 (1988).
- [YMW79] J. YOSHIMURA, T. MIYAZAKI, T. WADA, and K. KOHRA. *Measurement of local variations in spacing and orientation of lattice plane of synthetic quartz*. J.Cryst.Growth **46**, p. 691–700 (1979).
- [Zac94] W. H. ZACHARIASEN. *Theory of X-ray Diffraction in Crystals*. Dover Publications, Inc. (1994).
- [ZBG99] U. ZEIMER, T. BAUMBACH, J. GRENZER, D. LÜBBERT, A. MAZUELAS, U. PIETSCH, and G. ERBERT. *In-situ characterization of strain distribution in broad area high power lasers under operation by high resolution X-ray diffraction and topography using synchrotron radiation*. J.Phys.D:Appl.Phys. **32**, p. A123–A127 (1999).
- [Zon95] F. ZONTONE. *Imagerie par diffraction (“topographie”) à l’installation européenne de rayonnement synchrotron (“ESRF”): Ligne de lumière, possibilités et premières expériences*. PhD thesis Université Joseph Fourier, Grenoble, France (1995).
- [ZPB97] K. ZHURAVLEV, D. PETROV, Y. B. BOLKHOVITYANOV, and N. RUDAJA. *Effect of surface acoustic waves on low-temperature photoluminescence of GaAs*. Appl.Phys.Lett. **70**(25), p. 3389–3391 (1997).
- [ZSS98] E. ZOLOTOYABKO, D. SHILO, W. SAUER, E. PERNOT, and J. BARUCHEL. *Visualization of 10µm surface acoustic waves by stroboscopic X-ray topography*. Appl.Phys.Lett. **73**(16), p. 2278–2280 (1998).
- [ZT87] O. ZIENKIEWICZ and R. TAYLOR. *The finite element method*. McGraw-Hill (1987).

List of publications

Parts of this work have been published previously in the following articles:

Main publications

roughly sorted by decreasing relevance:

- D. Lübbert, T. Baumbach, S. Ponti, U. Pietsch, L. Leprince, J. Schneck, and A. Talneau. *Strain investigation of low strained buried gratings by grazing incidence X-ray diffraction and elasticity theory.* Europhys.Lett. **46**(4), p. 479–485 (1999).
- T. Baumbach and D. Lübbert. *Grazing incidence diffraction by laterally patterned semiconductor nanostructures.* J.Phys.D:Appl.Phys. **32**, p. 726–740 (1999).
- D. Lübbert, T. Baumbach, J. Härtwig, E. Boller, and E. Pernot. *μm-resolved high resolution X-ray diffraction imaging for semiconductor quality control.* accepted for publication in Nucl. Instr. Meth. B (1999).
- G. T. Baumbach, D. Lübbert, and M. Gailhanou. *X-ray structure investigation of lateral surface nano-structures - a full quantitative analysis of non-uniform lattice strain.* J.Phys.D:Appl.Phys. **32**, p. A208–A211 (1999).
- T. Baumbach, D. Lübbert, and M. Gailhanou. *Strain relaxation in surface nanostructures studied by X-ray diffraction methods.* accepted for publication in Jap.J.Appl.Phys. **38**(12A) (1999).
- D. Lübbert, B. Jenichen, T. Baumbach, H. Grahn, G. Paris, A. Mazuelas, T. Kojima, and S. Arai. *Elastic stress relaxation in GaInAsP quantum wires in InP.* J.Phys.D:Appl.Phys. **32**, p. A21–A25 (1999).
- T. Baumbach, D. Lübbert, and M. Gailhanou. *Strain and shape analysis of multilayer surface gratings by coplanar and by grazing incidence X-ray diffraction.* submitted to J.Appl.Phys (1999).
- G. T. Baumbach, C. Giannini, D. Lübbert, R. Felici, L. Tapfer, T. Marschner, and W. Stolz. *Investigation of Strain Induced Patterning in Superlattices by Grazing Incidence Diffraction - Comparison of Morphological and Strain Ordering.* J.Phys.D:Appl.Phys. **32**, p. A212–A215 (1999).
- C. Giannini, T. Baumbach, D. Lübbert, R. Felici, L. Tapfer, W. Marschner, T. Stolz, N. Jin-Phillipp, and J. Phillip. *Strain-driven transition from stepped interface to regularly spaced macrosteps in (GaIn)As/Ga(AsP) symmetrically strained superlattices.* submitted to Phys. Rev. **B** (1999).
- U. Zeimer, T. Baumbach, J. Grenzer, D. Lübbert, A. Mazuelas, U. Pietsch, and G. Erbert. *In-situ characterization of strain distribution in broad area high power lasers under operation by high resolution X-ray diffraction and topography using synchrotron radiation.* J.Phys.D:Appl.Phys. **32**, p. A123–A127 (1999).
- T. Baumbach, D. Lübbert, and M. Gailhanou. *Strain relaxation in surface nano-structures studied by X-ray diffraction methods.* Proceedings of the EMRS 1999 spring meeting (1999).

- D. Lübbert, T. Baumbach, J. Härtwig, E. Boller, and E. Pernot. *Wafer quality imaging by μ m-resolved high resolution X-ray diffraction*. Proceedings of the EMRS 1999 spring meeting (1999).
- G. T. Baumbach, D. Lübbert, U. Pietsch, N. Darowski, L. Leprince, A. Talneau, and J. Schneck. *Grazing incidence diffraction by epitaxial multilayered gratings*. Physica B **248**, p. 343–348 (1998).

Publications resulting from collaborations

- V. Holý, A. Darhuber, J. Stangl, S. Zerlauth, F. Schäffler, G. Bauer, N. Darowski, D. Lübbert, U. Pietsch, and I. Vávra. *Coplanar and grazing incidence x-ray diffraction investigation of self-organized SiGe quantum dot multilayers*. Phys. Rev. B **58**(12), p. 7934–7943 (1998).
- N. Darowski, U. Pietsch, Y. Zhuang, S. Zerlauth, G. Bauer, D. Lübbert, and T. Baumbach. *In-plane strain and strain relaxation in laterally patterned periodic arrays of Si/SiGe quantum wires and dot arrays*. Appl.Phys.Lett. **73**(6), p. 806–808 (1998).
- N. Darowski, K. Paschke, U. Pietsch, K. Wang, A. Forchel, D. Lübbert, and T. Baumbach. *Structural characterisation of a GaAs surface wire structure by triple axis X-ray grazing incidence diffraction*. Physica B **248**, p. 104–108 (1998).
- V. Holý, J. Stangl, S. Zerlauth, G. Bauer, N. Darowski, D. Lübbert, and U. Pietsch. *Lateral arrangement of self-assembled quantum dots in an SiGe/Si superlattice*. J.Phys.D:Appl.Phys. **32**, p. A234–A238 (1999).
- Y. Zhuang, V. Holý, J. Stangl, A. Darhuber, F. Schäffler, G. Bauer, N. Darowski, D. Lübbert, and U. Pietsch. *Strain relaxation in periodic arrays of Si/SiGe quantum wires determined by coplanar high-resolution x-ray diffraction and grazing incidence diffraction*. J.Phys.D:Appl.Phys. **32**, p. A224–A229 (1999).
- D. Buttard, J. Eymery, F. Rieutord, F. Fournel, D. Lübbert, T. Baumbach, and H. Moriceau. *Grazing incidence X-ray studies of twist-bonded Si/Si and Si/SiO₂ interfaces*. Proceedings of the Sixth International Conference on Surface X-ray and Neutron Scattering (6SNXS) (1999).

Internal Reports

- T. Baumbach, C. Giannini, D. Lübbert, R. Felici, L. Tapfer, T. Marschner, and W. Stolz. *Strain-induced patterning in superlattices - comparison of morphological ordering and strain ordering*. ESRF Highlights p. 87–88 (1998).
- D. Lübbert, T. Baumbach, L. Leprince, J. Schneck, A. Talneau, and R. Felici. *Residual strain in buried and non-buried semiconductor nanostructures*. ESRF Highlights p. 86–87 (1998).

List of abbreviations

AFM	Atomic force microscopy
AXRD	Asymmetric X-ray diffraction
BA	Born approximation
CBE	Chemical beam epitaxy
CTR	Crystal (or: central) truncation rod
DCD	Double-crystal diffractometry / diffractometer
DWBA	Distorted wave Born approximation
EPFL	Ecole polytechnique fédérale de Lausanne (CH)
FEM	Finite element method
FT	Fourier transform
GID	Grazing incidence diffraction
GTR	Grating truncation rod
LEC	Liquid encapsulated Czochralsky
MBE	Molecular beam epitaxy
MCA	Multi-channel analyzer
ML	Multilayer
MOCVD	Metal-organic chemical vapour deposition
PDE	Partial differential equation
PL	Photo-luminescence
PSD	Position-sensitive detector
RLP	Reciprocal lattice point
RSM	Reciprocal space map
SAW	Surface acoustic waves
SEM	Scanning electron microscopy
SL	Superlattice
SG	Surface grating
TCD	Triple-crystal diffractometry / diffractometer
TEM	Transmission electron microscopy
TRXF	Total reflection X-ray fluorescence
XRD	X-ray diffraction
XRR	X-ray reflectivity

List of important symbols

b	top width of a surface grating
D_{SG}	Lateral period of a surface grating
D_{SL}	Vertical period of a superlattice
d	interplanar lattice spacing
f_n	atomic form factor of the n -th atom in the unit cell
g	“groove path” (valley width) of a surface grating
$\mathbf{K}_i, \mathbf{k}_i$	wave vector of the incident wave in vacuum and in the crystal
$\mathbf{K}_f, \mathbf{k}_f$	wave vector of the exit wave in vacuum and in the crystal
$H = \frac{2\pi}{D_{SG}}$	Distance in reciprocal space between neighbouring grating
$\mathbf{h} = \frac{2\pi}{d}(H, K, L)$	truncation rods of a surface grating
P	reciprocal lattice vector
p_l, p_r	polarization factor
$\mathbf{Q} = \mathbf{K}_f - \mathbf{K}_i$	left and right sidewall slope ($\frac{dz}{dx}$) of a surface grating
$\mathbf{q} = \mathbf{Q} - \mathbf{h}$	Scattering vector (momentum transfer)
$r_e = \frac{e^2}{4\pi\epsilon_0 mc^2}$	Reduced scattering vector, i.e. distance between actual scattering vector and the nearest reciprocal lattice point \mathbf{h}
V	classical electron radius
$\Gamma = \frac{r_e \lambda^2}{\pi V}$	volume of unit cell of the crystal lattice
ϑ_B	proportionality factor between <i>Fourier coefficients</i> of charge density and dielectric constant
λ	exact Bragg angle
μ_0	wavelength
ϕ	linear absorption coefficient
$\rho(\mathbf{r})$	angle between scattering vector \mathbf{Q} and the sample's surface normal \mathbf{n}
	electron density

Acknowledgements

It is a great pleasure to thank Tilo Baumbach for the initial stimulation to choose this challenging topic as a thesis subject, for his constant support and for the time and energy that he invested in countless fruitful discussions. His enthusiasm, cooperative working style and open-mindedness contributed to making the last three years a very pleasant time. His vivid interest in all aspects of X-ray physics as well as his extraordinary skills in motivating colleagues and collaborators leave a deep impression.

Furthermore, I am indebted to Ullrich Pietsch, who as the academic supervisor contributed with many challenging questions and good ideas to this thesis. Moreover, he introduced me to the experimental techniques in a series of common measurements at HASYLAB, and also provided me with the possibility to give several talks in Potsdam as well as in very attractive surroundings in Smolenice (Slovakia).

I would also like to express my gratitude to Prof. Werner Press and Prof. Michel Schlenker, who have accepted the task to judge this manuscript.

Thanks are due to the ESRF, which hosted me on its site for three years, and in particular to two beamlines: Fabio Comin and Roberto Felici (ID32), who provided me with an office in the initial stages of this work, and most of all José Baruchel, who gave me a permanent home on the ID19 beamline and in his group. I will remember his remarkable talent in creating a good working climate.

I would also like to thank the whole ID19 staff, not only Jürgen Härtwig for being an indefatigable teacher of dynamical theory, but also all other members of the beamline (whom I will not mention individually just for fear to forget someone) for being helpful and pleasant colleagues.

The Fraunhofer-Institute for Nondestructive Testing (Izfp, Saarbrücken and Dresden) has made this thesis possible via a grant from the *Ministerium für Bildung, Kultur und Wissenschaft des Saarlandes*, and has generously financed my trips to various conferences and X-ray schools during the last three years.

I have profited quite a lot from the collaboration and the common beam times with Petr Mikulík, Marc Gailhanou, Nora Darowski, Cinzia Giannini, Jacques Schneck and Laurent Leprince, Bernd Jenichen, and Ute Zeimer. The discussions and exchange with them about experimental strategies and simulation issues were very stimulating.

Finally, I would like to express my gratitude to all those who have done some of the proofreading of this manuscript: Lina Aruta, Claudio Ferrero, Marc Gailhanou, Jürgen Härtwig, Lukas Helfen, Rolf Kilian, Petr Mikulík, Jean-Marc Petit, Ute Ramseger, and Metin Tolan. And to my most arduous proofreader - to Steffi, *sine qua non*.

Thesen

zur Dissertation mit dem Thema

Strain and Lattice Distortion in Semiconductor Structures: a Synchrotron Radiation Study

vorgelegt von DANIEL LÜBBERT

1. Röntgenbeugung unter Einsatz von Synchrotronstrahlung ermöglicht eine umfassende Charakterisierung von Halbleiterstrukturen.
2. Die Anwendung auf Halbleiter-Oberflächengitter und Quantendrähte ergibt repräsentative Informationen über die geometrische Form der Probe ebenso wie über ihre kristallinen Eigenschaften. Für eine vollständige Untersuchung ist i.a. die Aufnahme der zweidimensionalen Intensitätsverteilung im reziproken Raum (sog. *reciprocal space maps*) in der Umgebung mehrerer reziproker Gitterpunkte erforderlich.
3. Der Einfluss der Proben-Form auf das Beugungsbild ist an allen reziproken Gitterpunkten (Bragg-Reflexen) derselbe. Im Fall von Gittern mit Trapezform ist jeder Bragg-Reflex von einem charakteristischen kreuzförmigen Beugungsmuster umgeben.
4. Der Einfluss der Verzerrung des Kristallgitters (*strain*) auf das Beugungsbild unterscheidet sich hingegen von einem reziproken Gitterpunkt zum nächsten. Die einzelnen Bragg-Reflexe sind empfindlich für verschiedene Komponenten des *strain*-Feldes. Im Fall der Oberflächengitter bewirkt der Einfluss des *strain*-Feldes eine deutliche Abweichung der experimentell messbaren Beugungsbilder vom theoretischen Kreuz-Muster.
5. Die experimentellen Beugungsbilder können erklärt werden durch ein theoretisches Simulationsverfahren, das auf der Kombination einer semi-kinematischen Theorie der Röntgenbeugung mit Kontinuums-Elastizitätstheorie beruht. Durch die sehr gute Übereinstimmung von Experiment und Simulation kann nachgewiesen werden, dass makroskopische Elastizitätstheorie noch anwendbar ist zur Berechnung des *strain*-Feldes in Halbleiter-Nanostrukturen von nur einigen 10 – 100 nm linearer Ausdehnung.
6. Durch quantitative Auswertung der Intensitäts-Profile entlang der *grating truncation rods* an mehreren reziproken Gitterpunkten lassen sich sämtliche Komponenten ϵ_{ij} des *strain*-Feldes charakterisieren.
7. Das vollständige *strain*-Feld in Oberflächengittern, die durch (1) epitaktisches Wachstum und (2) chemisches Ätzen hergestellt werden, beruht auf drei Anteilen: erstens der gleichförmigen Verzerrung, die beim epitaktischen Aufwachsen einer planaren Schicht auf ein Substrat entsteht; zweitens der Relaxation dieser Verzerrung aufgrund des Ätzprozesses; drittens der teilweisen Umkehrung dieser Relaxation beim Überwachsen des Oberflächengitters mit einer Deckschicht.
8. Die Einflüsse von Gitterform und *strain* auf das Beugungsbild können voneinander getrennt werden durch eine Messung mit Röntgenbeugung unter streifendem Einfall (*grazing incidence diffraction*, GID). Auf diese Art kann die Gitterform im Experiment isoliert und unabhängig vom *strain*-Einfluss untersucht werden.

9. Des weiteren kann mit GID zusätzlich Tiefenselektivität erzielt werden. Auf diese Weise können auch vergrabene Strukturen zerstörungsfrei untersucht sowie der Verlauf des Verspannungsfeldes von der vergrabenen strukturierten Region bis hinauf zur Probenoberfläche nachgewiesen werden.
 10. GID erzielt (Tiefen-)Auflösung im *Ortsraum*, während konventionelle Röntgenbeugungsmethoden die Beiträge von verschiedenen Schichten der Probe im *reziproken Raum* trennen.
-
11. Röntgenbeugung mit zusätzlicher lateraler Ortsauflösung im Bereich von Mikrometern kann verwirklicht werden durch eine Kombination von Röntgen-Diffraktometrie und -Topographie. Der Einsatz von Synchrotronstrahlung ermöglicht dies durch die hohe Intensität, die hohe Parallelität und den grossen Querschnitt des einfallenden Röntgenstrahls, sowie durch die μm -aufgelöste, parallele Detektion der gebeugten Intensitäten mit Hilfe einer digitalen Kamera.
 12. Das breite Wellenlängenspektrum der Synchrotronstrahlung erlaubt es, diese Messungen nicht nur in Bragg- (Reflektions-) Geometrie, sondern auch in Laue- (Transmissions-) Geometrie durchzuführen. Dadurch gelingt es, das gesamte Volumen der untersuchten Struktur zu erfassen, und die Beschränkung der Untersuchung auf oberflächennahe Regionen zu überwinden.
 13. Die neu entwickelte Methode zur μm -aufgelösten Diffraktion erlaubt eine schnelle und umfassende Untersuchung von Halbleitermaterialien und anderen kristallinen Strukturen. Ein Beispiel ist die industrielle Charakterisierung von Halbleiter-Wafern im Hinblick auf Kristallqualität.
 14. Am Beispiel der Wafer zeigt sich der Zusammenhang zwischen makroskopischen Qualitätsmerkmalen des Kristalls (*rocking*-Kurven-Halbwertsbreite (FWHM), Probenkrümmung) und ihren mikroskopischen Ursachen (Gitterverkippungen, Defektstruktur). Diese Parameter können ortsaufgelöst über die gesamte Probenoberfläche *gemappt* werden. Die *rocking*-Kurven-Halbwertsbreite einzelner Kristallite kann so gemessen werden; ebenso können Korngrenzen zwischen den Kristalliten nachgewiesen werden.

Curriculum Vitae

DANIEL LÜBBERT

Born in Freiburg im Breisgau, Germany, on August 5th, 1970.

Primary education

1976 – 1980 Elementary school, Ehrenkirchen

Secondary education

1980 – 1989 Deutsch-Französisches Gymnasium, Freiburg

Military service

1989 – 1990 Compulsory military service (oboist in orchestra), München

University

1990 – 1992 Freie Universität Berlin (*Vordiplom* in Physics)

1992 – 1993 Universität Heidelberg

1993 – 1994 Università degli Studi, Torino, Italy

1994 – 1996 Universität Hamburg (*Diplom* in Physics)

Doctoral degree

1997 – 1999 PhD thesis at Universität Potsdam
Research done at the European Synchrotron Radiation Facility, Grenoble,
France,
as an employee of the Fraunhofer-Institut für Zerstörungsfreie Prüfverfahren,
Saarbrücken

Versicherung

Hiermit erkläre ich, dass ich die vorliegende Arbeit selbständig und nur unter Benutzung der angegebenen Hilfsmittel angefertigt habe. Die Arbeit wurde bisher weder im Inland noch im Ausland an einer anderen Hochschule eingereicht.

Potsdam, im Dezember 1999